Università degli Studi di Torino
Scuola di Dottorato

Search for non resonant Higgs boson pair production in the four-lepton two-b-jet final state at $\sqrt{s} = 13$ TeV with the CMS experiment at the LHC

Alessandra Cappati

Università degli Studi di Torino
Scuola di Dottorato

Dottorato in Fisica ed Astrofisica

Search for non resonant Higgs boson pair production in the four-lepton two-b-jet final state at $\sqrt{s} = 13$ TeV with the CMS experiment at the LHC

Alessandra Cappati

Advisor: Nicola Amapane

Abstract

This thesis presents the search for non-resonant double Higgs boson (HH) production in the final state where one of the two Higgs bosons decays into four leptons (4ℓ, with ℓ denoting either an electron or a muon), while the other decays into a pair of b quarks ($b\bar{b}$), which hadronise in jets. The analysis is performed exploiting the full dataset collected by the CMS experiment in the LHC Run II in proton-proton collisions at $\sqrt{s} = 13$ TeV, corresponding to an integrated luminosity of 137 fb^{-1}. The analysis presented is the first search for HH production performed in the $b\bar{b}4\ell$ final state and the first HH analysis in the CMS collaboration to be completed with the full Run II dataset. An upper limit on the HH production cross section times the branching fraction in the $b\bar{b}4\ell$ final state is set to 30 times the standard model (SM) predictions at 95% confidence level (CL). Possible modifications of the Higgs boson self coupling are also investigated, and the Higgs boson self coupling modifier k_λ is constrained to the range $-9 < k_\lambda < 14$ at 95% CL.

Contents

Introduction

The Higgs boson was introduced with the formulation of the electroweak symmetry breaking (EWSB) mechanism. This mechanism was proposed in 1964 by Brout and Englert [1], Higgs [2], and Guralnik, Hagen and Kibble [3] to explain how particles acquire a mass. The standard model of particle physics (SM), in fact, without the introduction of the EWSB mechanism, predicts all particles to be massless, but experimental evidence suggests them to have a mass different from zero. The mechanism, built on the Goldstone theorem and on a doublet of complex scalar fields, describes how particle masses are generated through the interaction with the Higgs field. The main experimental implication of this mechanism is the prediction of a new physical scalar boson: the Higgs boson.
Since its postulation, the Higgs boson has been the subject of extensive studies, both to determine theoretical predictions on its nature in the context of the SM, and to experimentally confirm or exclude its existence. Since the late 80's, various high energy experiments tried to detect the predicted particle, exploring different mass ranges, since the Higgs boson mass is a free parameter of the model. After 48 years since its postulation, the discovery of the predicted boson was announced in July 2012 at the European Centre for Nuclear Research (CERN) by the ATLAS (A Toroidal LHC Apparatus) [4] and CMS (Compact Muon Solenoid) [5] collaborations. The Higgs boson discovery was the first experimental confirmation of the EWSB mechanism.
Since its discovery, the Higgs boson has been widely studied in order to check if its properties are in agreement with the theoretical predictions. All the measurements of Higgs boson properties performed up to the present time by the ATLAS and CMS collaborations have been found to be compatible with the SM predictions [6, 7, 8].
There are, however, properties of this particle that are yet to be probed. One of these is the Higgs boson self coupling. According to the theory, the Higgs boson is the only particle in the SM that couples to itself. The measurement of the Higgs boson self-coupling provides an independent and crucial test of the SM since it allows the Higgs scalar field potential to be probed [9]. The nature of this self coupling can be studied by searching for the double Higgs boson production (HH) in particle colliders as the LHC. HH production is therefore a fundamental process

to be investigated, since it can be used to directly probe the Higgs boson self coupling and to access the parameters of the Higgs potential.
The search for HH production at LHC is experimentally very challenging. The HH production cross section predicted by SM is very small, even in comparison with the single-Higgs boson production. This is due to destructive interference between processes that produce HH through the Higgs boson self coupling and processes where the two Higgs bosons are radiated from a gauge boson or a fermion.
Beyond standard model (BSM) processes can largely modify the cross section and the kinematic properties of Higgs boson pair production. Different BSM hypotheses that affect double Higgs boson production can be broadly divided in two classes: resonant HH production, where a new hypothetical particle decays into two Higgs bosons, or non-resonant production, where e.g. new couplings contribute to HH production. This second class is treated with an effective field theory (EFT) approach. This thesis is focused on the HH non-resonant production. For this BSM hypothesis, the SM Lagrangian is extended with dimension-6 operators, resulting in five parameters relevant for the HH production. One of these five parameters is the modifier to the Higgs boson self coupling, whose constraint is one of the goals of this thesis.
HH production processes can be probed in different decay channels. At the LHC a rich phenomenology is accessible and the ATLAS and CMS collaborations have been investigating a wide variety of HH decay channels. The study of HH production in different final states allows different regions of the anomalous coupling parameter space to be probed. A combination of different decay channels is thus necessary to obtain the best possible sensitivity on HH production. The CMS collaboration performed a combination of HH production searches with results obtained in different channels with datasets collected in the time period from 2010 to 2013 (denoted as LHC Run I) and in 2016 [10], with a significant improvement over the results obtained from individual channels. A new combination of results is foreseen for the near future, using results obtained in different final states with datasets collected in the data taking years 2016, 2017, 2018, which are denoted as LHC Run II.
The analysis presented in this thesis focuses on the search for HH production in the final state where one of the two Higgs bosons decays into four leptons (4ℓ, with ℓ denoting either an electron or a muon), while the other one decays into a pair of b quarks ($\mathrm{b\bar{b}}$), which hadronise in jets. The Higgs to four lepton decay channel ($\mathrm{H} \to \mathrm{ZZ} \to 4\ell$) is the rarest observed so far at the LHC, but it presents the largest signal-to-background ratio. Therefore, despite its low branching ratio, the $\mathrm{b\bar{b}}4\ell$ final state considered in this analysis presents a clear signature granted by the $\mathrm{H} \to 4\ell$ decay mode. The high branching fraction of the $\mathrm{H} \to \mathrm{b\bar{b}}$ decay channel partially compensates for the small branching fraction of the 4ℓ decay.
This work was carried out in the context of the CMS collaboration, exploiting the full dataset collected by the CMS experiment in the LHC Run II. This channel has

never been investigated before. Also, this analysis is the first HH search in CMS to produce results with the full LHC Run II dataset. It is expected to contribute to the combination that will be performed over all HH final states, allowing the sensitivity on the analysis to be improved.
In order to search for HH production in the $b\bar{b}4\ell$ final state, a specific event selection was optimized to collect events containing four leptons and at least two jets, selecting then the two jets with the highest value of the b tag discriminator, which are the most likely to derive from b quarks hadronisation. A multivariate analysis technique was developed in order to separate signal from background contributions, exploiting the kinematic characteristics of events. A statistical analysis was performed on selected events in order to extract the results. For the SM scenario an upper limit on the HH production cross section times the branching fraction in the $b\bar{b}4\ell$ final state was set, while for the BSM case a constraint on the Higgs boson self coupling modifier was determined.
This thesis is structured as follows. A theoretical overview on the EWSB mechanism and HH production theory is briefly reported in Chapter 1. Chapter 2 presents the structure of the experimental apparatus, thus introducing the LHC accelerator and briefly describing the CMS experiment and the techniques for reconstructing events and particles. Chapter 3 describes the $b\bar{b}4\ell$ final state, the datasets used for the analysis, and the selection of physics objects. In Chapter 4 the event selection is presented, and the background estimation techniques, the multivariate analysis strategy, and the estimate of systematic uncertainties are discussed. Finally, Chapter 5 reports the statistical analysis technique used and the results obtained for SM and BSM scenarios.

Chapter 1

Higgs boson pair production

The discovery of the Higgs boson by the ATLAS and CMS collaborations in 2012 experimentally confirmed the Brout-Englert-Higgs (BEH) mechanism, which predicts the existence of a massive scalar particle. All the properties of the newly discovered particle measured so far have been found to be in agreement with the predictions made for the Higgs boson, but there are still properties not yet probed. One of these is the Higgs boson self coupling. According to the theory, the Higgs boson is the only particle that couples to itself and the strength of this self coupling can be probed in a particle collider as LHC by searching for double Higgs boson production (HH).
The search for HH production is fundamental for the landscape of particle physics since observing HH production would be another crucial validation for the BEH mechanism. If any deviations from the standard model of particle physics (SM) are observed, that would open a window on new physics beyond the SM (BSM).

This chapter presents the theory predictions for HH production in the context of both SM and BSM scenarios. After introducing the SM gauge structure and its scalar sector, HH production in the SM is reviewed. Then HH production is discussed in the context of BSM models, that can result in resonant or non-resonant HH processes. Finally, the phenomenology in collider experiments and results obtained by previous HH searches at the LHC are presented.

1.1 The standard model of particle physics

The Standard Model of particle physics (SM) is a renormalisable quantum field theory that describes the fundamental constituents of matter and their interactions. It provides a unified description of the strong and electroweak forces, and contains a scalar sector responsible for the BEH mechanism that breaks the electroweak symmetry and generates the masses of the known elementary particles.

1.1.1 Standard model gauge groups and fields

The SM Lagrangian is locally invariant under the gauge group $\mathrm{SU}(3)_C \times \mathrm{SU}(2)_L \times \mathrm{U}(1)_Y$. Strong interactions are described by the quantum chromodynamics (QCD), a gauge field theory invariant under the colour symmetry gauge group $\mathrm{SU}(3)_C$; the theory invariance results in the existence of 8 different mediators of the strong interaction: the *gluons*. The electroweak interactions are described by a gauge field theory invariant under the weak isospin and hypercharge symmetry gauge group $\mathrm{SU}(2)_L \times \mathrm{U}(1)_Y$; the electroweak theory describes together the weak and the electromagnetic interactions, mediated by the $\mathrm{W}^{\pm}$ and Z bosons, and the photon (γ), respectively.
In the SM, matter is described by twelve fundamental spin-$\frac{1}{2}$ fermion fields: six for *quarks*, which are subject to both strong and electroweak interactions and do not exist as free states, and six for *leptons*, which are sensitive only to electroweak interactions. Fermions are organized in three generations: the first one forms ordinary matter, while the other two are heavier copies of it. The fermion fields are summarised in the Table1.1, in their $\mathrm{SU}(2)_L$ representation, together with their main quantum numbers.

Table 1.1: SM fermion fields in their $\mathrm{SU}(2)_L$ representation, with their main quantum numbers: weak isospin (I_3), hypercharge (Y) and electric charge (Q). The L and R indices denotes the left and right chiralities, respectively.

	1st gen	2nd gen	3rd gen	I_3	Y	Q
Quarks	$\begin{pmatrix} u_L \\ d_L \end{pmatrix}$	$\begin{pmatrix} c_L \\ s_L \end{pmatrix}$	$\begin{pmatrix} t_L \\ b_L \end{pmatrix}$	$\begin{pmatrix} 1/2 \\ -1/2 \end{pmatrix}$	$\begin{pmatrix} 1/3 \\ 1/3 \end{pmatrix}$	$\begin{pmatrix} 2/3 \\ -1/3 \end{pmatrix}$
	u_R	c_R	t_R	0	4/3	2/3
	d_R	s_R	b_R	0	-2/3	-1/3
Leptons	$\begin{pmatrix} \nu_{e,L} \\ e_L \end{pmatrix}$	$\begin{pmatrix} \nu_{\mu,L} \\ \mu_L \end{pmatrix}$	$\begin{pmatrix} \nu_{\tau,L} \\ \tau_L \end{pmatrix}$	$\begin{pmatrix} 1/2 \\ -1/2 \end{pmatrix}$	$\begin{pmatrix} -1 \\ -1 \end{pmatrix}$	$\begin{pmatrix} 0 \\ -1 \end{pmatrix}$
	e_R	μ_R	τ_R	0	-2	1

1.1.2 The Brout-Englert-Higgs mechanism

The SM has been recently (in the time scale of physics theories) enriched with a scalar sector which is responsible for the origin of SM fundamental particles masses.

Experimental observations showed that many SM particles, in particular fermions and weak gauge bosons, have a non-zero mass. In order to reproduce the observed masses, the simple addition of a mass term in the Lagrangian of the electroweak theory is not a valid method, because this term would spoil the gauge invariance. As an example, a mass term for a W boson could be written as $m_{\mathrm{W}}^2 \mathrm{W}_\mu^\dagger \mathrm{W}^\mu$, and

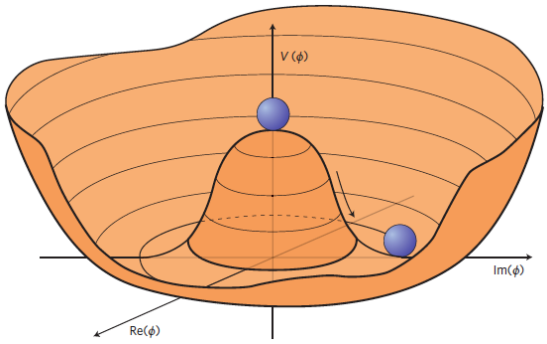

Figure 1.1: Illustration of the Higgs potential in the case of $\mu^2 < 0$. In this case the minimum is at $|\phi|^2 = -\mu^2/(2\lambda)$. The ground state of the theory breaks spontaneously the symmetry [11].

this term is not invariant under the gauge transformations of the $\mathrm{SU}(2)_L \times \mathrm{U}(1)_Y$ group.

The Brout-Englert-Higgs (BEH) mechanism was proposed in 1964 independently in three different papers from Brout and Englert [1], Higgs [2], and Guralnik, Hagen and Kibble [3], to explain the origin of weak gauge bosons and fermions masses. The mechanism is based on the spontaneous breaking of the $\mathrm{SU}(3)_C \times \mathrm{SU}(2)_L \times \mathrm{U}(1)_Y$ symmetry into the $\mathrm{SU}(3)_C \times \mathrm{U}(1)_{\mathrm{EM}}$ symmetry, without violating the local gauge invariance.
In the BEH mechanism, the symmetry breaking is realized by the presence of a field symmetric under gauge transformations, that acquires a non-zero expectation value in the vacuum state. The simplest field of this type that can be introduced is a $\mathrm{SU}(2)_L$ doublet of complex scalar fields

$$\phi = \begin{pmatrix} \phi^+ \\ \phi^0 \end{pmatrix}, \tag{1.1}$$

which is added in the SM Lagrangian via the term

$$\mathcal{L}_{BEH} = (D_\mu \phi)^\dagger (D^\mu \phi) - V\left(\phi^\dagger \phi\right), \tag{1.2}$$

where

$$D_\mu = \partial_\mu + \frac{ig'}{2}\mathcal{A}_\mu Y + \frac{ig}{2}\sigma \cdot \vec{B}_\mu \tag{1.3}$$

is the covariant derivative, where g is the coupling constant of the $\mathrm{SU}(2)_L$ group, g' is the $\mathrm{U}(1)$ coupling constant, and Y and $\sigma = (\sigma_1, \sigma_2, \sigma_3)$ are the Pauli matrices that generate, respectively, $\mathrm{U}(1)$ and $\mathrm{SU}(2)$. $\mathcal{A}_\mu$ and $\vec{B}_\mu = (B^1_\mu, B^2_\mu, B^3_\mu)$ are gauge fields associated with $\mathrm{U}(1)_Y$ and $\mathrm{SU}(2)_L$, respectively.

The potential $V\left(\phi^\dagger\phi\right)$ is chosen as (see Figure 1.1)

$$V\left(\phi^\dagger\phi\right) = \mu^2\phi^\dagger\phi + \lambda\left(\phi^\dagger\phi\right)^2 \tag{1.4}$$

with $\mu^2 < 0$ and $\lambda > 0$. When $\mu^2 < 0$, $\langle\phi^2\rangle = 0$ is an unstable local maximum of the potential. The minimum of the potential has $\langle\phi^2\rangle \neq 0$, in particular the location of the minimum is at

$$|\phi|^2 = -\frac{\mu^2}{2\lambda} = \frac{v^2}{2} \tag{1.5}$$

with an arbitrary SU(2) × U(1) orientation, leading to spontaneous symmetry breaking when one chooses any points at the bottom of the potential. The quantity v is called *vacuum expectation value* (VEV) of the potential.
Minimizing the potential, one obtains:

$$\frac{\partial}{\partial\left(\phi^\dagger\phi\right)}V\left(\phi^\dagger\phi\right) = \mu^2 + 2\lambda\langle\phi\rangle_0 = \mu^2 + 2\lambda\left[\left(\phi^+_{\text{vac}}\right)^2 + \left(\phi^0_{\text{vac}}\right)^2\right] = 0. \tag{1.6}$$

With no loss in generality, one can set:

$$\phi^+_{\text{vac}} = 0, \quad \phi^0_{\text{vac}} = \sqrt{-\frac{\mu^2}{2\lambda}}. \tag{1.7}$$

This choice breaks the $\text{SU}(2)_L \times \text{U}(1)_Y$ symmetry, but preserves the invariance under the residual $\text{U}(1)_{\text{EM}}$ gauge symmetry of electromagnetism.
One can consider perturbations of the scalar field ϕ around the chosen vacuum

$$\phi = \frac{1}{\sqrt{2}}\exp\left(\frac{i\theta\cdot\sigma}{2v}\right)\begin{pmatrix}0\\ v+\text{H}\end{pmatrix}, \tag{1.8}$$

where $\theta = (\theta^1, \theta^2, \theta^3)$ and H are four real scalar fields.
The θ fields are three massless Goldstone bosons, whose existence is predicted by the Goldstone theorem [12], since three of the four generators of $\text{SU}(2)_L \times \text{U}(1)_Y$ are broken by the VEV. These massless fields, not observed in nature, can be removed by choosing a proper gauge (*unitary gauge*). This can be done with the following gauge transformation:

$$\phi \mapsto \phi' = \exp\left(\frac{-i\theta^a\sigma_a}{2v}\right)\phi = \frac{1}{\sqrt{2}}\begin{pmatrix}0\\ v+\text{H}\end{pmatrix}. \tag{1.9}$$

After this transformation, only the real scalar field H remains whose quanta are associated to the physical particle *Higgs boson*.
If one defines the charged gauge fields $W^\pm_\mu$ as

$$W^\pm_\mu = \frac{B^1_\mu \mp iB^2_\mu}{\sqrt{2}}, \tag{1.10}$$

and the neutral gauge fields as

$$Z_\mu = \frac{-g'\mathcal{A}_\mu + gB^3_\mu}{\sqrt{g^2+g'^2}}, \tag{1.11}$$

$$A_\mu = \frac{g\mathcal{A}_\mu + g'B^3_\mu}{\sqrt{g^2+g'^2}}, \tag{1.12}$$

and then substitutes the expression of the ϕ field in the unitary gauge Eq. (1.9) in Eq. (1.2), the BEH Lagrangian becomes:

$$\begin{aligned}\mathcal{L}_{BEH} = &\frac{1}{2}\partial_\mu \mathrm{H}\partial^\mu \mathrm{H} - \frac{1}{2}\left(2\lambda v^2\right)\mathrm{H}^2 \\ &+ \left(\frac{g^2v^2}{4}\right) W^-_\mu W^{\mu+} + \frac{1}{2}\left(\frac{(g^2+g'^2)v^2}{4}\right) Z_\mu Z^\mu \\ &+ \left(\frac{g^2v^2}{4}\right)\frac{2}{v}\mathrm{H}W^-_\mu W^{\mu+} + \left(\frac{(g^2+g'^2)v^2}{4}\right)\frac{1}{v}\mathrm{H}Z_\mu Z^\mu \\ &+ \left(\frac{g^2v^2}{4}\right)\frac{1}{v^2}\mathrm{H}^2 W^-_\mu W^{\mu+} + \frac{1}{2}\left(\frac{(g^2+g'^2)v^2}{4}\right)\frac{1}{v^2}\mathrm{H}^2 Z_\mu Z^\mu \\ &- \lambda v\mathrm{H}^3 - \frac{\lambda}{4}\mathrm{H}^4 + \frac{\lambda}{4}v^4.\end{aligned} \tag{1.13}$$

The first line represents the evolution of the scalar Higgs field which has a mass:

$$m^2_\mathrm{H} = 2\lambda v^2 = -2\mu^2 \tag{1.14}$$

which is a free parameter of the model, since there is no theoretical prediction for it within the SM. The second line contains the mass terms of the weak bosons, whose masses are:

$$m^2_W = \frac{g^2v^2}{4}, \tag{1.15}$$

$$m^2_Z = \frac{(g^2+g'^2)v^2}{4}. \tag{1.16}$$

The Goldstone bosons that were removed by the gauge transformation became the longitudinal polarization of the $W^\pm$ and Z^0 vector bosons, that initially were massless (with only transversal polarizations), acquired a mass, thanks to the BEH mechanism. It can be noted that the A_μ field (the photon) remains massless, and this is due to the unbroken $\mathrm{U(1)_{EM}}$ symmetry, identified with electromagnetism. The third and fourth lines of Eq. 1.13 describe the interactions of the weak bosons with the Higgs field, through triple and quadruple vertices (HWW, HZZ, HHWW and HHZZ).

The last line of the equation predicts Higgs boson self couplings through cubic and quartic vertices. The BEH potential can be rewritten in terms of these self interactions

$$V(\mathrm{H}) = \frac{1}{2}m_{\mathrm{H}}^2\mathrm{H}^2 + \lambda_{\mathrm{HHH}}\mathrm{H}^3 + \lambda_{\mathrm{HHHH}}\mathrm{H}^4 - \frac{1}{4}\lambda v^4, \tag{1.17}$$

where

$$\lambda_{\mathrm{HHH}} = \lambda v = \frac{m_{\mathrm{H}}^2}{2v} \tag{1.18}$$

and

$$\lambda_{\mathrm{HHHH}} = \lambda/4 = \frac{m_{\mathrm{H}}^2}{8v^2}, \tag{1.19}$$

since from eq. 1.14 we have

$$\lambda = \frac{m_{\mathrm{H}}^2}{2v^2}. \tag{1.20}$$

This shows that the Higgs boson self couplings are directly related to the Higgs boson mass and to the VEV of the scalar potential. Therefore, an experimental measurement of the Higgs boson self coupling is crucial for better knowing the Higgs potential and exploring the nature of the electroweak symmetry breaking.

The spontaneous symmetry breaking allows also fermions to acquire mass through interactions with the Higgs field: the *Yukawa interactions*. The fermions mass terms introduced in the SM Lagrangian are gauge-invariant:

$$\begin{aligned}\mathcal{L}_{\mathrm{Yukawa}} = &-g_{f'}\left[\bar{\psi}'_R\phi^\dagger\begin{pmatrix}\psi_L\\ \psi'_L\end{pmatrix} + (\bar{\psi}_L\ \bar{\psi}'_L)\phi\psi'_R\right]\\ &-g_f\left[\bar{\psi}_R\tilde{\phi}^\dagger\begin{pmatrix}\psi_L\\ \psi'_L\end{pmatrix} + (\bar{\psi}_L\ \bar{\psi}'_L)\tilde{\phi}\psi_R\right],\end{aligned} \tag{1.21}$$

where $\tilde{\phi}$ is the charge conjugate of the ϕ field, ψ and ψ' are the up and down fermions, and g_f and $g_{f'}$ are the intensities of the interactions. After electroweak symmetry breaking, the Lagrangian 1.21 take the form:

$$\mathcal{L}_{\mathrm{Yukawa}} = -\frac{v}{\sqrt{2}}\left(1+\frac{\mathrm{H}}{v}\right)\left[g_{f'}\left(\bar{\psi}'_R\psi'_L + \bar{\psi}'_L\psi'_R\right) + g_f\left(\bar{\psi}_R\psi_L + \bar{\psi}_L\psi_R\right)\right]. \tag{1.22}$$

Fermion masses can be defined as

$$m_{f^{(\prime)}} = g_{f^{(\prime)}}\frac{v}{\sqrt{2}}. \tag{1.23}$$

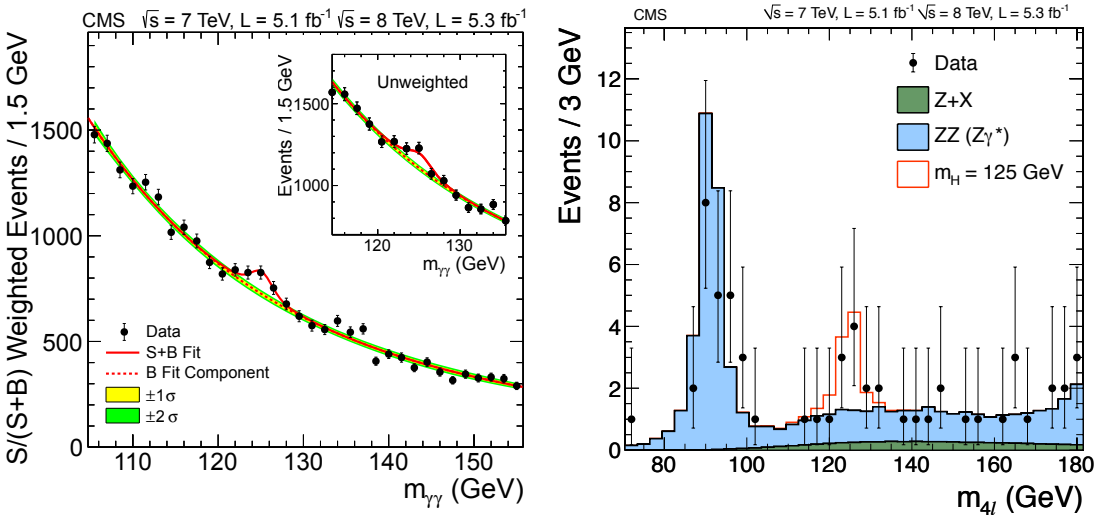

Figure 1.2: CMS Collaboration Invariant mass distributions for the di-photon final state (left) and the four-lepton final state (right) at the moment of the Higgs boson discovery [15].

This procedure implies also that the Higgs field interacts with fermions, with couplings proportional to fermion masses.
Mass matrices in this formula have to take into account that fermions weak and mass eigenstates differ. Furthermore, in the case of neutrinos it is possible that the electroweak symmetry breaking mechanism plays only a partial role in generating the observed neutrino masses, with additional contributions at higher scale via other mechanisms [13, 14].

1.1.3 Higgs boson phenomenology, discovery, and experimental status

The BEH mechanism received an experimental confirmation in 2012, when the discovery of a new scalar boson with a mass of about 125 GeV was announced by the ATLAS [4] and CMS [5] Collaborations. The discovery relied on a combination of studies in different final states performed with data collected by the two collaborations in 2011 and 2012 at $\sqrt{s} = 7$ and 8 TeV (LHC Run I). The two final states that provided most of the sensitivity were the two photons final state ($H \to \gamma\gamma$) and the four-lepton final state ($H \to ZZ \to 4\ell, \ell = e, \mu$), where leptons are electrons or muons. Figure 1.2 shows the invariant mass distribution obtained, by the CMS Collaboration, for these two final states. In these plots the Higgs boson is visible as an excess over the background around 125 GeV/c^2.
After the discovery, Higgs boson properties have been deeply investigated in order to verify if they were in agreement with the theoretical predictions. Already with

Run I data it was possible to confirm the spin-parity hypothesis $J^P = 0^+$ [16], and at the end of the LHC Run I, the ATLAS and CMS collaborations performed a combined measurement of its mass m_H [17]:

$$m_H = 125.09 \pm 0.21(\text{stat.}) \pm 0.11(\text{syst.}) \text{ GeV}/c^2 \tag{1.24}$$

Other Higgs boson properties were also investigated like the production cross-section and couplings with fermions and bosons [8, 7], anomalous couplings with bosons and the particle width [18].
In 2015 the LHC started again to deliver proton-proton (pp) collisions, but at higher centre-of-mass energy ($\sqrt{s}$ =13 TeV) starting the data taking period referred to as Run II (lasted from 2016 to 2018). Thanks to the increase of energy and to the larger amount of data collected, the ATLAS and CMS collaborations managed to investigate the less accessible properties of the Higgs boson, like the sub-dominant production modes of the Higgs particle.

The theory predicts that the Higgs boson can be produced through several different mechanisms. In a pp collider like the Large Hadron Collider (LHC), the dominant production mechanism is the *gluon fusion* (ggH). This process involves two gluons that merge into a Higgs boson via an intermediate quark loop. At the LHC Run II energy, it has a cross section of 48.58 pb [19]. With a 12 times smaller cross section, the *vector boson fusion* is the second main mechanism at the LHC, in which the Higgs boson is produced in association with a high-energy jet pair. The third most relevant process at LHC is the Higgs boson associated production with a vector boson (VH, V=Z,W), while the fourth main mechanism is the associated production with a top quark pair (ttH). The VBF and VH production modes allow the couplings with vector bosons to be studied, while ttH allows the Yukawa coupling with top quark to be investigated.
Figure 1.3 (left) reports the cross sections of Higgs boson production modes computed for the centre-of-mass energy of LHC in Run II (13 TeV).

Other Higgs boson couplings can be investigated by considering the different Higgs boson decay modes. The Higgs boson directly couples to all massive particles of the Standard Model and can also couple to massless particles via intermediate loops. This fact leads to a variety of different decay channels. Figure1.3 (right) presents the values of the branching fractions as a function of the Higgs boson mass m_H. Some of them, like $H \to ZZ^*$ and $H \to WW^*$, give information on Higgs boson couplings to weak vector bosons. Others, like $H \to b\bar{b}$ [20, 21] and $H \to \tau^+\tau^-$ [22, 23], which were recently observed, allow Higgs boson direct couplings to fermions to be investigated.

The study of Higgs boson production processes and decay channels is important since it allows not only the Higgs boson couplings with other particles to be studied,

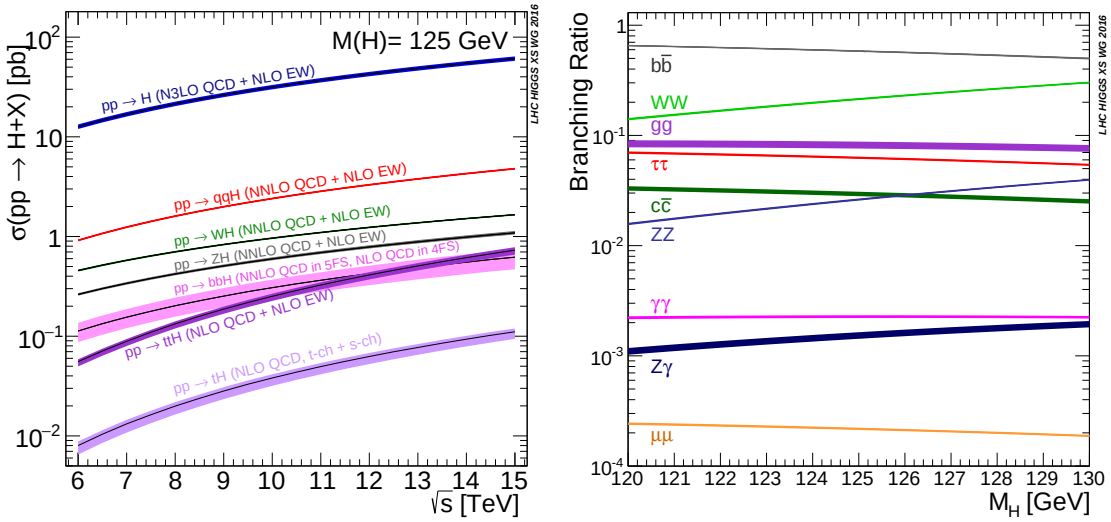

Figure 1.3: (Left) Production mechanisms cross sections and their uncertainties for a SM Higgs boson of mass $m_{\mathrm{H}} = 125$ GeV, as function of the centre-of-mass energy, $\sqrt{s}$, for proton-proton collisions [19]. (Right) SM Higgs boson branching ratios and their uncertainties as a function of m_{H}, for the mass range around 125 GeV [19].

and therefore further understanding the Higgs boson nature, but also possible deviations from the SM to be tested.

Figure 1.4 shows the Higgs boson couplings to fermions and bosons measured by the ATLAS and CMS collaborations, as a function of the particle mass. It is possible to notice that all the values measured (up to now) follow the SM predictions. One thing that is missing from this plot is the Higgs boson coupling with itself (λ_{HHH}). Experimentally measuring λ_{HHH} would allow us to verify if this interaction fits in the coupling scheme shown in figure 1.4, providing a test for the validity of the SM predictions.
The Higgs boson self coupling λ_{HHH} can be directly probed by studying the Higgs boson pair (HH) production. Investigating this process is, therefore, crucial for probing the Higgs boson nature, and thus further understanding the BEH mechanism. Furthermore, since BSM processes could contribute to the Higgs boson self coupling, this study is an important benchmark for the SM predictions and for testing possible deviations arising from BSM contributions.

1.2 Higgs boson pair production

HH production can be used to directly probe the Higgs boson self coupling. Although the observation of HH production processes can be experimentally very

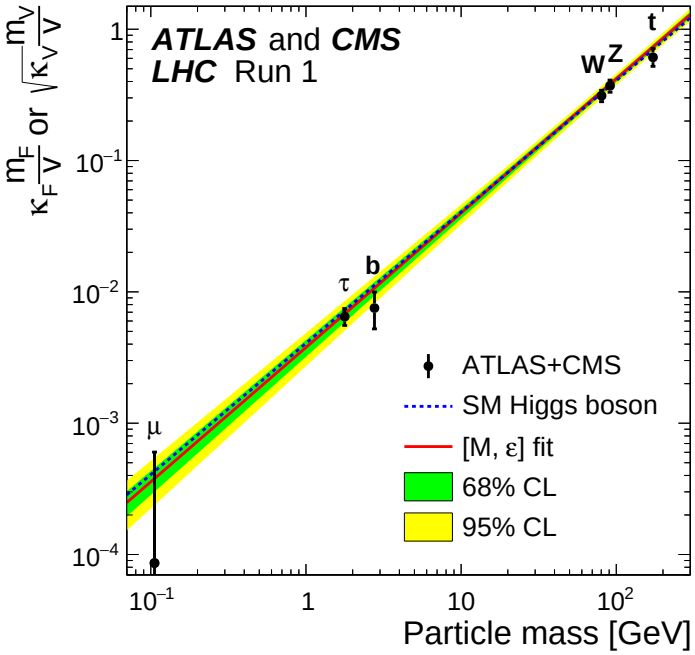

Figure 1.4: Higgs boson couplings as a function of the particle mass obtained with combination of ATLAS and CMS collaborations data collected in LHC Run I [6].

challenging because of the tiny cross section, they are fundamental to be investigated since they provide direct access to the Higgs potential parameters.
The Higgs boson self coupling, however, is not the only process that contributes to HH production. Beside processes that involve the trilinear coupling, there are others where two Higgs bosons are radiated from a gauge boson or a fermion.

1.2.1 HH production in the SM

According to the SM, at the LHC HH can be produced through four main different mechanisms [9], [24], that are discussed below. In Figure 1.5 leading-order (LO) Feynman diagrams of these processes are illustrated, while Figure 1.6 reports a summary plot of the total cross sections as a function of the collider centre-of-mass energy.

- **Gluon fusion**, $gg \rightarrow$ HH, is the dominant HH production mechanism at LHC (Figure 1.6) and it is mediated by loops of heavy quarks (mainly top quarks) that couple to the Higgs boson. There are two destructively interfering diagrams contributing to the process: the box diagram where two on-shell Higgs bosons are radiated from a heavy quark (Figure 1.5 (a) left), and the triangle diagram where a Higgs pair is produced through the trilinear cou-

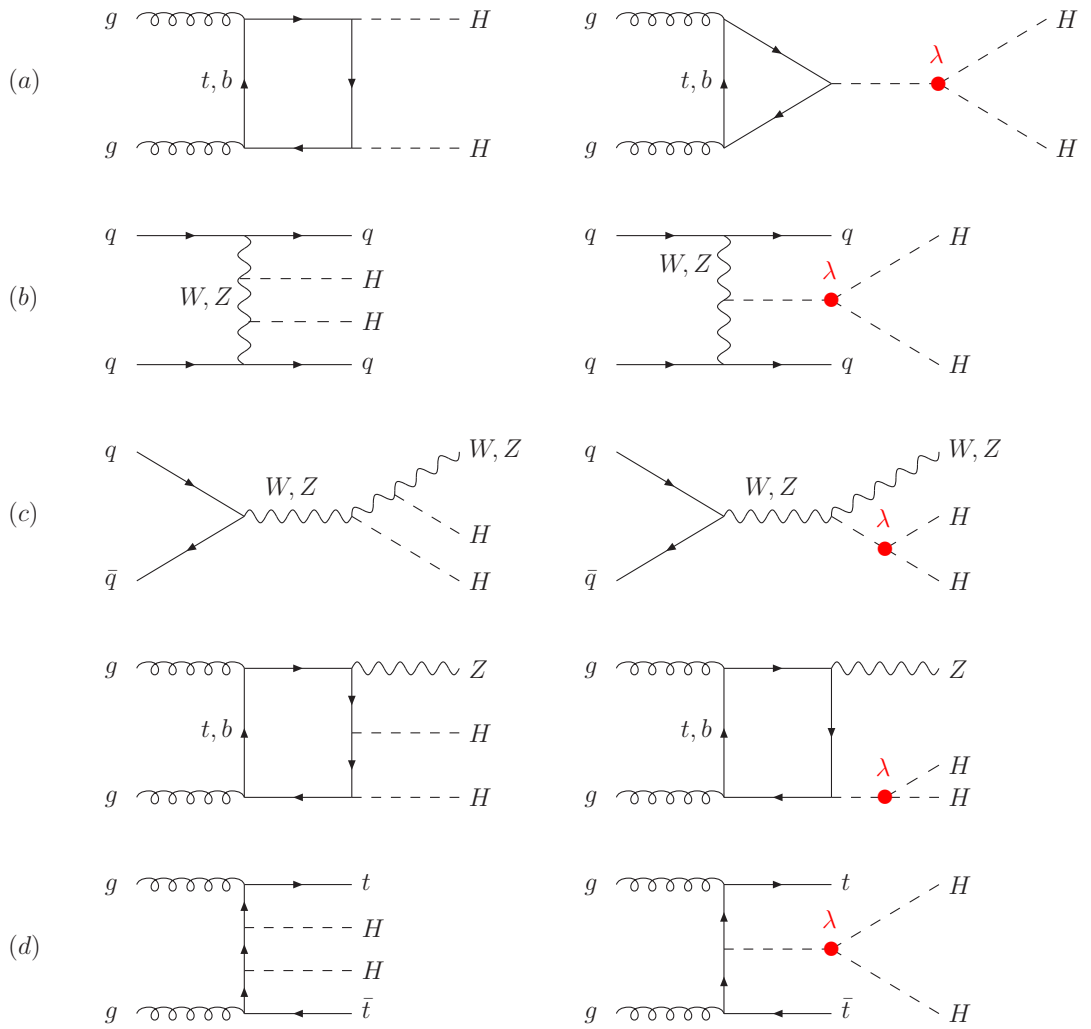

Figure 1.5: Diagrams of the HH production modes: gluon fusion (a), vector-boson fusion (b), double Higgs-strahlung (c) and double Higgs bremsstrahlung off top quarks (d). The trilinear Higgs coupling contribution is marked in red [24].

pling (Figure 1.5 (a) right). The relative contribution of the two different diagrams, with their interference, is shown in Figure 1.7. The presence of the box diagram dilutes the dependency of the HH production cross section on the trilinear coupling λ_{HHH}, increasing the dependency on the Yukawa top quark coupling y_t.

- **Vector boson fusion** (VBF), $qq' \to V^*V^*qq' \to \mathrm{HH}qq'$ ($V = \mathrm{W}, \mathrm{Z}$), is the second-largest production mechanism at the LHC. It involves diagrams in which two Higgs bosons radiate from the virtual W or Z bosons (Figure 1.5

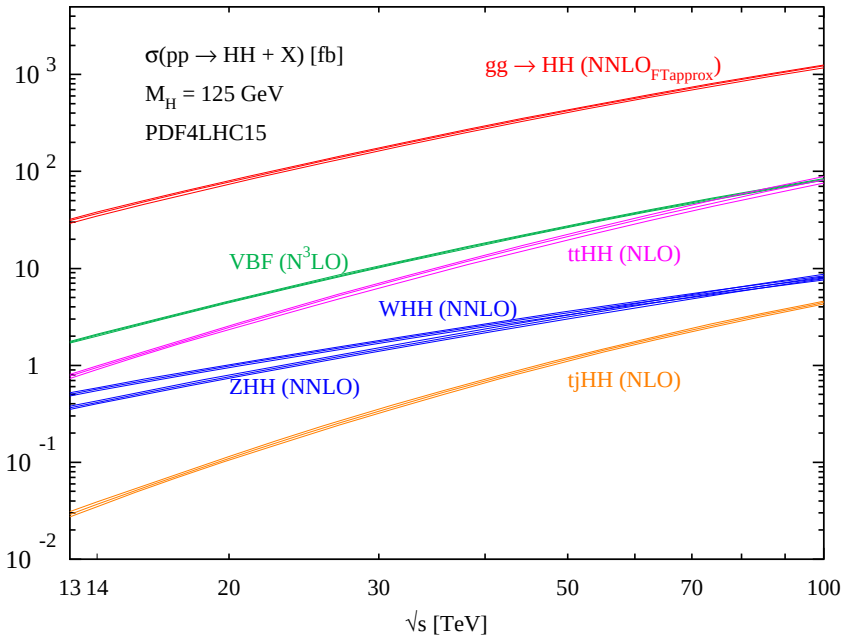

Figure 1.6: Total cross sections for Higgs pair production within the SM via the different production processes (gluon fusion, vector-boson fusion, double Higgs-strahlung and double Higgs bremsstrahlung off top quarks), as a function of the collider centre-of-mass energy. The size of the bands shows the total uncertainties originating from the scale dependence and the PDF+α_s uncertainties [24].

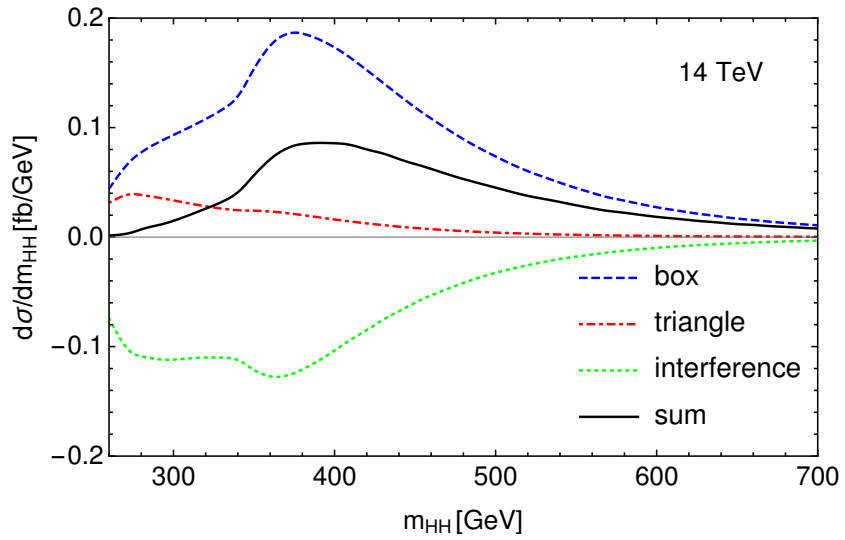

Figure 1.7: Higgs pair invariant mass distribution at leading order for the different contributions to the gluon fusion production mechanism and their interference [24].

Table 1.2: Cross section values for different HH production mode, assuming a Higgs boson mass $m_{\mathrm{H}} = 125$ GeV [24].

Process	σ [fb] ($\sqrt{s} = 13$TeV)
ggHH	$31.05^{+2.2\%}_{-5.0\%}$(scale)$\pm$3.0%(PDF+α_s)$\pm$2.6%($\mathrm{m_{top}}$)
VBF HH	$1.73^{+0.03\%}_{-0.04\%}$(scale)$\pm$2.1%(PDF+α_s)
HHZ	$0.363^{+3.4\%}_{-2.7\%}$(scale)$\pm$1.9%(PDF+α_s)
$\mathrm{HHW^+}$	$0.329^{+0.32\%}_{-0.41\%}$(scale)$\pm$2.2%(PDF+$\alpha_s$)
$\mathrm{HHW^-}$	$0.173^{+1.2\%}_{-1.3\%}$(scale)$\pm$2.8%(PDF+α_s)
$\mathrm{t\bar{t}HH}$	$0.775^{+1.5\%}_{-4.3\%}$(scale)$\pm$3.2%(PDF+α_s)
$\mathrm{t}j\mathrm{HH}$	$0.0289^{+5.5\%}_{-3.6\%}$(scale)$\pm$4.7%(PDF+α_s)

(b) left), and diagrams in which the Higgs boson (off-shell) splits into a Higgs pair (Figure 1.5 (b) right). The cross section is one order of magnitude smaller with respect to the gluon fusion cross section (Figure 1.6), but this process presents two high energy jets in the final state that can represent a clean signature for identifying this mechanism.

- **Double Higgs-strahlung**, or associated production of Higgs pairs with a W or Z boson, $q\bar{q} \to V^* \to V\mathrm{HH}$ ($V = \mathrm{W}, \mathrm{Z}$), (Figure 1.5 (c)) has a cross section significantly lower than VBF, as shown in Figure 1.6. In the final state of this process, the Higgs boson pair is present together with a vector boson.

- **Double Higgs strahlung off top quarks**. In the process of associated production of Higgs boson pair with top quark pairs, $gg/qq' \to \mathrm{t\bar{t}HH}$, (Figure 1.5 (d)) the Higgs boson pair is either radiated from the top quarks, or produced through the trilinear coupling. The cross section of this process exceeds the one of VBF HH production at high centre-of-mass energy of the collider, as shown in Figure 1.6. The single-top associated production, $qq' \to \mathrm{t}j\mathrm{HH}$, is the only process sensitive at the same time to HH coupling to vector bosons and to top quarks, but the corresponding cross section is too small to be investigated at LHC (Figure 1.6). It could be targeted in future colliders.

The cross sections for the HH production mechanism are reported in Table 1.2 for the LHC Run II centre-of-mass energy.
HH production cross sections are very small, compared for example to single Higgs boson production. This leads to the strategy of most of the experimental searches for HH production, including the one presented in this thesis, of focusing only on the dominant gluon fusion production mechanism. Consequently, the symbol σ_{HH} will be used in the following to indicate the gluon fusion HH production cross section.

1.2.2 BSM HH production

BSM processes can modify the HH production cross section. There are different hypotheses that describe BSM processes resulting in the production of a pair of Higgs bosons. These processes are divided in two main categories: *resonant* HH production processes, where the Higgs boson pair is produced through the decay of a new particle, and *non-resonant* HH production, that is treated with an effective field theory (EFT) approach.
This thesis is focused on the HH non-resonant production, but a brief summary of HH resonant processes is reported in the following paragraph for completeness.

HH resonant production

Resonant HH production can be used to investigate BSM hypotheses that predict the existence of a new resonance X of mass $m_{\mathrm{X}} > 2m_{\mathrm{H}}$ decaying into a pair of Higgs bosons. From the experimental point of view, the searches of HH resonant production require the development of dedicated analysis strategies in order to ensure a large acceptance over the mass range, since the new resonance mass can range from the kinematic threshold of 250 GeV up to several TeV. BSM models that predict a HH signature are diverse and some of them are presented in the following. This section is not meant to be an extensive summary of BSM models; on the contrary the discussion aims at showing that despite the different theoretical assumptions behind the analysed BSM models, they can be simultaneously tested in HH production.

The **Higgs singlet model** [25] predicts the existence of a new Higgs singlet in addition to the Higgs doublet of the SM. Both the Higgs fields acquire a non zero VEV, breaking the electroweak symmetry, and resulting in the existence of two real scalar fields. The lighter scalar field, conventionally denoted with h, is interpreted as the SM Higgs boson. The heavier scalar is instead denoted with H. The model predicts a modification of the higgs boson trilinear coupling and the presence of a new coupling Hhh between the two scalars. This generates an enhancement of the HH production cross section, resulting in a resonance peak in the HH invariant mass distribution.

The two-Higgs-doublet models **2HDM** [26] predict the existence of a new Higgs doublet field in addition to the SM one. The addition of a complex Higgs doublet implies the existence of different new scalar particles (depending on the model considered), that couple with the SM Higgs boson and produce a resonant HH signature. The 2HDM models are particularly interesting since the presence of two Higgs doublets is required also in low energy super symmetry (SUSY) models to break the electroweak symmetry. Thus these scenarios represent the contact point between Higgs and SUSY sectors.

Warped extra dimensions **WED** models [27, 28] are well motivated extensions to the SM, providing a natural solution to different open topics of the SM (electroweak hierarchy problem, hierarchies in the flavour sector). As a consequence of these models, the existence of new particles of spin 2 (*graviton*) and of spin 0 (*radion*) is predicted. These new particles can decay into a pair of Higgs bosons.

HH non-resonant production

BSM physics can be probed also in non-resonant HH production. New processes can contribute in the quantum loops responsible for HH production, modifying the kinematics of the process and enhancing the HH production rate, but without generating a resonance that then decays in a pair of Higgs bosons.

An effective-field-theory (EFT) approach is used in order to consider the most general set of perturbations to HH kinematics due to possible new physics. The key idea of this approach is that interactions of arbitrary complexity that act at short distances can be approximated systematically by a Lagrangian with an enumerable set of parameters, and this Lagrangian provides an "effective"description of any underlying model. In the case of HH production, the Lagrangian will be the SM Lagrangian with corrections described by addition of local operators.
In a renormalisable Lagrangian, all terms are operators of dimension $d \leq 4$. Thus the effects of BSM physics, whose scale is beyond the direct reach of LHC, can be locally approximated by adding to the SM Lagrangian higher order operators ($d > 4$). These additional operators are suppressed by powers of the new BSM interactions scale M. Considering that dimension-8 operators give a very little contribution because of the power suppression, and dimension-5 and dimension-7 operators involve lepton number violation and neutrino mass terms and can be ignored when discussing LHC processes, only dimension-6 operators are relevant and the EFT Lagrangian can be written as:

$$\mathcal{L} = \mathcal{L}_{\text{SM}} + \sum_i \frac{c_i}{M^2} \mathcal{O}_i^6 \tag{1.25}$$

where c_i are the Wilson coefficients, that parametrize the BSM physics contributions. This gives a finite set of parameters describing the most general modifications of the SM at short distances.
The EFT Lagrangian can be rewritten in terms of Higgs boson couplings [19] and

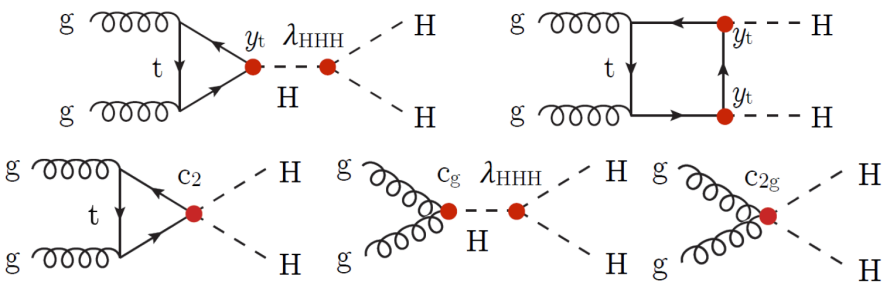

Figure 1.8: Feynman diagrams that contribute to HH non resonant production at LO. The two top diagrams correspond to SM-like processes, while the three bottom diagrams describe pure BSM effects [29].

the relevant terms for HH production via gluon fusion are given by:

$$\begin{aligned}\mathcal{L}^{\mathrm{HH}} = & \frac{1}{2}\partial_\mu \mathrm{H}\partial^\mu \mathrm{H} - \frac{1}{2}m_{\mathrm{H}}^2\mathrm{H}^2 - k_\lambda \lambda^{\mathrm{SM}}\mathrm{H}^3 \\ & - \frac{m_t}{v}\left(v + k_t\mathrm{H} + \frac{c_2}{v}\mathrm{HH}\right)(\bar{t}_L t_R + h.c.) \\ & + \frac{\alpha_s}{12\pi v}\left(c_g\mathrm{H} - \frac{c_{2g}}{2v}\mathrm{HH}\right)G^a_{\mu\nu}G^{a,\mu\nu}\end{aligned} \tag{1.26}$$

The presence of the dimension-6 operators introduces three new BSM contact interactions involving the gHH (c_g), ggHH (c_{2g}), and ttHH (c_2) vertices, and modifies the Higgs boson trilinear coupling λ_{HHH} and the top Yukawa coupling y_t. Deviations from the SM are expressed in terms of ratio between the coupling value and the SM expectation for that coupling: $k_\lambda = \lambda_{\mathrm{HHH}}/\lambda^{\mathrm{SM}}_{\mathrm{HHH}}$ for trilinear coupling and $k_t = y_t/y_t^{\mathrm{SM}}$ for top Yukawa coupling. These five new parameters (k_λ, k_t, c_2, c_g and c_{2g}) describe the lower level interactions, reported in Figure 1.8 where the BSM couplings are highlighted in red.

Exploring all the possible combinations of all the five couplings is not feasible for an experimental search in terms of complexity of the combinations and computing time. Thus an approach that defines *shape benchmarks* [29] is used. Benchmarks are combinations of the five EFT parameters whose topologies are representative for large regions of the five dimensional parameter space. They are defined by scanning a sample of 1507 points generated in a five-dimensional grid and regrouping those with similar kinematic properties in clusters. With this procedure, 12 benchmark shapes are defined and the corresponding shapes are shown in Figure 1.9. The values of the five couplings for each benchmark are reported in Table 1.3.

This approach allows non resonant HH production to be probed with a model-independent parametrization of BSM scenarios, and this is very useful given the large variety of BSM models that can result in non resonant HH production even

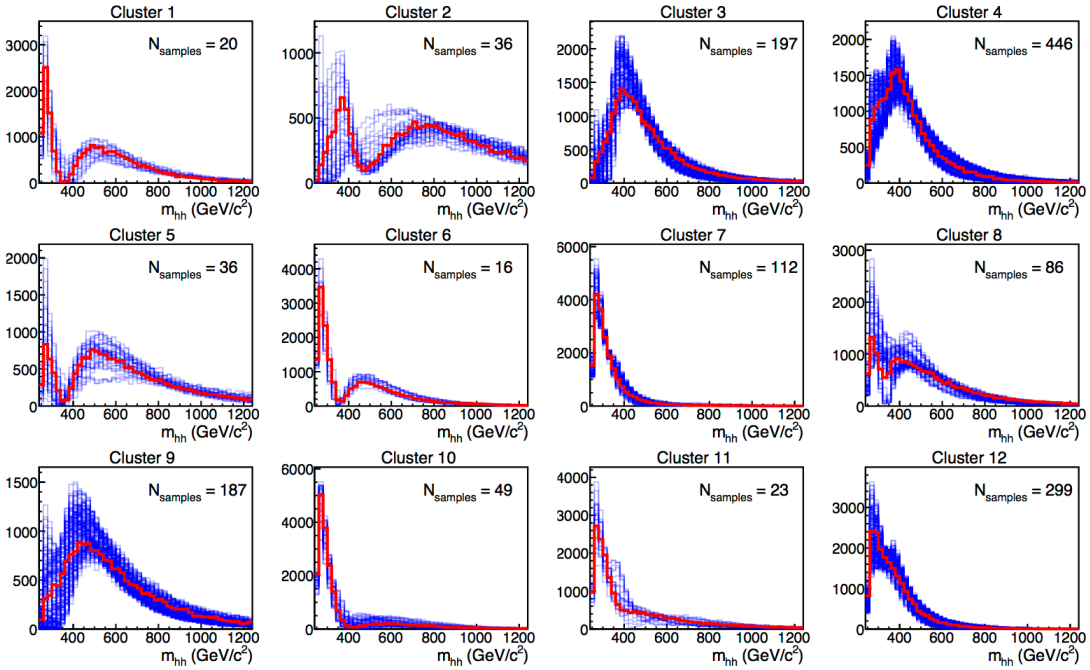

Figure 1.9: Distributions of the di-Higgs invariant mass m_{HH}. The red lines represent the benchmark shape of each cluster, while the blue lines describe the sample points with similar kinematic properties [29].

Table 1.3: Values of the EFT Lagrangian couplings that define the 12 shape benchmarks [29]

Benchmark number	k_λ	k_t	c_2	c_g	c_{2g}
1	7.5	1.0	-1.0	0.0	0.0
2	1.0	1.0	0.5	-0.8	0.6
3	1.0	1.0	-1.5	0.0	-0.8
4	-3.5	1.5	-3.0	0.0	0.0
5	1.0	1.0	0.0	0.8	-1.0
6	2.4	1.0	0.0	0.2	-0.2
7	5.0	1.0	0.0	0.8	-1.0
8	15.0	1.0	0.0	-1.0	1.0
9	1.0	1.0	1.0	-0.6	0.6
10	10.0	1.5	-1.0	0.0	0.0
11	2.4	1.0	0.0	1.0	-1.0
12	15.0	1.0	1.0	0.0	0.0
SM	1.0	1.0	0.0	0.0	0.0

starting from different theoretical motivations (multiplet extensions to the scalar sector [30], vector-like quarks [31], composite Higgs models [32], etc.).

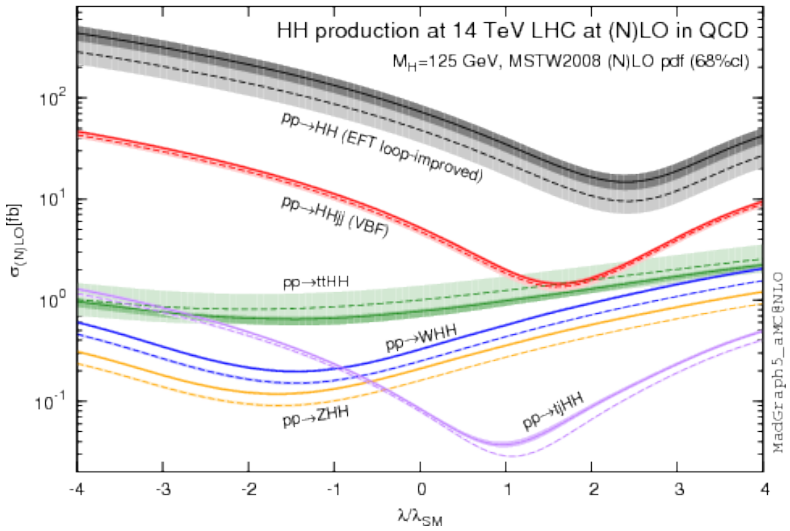

Figure 1.10: Total cross section for HH production as a function of the trilinear Higgs boson coupling. The dashed (solid) lines and light (dark) colour bands correspond to the LO (NLO) results [34].

Some experimental searches for non resonant HH production performed at the LHC, however, focus only on one (k_λ) or two (k_λ and k_t) of the EFT parameters illustrated before. The analysis presented in this thesis, for example, considers possible variations of the trilinear Higgs boson coupling by varying the k_λ parameter value in order to probe BSM physics. This procedure is performed by keeping all the other EFT parameters fixed to their SM value. This parametric approach is referred to as *k-framework* [33].
Even considering only one of the EFT parameters, it is possible to extract a lot of information from k_λ studies. As shown in Figure 1.10, variations of the value of λ_{HHH} modify the HH production cross section, and the interference between the different diagrams contributing to HH production results in a minimum of the cross section. In particular for the gluon fusion production process, which is the dominant production mode also in the hypothesis of anomalous trilinear coupling, the minimum of the cross section is located at $k_\lambda = 2.45$ (keeping all the other EFT parameters fixed to their SM value).
k_λ variations affect also HH kinematics, modifying the HH invariant mass and transverse momentum distributions.
These effects have important consequences for the experimental searches, that are sensitive to anomalous trilinear Higgs boson couplings through the total HH cross section and HH kinematic distribution.

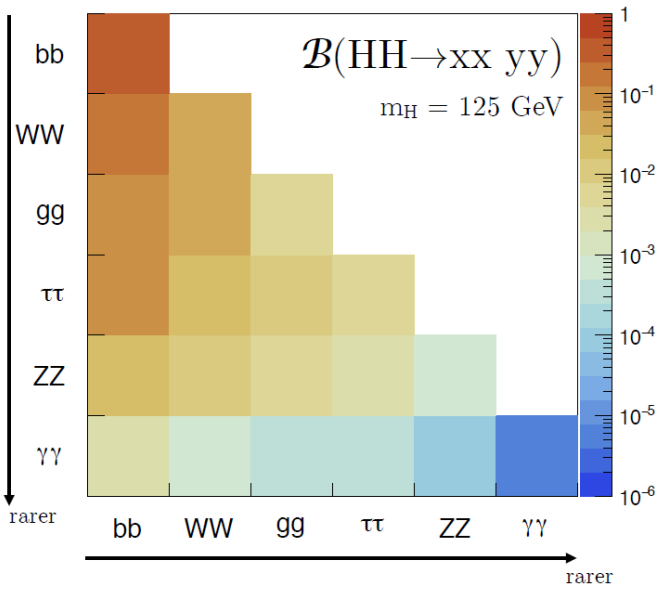

Figure 1.11: Branching ratios for HH decay into a selected group of final states. The decay modes for the two Higgs bosons are shown on each axis of the figure.

1.3 Search for HH production at the LHC

HH production processes are phenomenologically very rich and they can be probed in several different decay channels. At CERN LHC a large number of HH decay channels is accessible, thus a large number of HH searches is being carried on, making use of complementary techniques to enhance the sensitivity.

1.3.1 HH decay channels and Experimental searches

HH processes can result into a variety of final states. Assuming SM Higgs boson branching ratios, Figure 1.3 (right), the possible final states for HH processes are obtained by combining the two Higgs bosons decay channels, as shown in Figure 1.11.

Searching for HH production at the LHC requires to reconstruct the decay products in the detectors and to reject contributions coming from background processes. Since the HH production cross section is rather small, at least in SM predictions, experimental HH searches focus mainly on decay channels with large branching fractions, in order to increase the HH signal rate. The most favourable way is to consider one of the two Higgs bosons decaying into a $b\bar{b}$ pair. Searches in similar channels ($b\bar{b}\tau\tau$, $b\bar{b}\gamma\gamma$) have been performed by the ATLAS and CMS experiments already at the LHC Run I. These channels exploit the large branching fraction

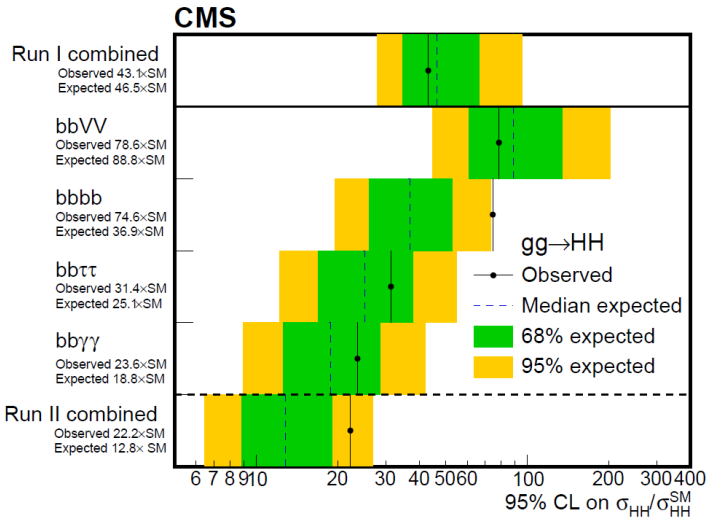

Figure 1.12: 95% CL upper limit on the signal strength modifier $\mu = \sigma_{\mathrm{HH}}/\sigma_{\mathrm{HH}}^{\mathrm{SM}}$ [10].

of the first Higgs decaying into $b\bar{b}$, and the clear signature left by the decay of the other Higgs boson into a pair of photons or tau leptons. Combining the results obtained in Run I in these two channels, the CMS experiment managed to set an upper limit on the HH production cross section of 43 times the SM expectations [35].

In LHC Run II, with the increase of the centre-of-mass energy and thus of the predicted HH production cross section, new opportunities for HH searches became accessible. The CMS collaboration published results obtained with data collected in 2016 probing new HH decay channels ($b\bar{b}b\bar{b}$, $b\bar{b}2\ell 2\nu$) in addition to those already studied in Run I. The $b\bar{b}b\bar{b}$ final state is characterized by the highest branching fraction but it is affected by a large multi-jet background thus it is not the most sensitive channel, especially at lower invariant HH mass regions, but it can profit from the larger signal yield to probe mass regions up to $m_{\mathrm{HH}} \simeq 3$ TeV. On the other hand, the $b\bar{b}2\ell 2\nu$ final state profits from a reduced background contamination, even if it presents a smaller branching fraction.

The strength of HH searches is in the combination. All the final states probed are sensitive to a particular region of the phase space, thus combining the results it is possible to obtain more information about HH production. This can be seen in the combination performed by the CMS experiment with results obtained with 2016 datasets where the combined upper limit on the HH production cross section was improved and set to 22.2 times the SM expectations [10] (Figure 1.12).

In order to explore all the corners of the phase space and combine the results for improving the sensitivity, the ATLAS and CMS experiments are investigating

rarer HH decay channels, like WW$\gamma\gamma$, WWWW, $\tau\tau\tau\tau$, b$\bar{\text{b}}$WW and b$\bar{\text{b}}$ZZ. All these analyses are using the full datasets collected by the experiments during LHC Run II. This way, thanks to the increased statistics of the analysed dataset and to all the diverse information coming from the different channels, the full Run II combined result will set more stringent constraints on the HH production cross section and increase our knowledge on this process.

This thesis is focused on the search for HH non-resonant production in the final state b$\bar{\text{b}}4\ell$ where $\ell = e, \mu$, thus exploiting the higher decay rate of one Higgs boson into the b$\bar{\text{b}}$ pair, and the clean signature of the other Higgs boson decay into four leptons. The analysis is performed with the full Run II dataset, and, eventually, will be included in the combination providing fundamental information on HH process.

Since the analysis is performed in the context of the CMS experiment, the following chapter will briefly illustrate the CMS detector.

Chapter 2

The experimental setup

This thesis is realized using data collected by the CMS experiment, which is one of the four big experiments at the CERN Large Hadron Collider (LHC).

CERN, the European Organization for Nuclear Research, is a scientific laboratory founded in 1954 by 12 European countries to investigate the physics of atomic nuclei. Today the understanding of matter has gone deeper than that of the atomic nucleus, and CERN's main research area is particle physics: the study of fundamental constituents of matter and of the forces acting among them. In order to investigate fundamental interactions, particles are accelerated through a chain of *particle accelerators*, today culminating with the LHC. Then collision products are observed and recorded by *particle detectors*, like the CMS experiment.

2.1 The Large Hadron Collider

The Large Hadron Collider (LHC) [36] is the world's largest and most powerful particle accelerator. It consists in a 27-kilometre two-ring, superconducting accelerator and collider, designed to collide proton beams up to a nominal centre-of-mass energy of $\sqrt{s} = 14$ TeV (i.e. 7 TeV per beam) and an instantaneous luminosity of $10^{34}\,\mathrm{cm^2 s^{-1}}$. The beams travel in opposite directions in separate beam pipes, which are two tubes kept at ultra-high vacuum. Beams are guided around the accelerator ring by strong magnetic fields maintained by superconducting electromagnets made by coils of copper-clad niobium-titanium. Magnets operate in a superconducting state, efficiently conducting electricity without resistance or loss of energy. This requires superfluid helium in order to cool the magnets and maintain them at the operating temperature of 1.9 K ($-271.25°$C). Thousands of magnets of different varieties and sizes are used for various purposes: dipole magnets are used to bend the beams around the accelerator, quadrupole magnets focus the beams and sextupole magnets are used to squeeze the beams further close to the intersection points to maximize the probability of interaction.

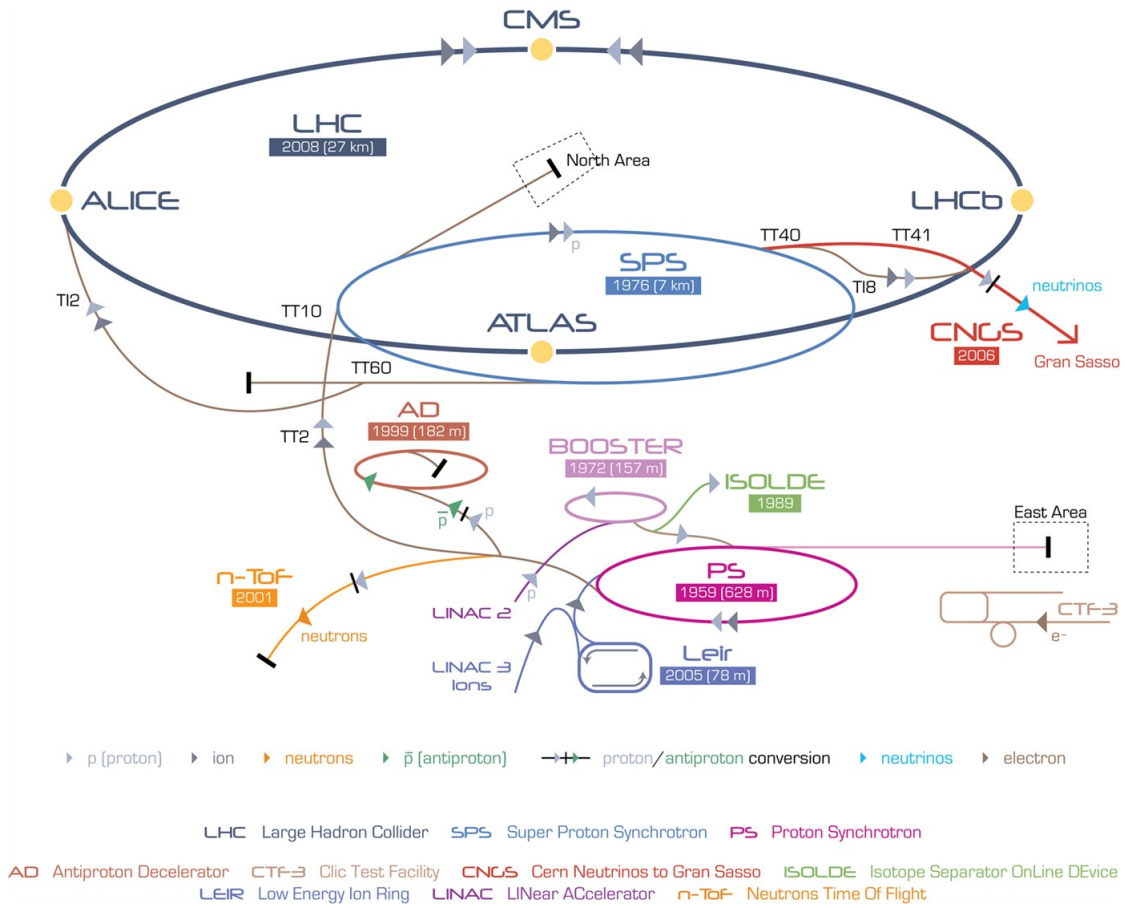

Figure 2.1: The CERN accelerator complex [37]. The proton injection chain for the LHC starts from the LINAC2 and proceeds through the Booster, PS, and SPS.

Before being injected into the LHC the proton beams are prepared by a chain of pre-accelerators which increase their energy in steps. This system is presented in the Figure 2.1 which shows the CERN accelerator complex. Protons are first accelerated to an energy of 50 MeV in the Linear Accelerator (LINAC2), which feeds the Proton Synchrotron Booster (PSB), where protons are accelerated up to 1.4 GeV. Then particles reach 26 GeV in the Proton Synchrotron (PS), and the Super Proton Synchrotron (SPS) further increases their energy to 450 GeV. The protons are finally injected in the two beam pipes of the LHC where one beam circulates clockwise and the second one circulates anti-clockwise, separated in the two beam pipes. It takes about four minutes to fill each LHC ring and about 20 minutes for the protons to reach their maximum energy of 6.5 TeV. Beams circulate for many hours ($\sim$ 13 h) inside the LHC under normal operating conditions. The two beams are brought into collision inside four detectors (ALICE, ATLAS, CMS and LHCb).

Protons are not the only particles accelerated in the LHC. Lead ions for the LHC are taken from a source of vaporized lead and then enter in Linac 3 before being collected and accelerated in the Low Energy Ion Ring (LEIR). They then follow the same journey of the protons to maximum energy. Colliding ions are used to study the physics of strongly interacting matter at extreme energy densities.

Protons circulate in the LHC in bunches spaced by 25 ns (or 7.5 m), thus the bunch crossing rate is 40 MHz. The nominal number of protons per bunch is $N_b = 12 \times 10^{11}$, and the nominal number of bunches per beam is $n_b = 2808$. Under nominal conditions, the number of inelastic collision events is of the order of 10^9 per second, with ~ 20 collisions per bunch crossing.
The LHC instantaneous luminosity depends on the beam parameters and can be written as:

$$L = \frac{f_{\text{rev}}\, N_b^2\, n_b\, \gamma_r}{4\pi\, \epsilon_n\, \beta^*} F \tag{2.1}$$

where $f_{\text{rev}} = 11\,\text{kHz}$ is the revolution frequency, ϵ_n the normalized transverse beam emittance, $\beta^* = 0.55\,\text{m}$ is the nominal value of the beta function at the collision point, which measures the beam focalization and is corrected by the relativistic gamma factor γ_r, and F is a geometric luminosity reduction factor that accounts for the crossing angle at the interaction point.
The nominal instantaneous luminosity of LHC is $10^{34}\,\text{cm}^2\text{s}^{-1}$. Thanks to this, the integrated luminosity (which is a measure of the total amount of collisions produced) collected by the CMS experiment in the Run II period is 35.8 fb^{-1} in 2016, 41.5 fb^{-1} in 2017, and 59.7 fb^{-1} in 2018. These are the samples considered for the analysis presented in this thesis in the following chapters.

Four main particle detectors are installed in underground caverns at the four intersection points of the beams. The two largest ones, ATLAS (*A Toroidal LHC ApparatuS*) and CMS (*Compact Muon Solenoid*) are designed to cover a wide physics program in the scalar, electroweak, and strong sectors, with optimized sensitivity for Higgs bison searches and additional possible new physics at the TeV scale. The two other detectors are LHCb (*LHC beauty*), which is aimed at studying CP violation in B-hadrons, and ALICE (*A Large Ion Collider Experiment*), which is dedicated to heavy-ion collisions in order to study the quark-gluon-plasma.
This thesis is performed in the context of the CMS experiment, presented in the following section.

2.2 The Compact Muon Solenoid experiment

The CMS detector layout is organized around a superconducting solenoid magnet of 6 m internal diameter and 12.5 m length, which provides a large magnetic

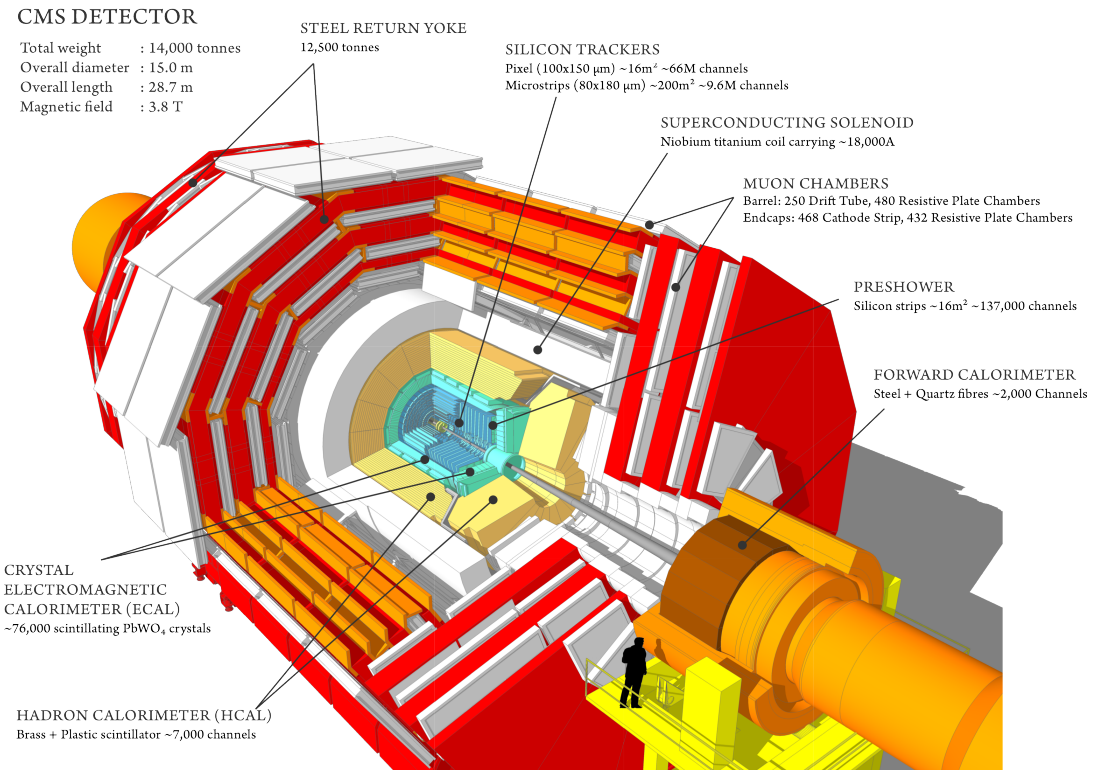

Figure 2.2: A perspective view of the CMS detector, illustrating its major subsystems.

field of 3.8 T. The overall apparatus is rather compact: it materializes as a 21.6-metre-long, 14.6-metre-wide, 14000-tonne cylinder around the LHC beam axis. Within the solenoid volume there are three major subsystems: a silicon pixel and strip *tracker* which measures the trajectories of charged particles, a lead tungstate crystal *electromagnetic calorimeter* (ECAL) that mainly collects the energies of electrons and photons, and a brass and scintillator *hadronic calorimeter* (HCAL) which stops the more penetrating hadrons. Some *forward calorimeters* further improve hermeticity. The measurement of muons relies on a combination of inner tracking and information from the *muon chambers*, which are gas-ionization detectors embedded in the steel flux-return yoke outside the solenoid. The overall layout of the detector is shown in Figure 2.2. A detailed description of the CMS detector can be found in Ref [38].

2.2.1 The coordinate system

A right-handed Cartesian coordinate system is used to describe the CMS detector. The origin of the coordinate system is located at the nominal collision point. The z axis coincides with the proton beam direction, the y axis points vertically upward,

and the x axis points radially inward towards the centre of the LHC ring.
Since the detector has a cylindrical structure, a polar coordinate system is also used. The azimuthal angle ϕ is defined from the x axis in the xy (*transverse*) plane and it takes values between $-\pi$ and π. The radial coordinate in the transverse plane is denoted as r. The polar angle θ is defined from the z axis in the rz plane and assumes values from 0 to π. Usually the polar coordinate is quoted using another variable, the *pseudorapidity*, defined as $\eta = -\ln[\tan(\theta/2)]$. The spatial separation of two particles can be expressed in terms of their angular distance $\Delta R = \sqrt{(\Delta\eta)^2 + (\Delta\phi)^2}$.

The projection of the momentum of a particle on the transverse plane, the *transverse momentum* p_{T}, as well as the *transverse energy* E_{T}, are defined using the components of the momentum and energy in the xy plane:

$$\begin{aligned} p_{\mathrm{T}} &= \sqrt{p_x^2 + p_y^2} \\ E_{\mathrm{T}} &= \sqrt{m^2 + p_{\mathrm{T}}^2} \end{aligned} \tag{2.2}$$

where m is the mass of the particle and p_x and p_y are the x and y components of the particle momentum, respectively.
Consequently, the *missing transverse energy* $E_{\mathrm{T}}^{\mathrm{miss}}$ is defined as the the imbalance of the total transverse energy measurement in a collision.
Detectors are composed by a central part called the *barrel* and two opposite forward parts denoted as *endcaps*. These parts cover different acceptance regions (in the η coordinate) depending on the subsystem.

2.2.2 The trigger system

The CMS trigger system relies on two successive levels:

- The first level, the *Level-1 trigger* (L1), performs a fast readout of the detector, selecting events that contain distinctive detector signals such as ionization deposits consistent with a muon, or energy clusters compatible with an electron or a photon.
- The second level, the *High Level Trigger* (HLT), is implemented in software and performs a full readout of the CMS detector. Events are reconstructed with similar algorithms as those used in the off-line analysis, with progressive selection steps in order to allow more sophisticated and time consuming algorithms to be applied over a smaller fraction of events. All main classes of physics objects can be reconstructed at HLT, like electrons, muons or photons, and specific selection criteria are applied on these objects in order to keep the rate under control and select the subset of events relevant to subsequent data analysis.

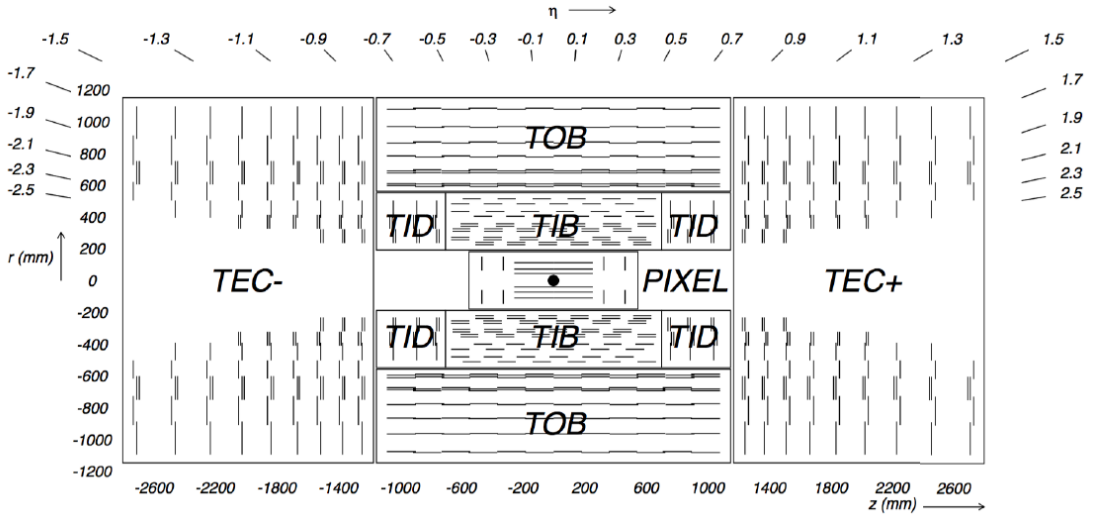

Figure 2.3: Schematic longitudinal section of the CMS tracker, showing inner pixel detector with its barrel and endcap modules, and the strip detector with two collections of barrel modules, the tracker inner barrel (TIB) and the tracker outer barrel (TOB), and two collections of endcap modules, the tracker inner discs (TID) and the tracker endcaps (TEC) [38].

2.2.3 The tracking system

The tracker is the most inner detector of the CMS Experiment. It surrounds the interaction point, has a length of 5.8 m and a diameter of 2.5 m. Thanks to the uniform magnetic field within its volume, this detector, which is designed to provide a precise and efficient measurement of the trajectories of charged particles emerging from the LHC collisions, provides also a measurement of the momentum of these charged particles. The spacial measurement provided by the tracking system allows also the determination of the hard scattering interaction point, the *primary vertex*, and its discrimination against pileup interactions. It also allows the reconstruction of in-flight decays and the determination of *secondary vertices*. To fulfil a requirement of precise spatial measurement while being exposed to a large flux of particles, the tracking detector is finely segmented and equipped with fast readout on-board electronics. Furthermore, the amount of material has to be kept to the minimum, in order to limit phenomena such as multiple scattering, bremsstrahlung and photon conversion which complicate particle reconstruction.
The silicon detector technology used in the CMS tracking system addresses these needs by providing a large surface of thin, finely segmented, active detectors. The overall layout of this system is shown in Figure 2.3.
The CMS tracker is based on two types of sensors: *silicon pixel sensors* of size $100 \times 150\,\mu\text{m}^2$ displayed on three cylindrical barrel layers and on two endcap disk

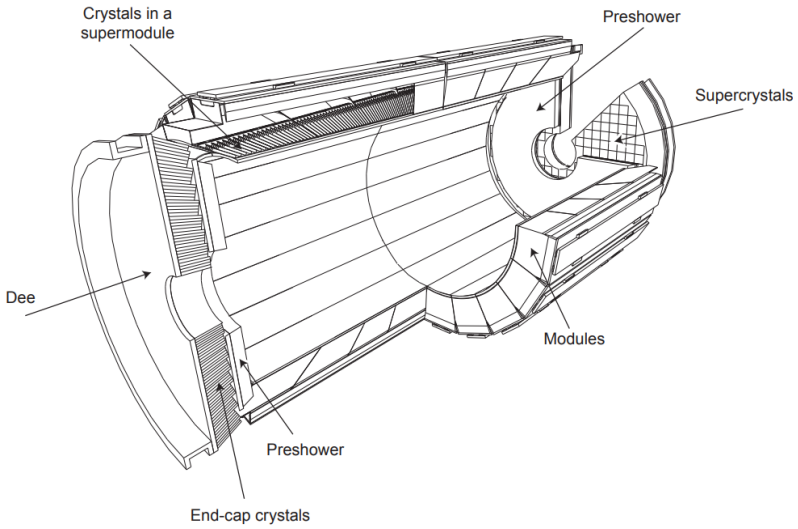

Figure 2.4: Layout of the CMS electromagnetic calorimeter showing the arrangement of crystal modules, supermodules and endcaps, with the preshower in front [38].

layers, and *silicon strip sensors* displaced in the rest of the tracker, arranged in 10 barrel layers and 12 endcap layers. The tracker detector covers a pseudorapidity range of $|\eta| < 2.5$ allowing the measurement of all the charged particles within this range. The strip tracker and pixel detectors are operated at temperatures of about $-15°C$ and $-20°C$, respectively, in order to minimize the damage caused by ionizing radiations and to absorb the heat produced by on-board electronics. In 2017 the pixel detector was upgraded [39], providing an additional pixel layer both in the barrel and in the andcaps, improving the detector performances.

2.2.4 The electromagnetic calorimeter

The electromagnetic calorimeter (ECAL) is designed to provide the measurement of incoming electrons and photons energies. It is a hermetic homogeneous calorimeter made of scintillating crystals of lead tungstate ($PbWO_4$). Thanks to the short radiation length (0.89 cm) and the high density of this material, electromagnetic showers can be absorbed within relatively short distance, while the small Molière radius (2.2 cm) allows a good shower separation to be obtained. The 80% of the scintillation light is emitted in 25 ns and this allows a detector response fast enough to face the LHC bunch spacing. The ECAL general structure is shown in Figure 2.4.
The barrel part of the ECAL (EB) covers the pseudorapidity range $|\eta| < 1.479$ and it is made of crystal of length 230 mm and and frontal cross section $22 \times 22\,\mathrm{mm}^2$ organized in 36 *supermodules* which cover half of the barrel length and 20° in ϕ.

Each supermodule is made of four *modules* which contain 400 or 500 crystals in an alveolar structure. The ECAL endcaps (EE), instead, cover the pseudorapidity range $1.479 < |\eta| < 3.0$ and are made of crystals with length 220 cm and frontal cross section $28.62 \times 28.62\,\mathrm{mm}^2$ organized in two semi-circular *dees* containing 3662 crystals.
The crystals are mounted in a quasi-projective geometry, so that their axes make a 3° angle with respect to the direction of the nominal interaction point in both the η and ϕ projections, thus avoiding the alignment of inter-crystal gaps with particle trajectories.
The scintillation light from ECAL crystals is read by fast, radiation-tolerant *photodetectors* which can operate inside the CMS magnetic field and are insensitive to particles traversing them.

Two *preshower* detectors are installed at each end of the tracker detector, in front of the ECAL endcaps, in order to help distinguishing $\pi^0 \to \gamma\gamma$ decays from single photons and identifying electrons against minimum ionizing particles. These sampling calorimeters are made of a lead radiator layer which initiates electromagnetic showers from incoming particles, followed by silicon strip sensors that measure the deposited energy.

Although lead tungstate crystals are radiation resistant, they undergo a limited but rapid loss of optical transmission under irradiation. This phenomenon depends on the luminosity and crystal pseudorapidity, and is partly balanced by an annealing effect. This effect is measured and it is taken into account by time-dependent corrections applied to the measured particle energies.

2.2.5 The hadronic calorimeter

Hadrons typically traverse the ECAL volume without being stopped. The hadronic calorimeter (HCAL) is designed to absorb them and measure their energy. The CMS HCAL is an essential element in the reconstruction of final states containing hadronic jets or non-interacting particles like neutrinos, where the calorimeter hermeticity and geometrical coverage allows the missing energy in the event to be determined. Hadron energies, however, are intrinsically more difficult to measure from hadron showers in HCAL, in comparison to electron and photon interactions in ECAL.
The structure of the CMS HCAL is illustrated in Figure 2.5. The HCAL barrel (HB) is located between the outer extent of the EB and the inner extent of the magnet coil. This extension is not enough to fully absorb the hadronic showers, therefore an outer hadron calorimeter (HO) is placed outside of the solenoid. The HCAL barrel covers a pseudorapidity range $|\eta| < 1.3$, which the HCAL endcaps (HE) extend to $|\eta| < 3.0$. In addition, two forward hadron calorimeters (HF) are located 11.2 m away from the interaction point and extend the pseudorapidity

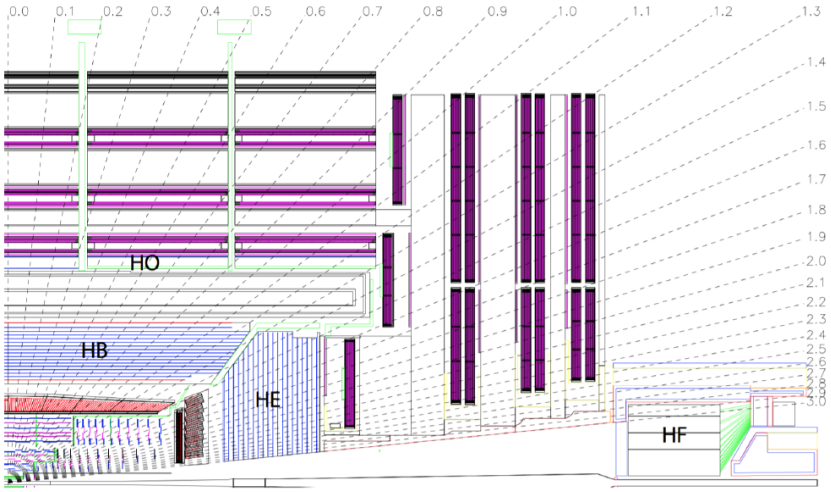

Figure 2.5: Longitudinal section of a quarter of the CMS detector, showing the locations of the hadron barrel (HB), endcap (HE), outer (HO) and forward (HF) calorimeters [38].

coverage up to $|\eta| < 5.2$, thus ensuring good hermeticity.
The CMS HCAL is a sampling calorimeter. In the HB and HE, brass layers are used as the absorber material and are interspersed with plastic scintillator tiles which are the active material. The HB and HE calorimeter cells are grouped in projective towers and the scintillation light is converted by wavelength-shifting fibres embedded in the scintillator tiles and detected by hybrid photodiodes. The HFs instead has to sustain a harsher radiation environment therefore quartz fibres are used as active material. They are placed between steel absorber plates and emit Cherenkov light, which is detected by photomultipliers.

2.2.6 The muon system

Muons produced in collisions at the LHC usually traverse the ECAL, the HCAL, and the solenoid volumes without being stopped and are identified and measured in the muon detectors located in the outermost part of CMS.
As shown in Figure 2.6 the muons system is made of *muon chambers* embedded in the iron return yoke of the CMS magnet and it is divided into a cylindrical barrel section and two planar endcap regions.
Three types of gas-ionization chambers are used in this system: *Drift Tubes*, *Cathode Strip Chambers* and *Resistive Plate Chambers*.

The *Drift Tubes* (DTs) are located in the barrel region, where the muon rate is lower, and the magnetic field is quite uniform, and cover a pseudorapidity range of $|\eta| < 1.2$. The DTs are organized into four stations interspersed among the

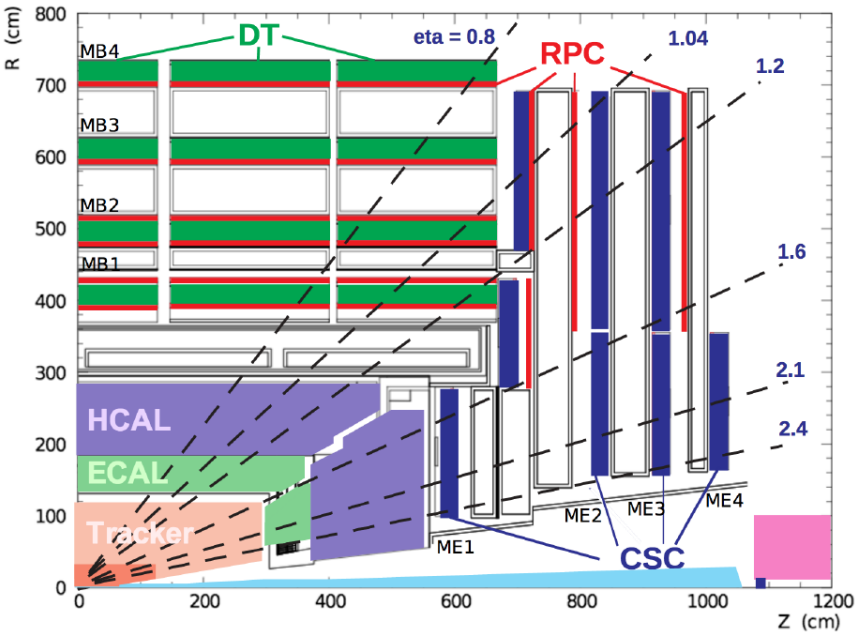

Figure 2.6: Longitudinal section of a quarter of the CMS detector, showing the four DT stations in the barrel (MB1-MB4, green), the four CSC stations in the endcap (ME1-ME4, blue), and the RPC stations (red) [40].

layers of the flux return plates. Their basic constituents are rectangular drift cells bounded by two parallel aluminium planes, which serve as cathodes. Anodes are 80 μm stainless steel wires located in the centre of each cell. A muon passing through a cell ionises the gas mixture that fills the cell volume. The drift time of the resulting electrons is then used to measure the distance between the muon track and the wire. Each chamber has a resolution of 100 μm in the $r - \phi$ plane.

The *Cathode Strip Chambers* (CSCs) are used in the endcaps, where the the muon rates and background levels are higher and the magnetic field is large and non uniform, and cover a pseudorapidity range of $0.9 < |\eta| < 2.4$. The CSCs are multiwire proportional chambers, made of 6 anode wire planes interleaved among 7 cathode panels, with the wires running approximately perpendicular to the strips. A muon passing through a chamber generates an avalanche, inducing a charge on several cathode strips. The ensuing interpolation allows a spatial resolution of 50 μm to be obtained. Four stations of CSCs are located in each endcap. The chambers are positioned perpendicular to the beam line and interspersed between the magnetic field flux return plates.

The *Resistive Plate Chambers* (RPCs) are located both in the barrel and in the

endcaps and cover the pseudorapidity range $|\eta| < 1.6$. The RPCs are double-gap chambers which operate in avalanche mode and are disposed in six layers in the barrel and three layers in the endcaps. They provide a complementary trigger system with moderate spatial resolution but excellent time resolution (of the order of 1 ns), which helps measuring the correct beam-crossing time.

2.2.7 Events and particle reconstruction

Collision events recorded by the CMS detector are reconstructed exploiting the combined information collected by the different subsystems, in order to improve the identification of the final state particles and the reconstruction of their properties. This global-reconstruction approach is implemented in the *particle-flow* (PF) algorithm [41], which takes as input the raw data collected by the CMS subsystems and combines the information from all the different detectors to reconstruct *physics objects*, performing a global event reconstruction. The reconstructed physics objects are articulated in charged and neutral hadrons, photons, electrons, and muons, and constitute the inputs for all the data analyses performed. In addition, these PF candidates are used to build more complex observables such as jets and missing transverse energy.
Figure 2.7 shows examples of the signatures that the different particles leave inside the CMS detector subsystems. Each type of particle leaves a typical signature that involves different subsystems, for example electrons leave hits in the tracker system and also deposits in the ECAL, while charged hadrons leave similarly hits in the tracking system but a deposit in the HCAL; photons instead do not interact with the tracking system but leave a deposit in the ECAL. The combination of information from different subsystems, therefore, allows a better identification and reconstruction of the particles traversing the detectors.
The following sections consider the reconstruction of the physics objects used in the analysis, such as muons and electrons (coming from the decay of $H \to ZZ \to 4\ell$), and jets (from the $H \to b\bar{b}$ decay).

Muon reconstruction

Muons are reconstructed in the CMS detector with high efficiency and purity, thanks to the clear signature they leave in the muon spectrometer and in the inner tracking system. The purity is granted by the upstream calorimeters that absorb other particles (except neutrinos), while the inner tracker provides a precise measurement of the muon momentum.
Muon physics objects are reconstructed with dedicated algorithms combining information from different subsystems. The final collection is composed by three different muon types:

- *Standalone muons* built exploiting only information from the outer muon

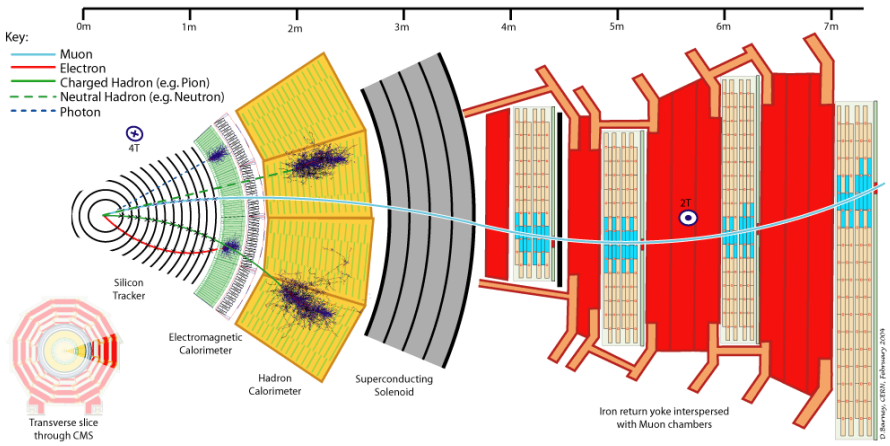

Figure 2.7: Schematic of the specific particle interactions in a transverse slice of the CMS detector [41].

system; patterns from DT, CSC and RPC detectors are combined and fitted into *standalone-muon tracks*.

- *Global muons* built propagating standalone-muon tracks inward to the inner tracker. If a matching track reconstructed in the inner tracking system is found, the hits of the two matched tracks are combined and fitted into a *global-muon track*.
- *Tracker muons* built by extrapolating inner tracker tracks outward to the outer muon system, requiring that at least one muon track segment made of hits in the DTs or CSCs matches the extrapolated track. The possibility for tracker muons to have one single matched segment in the muon system makes this algorithm more efficient than global-muon reconstruction at low momentum ($p_T \lesssim 5\,\text{GeV}$).

Thanks to the high efficiency of the inner track and muon segment reconstruction, about 99% of the muons produced in the detector acceptance are reconstructed. Global muons and tracker muons that share the same inner track are merged into a single candidate.
The charge and momentum are reconstructed from the tracker track for muons of $p_T < 200\,\text{GeV}$, since the precision of the muon system measurement at low momentum is limited by multiple scattering. For muons with $p_T > 200\,\text{GeV}$, charge and momentum are extracted from the global fit.

Electron reconstruction

Electrons deposit most of their energy in the ECAL, but they also leave hits in the inner tracker. Electron reconstruction in CMS therefore uses an algorithm that

combines the inputs from both subsystems. It associates a reconstructed track with a cluster of energy in the ECAL and exploits both sides of the information to estimate the electron momentum.
The electron reconstruction is complicated by their interaction with the inner tracker material located between the collision point and the ECAL. This causes significant bremsstrahlung along the electron trajectory, with the resulting photons possibly converting to electron pairs. Electron reconstruction algorithms must take into account these effects.

Since the electron energy usually spreads over several crystals of the ECAL, the first reconstruction step consists in clustering the energy deposits. The algorithm used consists in subsequent steps. Firstly the *cluster seeds* are identified as local crystal energy maxima above a given threshold, then *topological clusters* are grown from the seeds by aggregating crystals with at least one side in common with a crystal already in the cluster, and with an energy exceeding a defined threshold. A topological cluster gives rise to as many PF *clusters* as seeds. Lastly, the energy of each cell is shared among all PF clusters according to the cell-cluster distance, with an iterative determination of cluster energies and positions. PF clusters are then assembled into PF *superclusters*, starting from a seed cluster and gathering the presumptive clusters of bremsstrahlung photons and conversions products.

Electron tracks are reconstructed with a dedicated tracking procedure, different from the one used for other charged particles, because electrons loose a larger amount of energy in the tracker and this causes changes in the curvature. The tracker procedure is preceded by a *seeding* procedure that consists in finding and selecting the two or three first hits in the tracker from which the track can be initiated. Then the track building proceeds iteratively from the track parameters provided in each layer, modelling the electron energy loss with a Bethe-Block function. To maintain good efficiency in the presence of bremsstrahlung, compatibility requirements between the predicted and the found hits in each layer are quite loose. If several hits are compatible with the predicted one, different trajectory candidates are created and developed, with a limit of five candidate trajectories for each layer. At most one missing hit is allowed per each trajectory. Once the hits are collected, the track parameters are estimated with a fit that uses a Gaussian Sum Filter (GSF) [42], instead of the Kalman Filter (KF) [43] used for non-electron tracks.

In the end, a refining procedure is applied to the PF superclusters and some loose requirements are applied to the variables that characterize the geometrical association between the track and the supercluster. Charge estimation is then performed and the final step is the estimation of electron momentum, which relies on a combination of the energy of the supercluster and the momentum estimate of the GSF track.

Jet reconstruction

Jets, product of the hadronization of quarks and gluons, are reconstructed by clustering the PF candidates with the anti-k_T algorithm [44]. This algorithm iteratively combines PF candidates close to each other, clustering them around the hardest particle in the event in order to produce jets of an approximate conic shape. The size of the jet cone is defined by the distance parameter R, at which the algorithm is operated. Jets considered in this analysis have $R = 0.4$.
The anti-k_T algorithm is resilient against infrared and collinear effects.
The jet momentum is computed as the vectorial sum of all particle momenta in the jet, and a set of corrections are applied to calibrate the jet response using the information of generated particles in simulations.

Chapter 3

HH search in the 4lbb final state

This thesis focuses on the search for HH production in the decay channel where one of the two Higgs bosons decays into four leptons (muons or electrons) through the ZZ* decay, while the other one decays into a pair of b quarks that hadronize into jets.
Considering all the possible decay of the Higgs boson, a wide variety of HH decays is possible. A large number of them has been studied by the ATLAS [45, 46, 47, 48, 49, 50] and CMS [51, 52, 35, 53, 54] collaborations, using data collected in Run I and in the first part of Run II.
The $4\ell b\bar{b}$ ($\ell = e, \mu$) final state is one of those that have not been investigated previously, because of its smaller branching fraction with respect to the leading decay channels. These secondary decay modes of HH require a larger quantity of data in order to be investigated. The Higgs to four lepton decay channel, where leptons are either electrons or muons, is, in fact, the rarest decay mode observed so far at the LHC, but is also has the largest signal-to-background ratio and presents a very clean signature. On the other hand, the Higgs boson decay into two b quarks has the highest branching fraction among Higgs boson decays.
The analysis presented in this thesis is thus significant as it investigates a HH decay channel never studied before. This was possible thanks to the larger amount of data available from LHC Run II and to the application of advanced analysis techniques.
In the $4\ell b\bar{b}$ final state we can exploit the clear signature granted by the four-lepton decay mode and the large branching fraction of the bb decay channel, that partially compensate for the small branching ratio of the four lepton channel.
This analysis is the first HH search in CMS to produce results with the full Run II dataset. The results obtained will provide essential information for the combination that will be performed collecting the results from all HH decays, in order to improve the constraint on the HH observables, as mentioned in Section 1.3.1.

This chapter reports the datasets used for the analysis, and illustrates the trigger

requirements and the procedure adopted to select the physics objects employed in the analysis.

3.1 Trigger requirements

The final state considered by the analysis reported in this thesis consists of two pairs of opposite-charged isolated leptons (muons or electrons) and at least two jets. The analysis strategy consists in first selecting the four leptons coming from the decay of the first Higgs boson and then add requirements for selecting two jets, originating from the decay of the second Higgs.
The online events selection is based on a set of inclusive lepton triggers, requiring the presence of one, two or three muons or electrons in the event. No trigger requirements are set on jets, since requiring combinations of inclusive lepton triggers already grants a very high trigger efficiency, close to 1 for events with four leptons inside the detector acceptance [55, 56, 57]. It is therefore not necessary to require additional triggers on jets to improve the trigger efficiency, nor to introduce exclusive triggers for this particular decay channel.

A HLT path consists of several steps made by software modules. The present analysis makes use of HLT paths to select events which present a certain number of electrons or muons in the final state. Due to the evolution of trigger requirements with instantaneous LHC luminosity, the collection of HLT paths used in this analysis is different for each data taking year. The three sets used match those adopted in the $H \to ZZ^* \to 4\ell$ analysis [55, 56, 57]. The collections used are designed and optimized to cover the phase space of the 4ℓ Higgs boson decay. In order to model the trigger response in MC to be the same as in data, the set of triggers applied to data is emulated in MC samples.
The HLT paths used for the 2016, 2017 and 2018 collisions, are listed in Table 3.1,3.2,3.3, respectively.
They are grouped according to the kind of event selected. The *DiEle* triggers select events containing in the final state at least two electrons above given transverse momentum (p_T) thresholds. Similarly, *TriEle* triggers target events containing three electrons above certain p_T thresholds. *DiMuon* and *TriMuon* triggers target events with at least two and three muons passing given p_T thresholds, respectively, while *MuEle* triggers select events containing in the final state at least one muon and one electron, satisfying given p_T requirements. *SingleMuon* triggers select events with at least one muon passing given p_T requirements, while *SingleElectron* triggers select events containing in the final state at least one electron above given p_T thresholds. Each trigger path in these groups additionally requires the event to satisfy conditions regarding particle identification from the sub-detector systems. For example the HLT HLT_Ele17_Ele12_CaloIdL_TrackIdL_IsoVL_DZ selects events with two electrons, one with $p_T > 17\,\text{GeV}/c$ and the other with $p_T > 12\,\text{GeV}/c$ that

pass the identification in the ECAL and in the tracker detector, and appear to be isolated with respect to other particles.

The analysis relies on different *Primary Datasets* (PDs), each of which combines a certain collection of high-level trigger (HLT) paths. Events considered for the analysis are taken from the PDs following a specific sequence, in order to avoid duplicate events from different PDs. The PDs used in the analysis are reported in Table 3.1,3.2,3.3, together with the associated HLT paths.
For 2016 and 2017 datasets, five PDs are used (*DoubleEG*, *DoubleMuon*, *MuEG*, *SingleElectron*, *SingleMuon*) and events are taken from the PDs as follow:

- from DoubleEG, if they pass the diEle or triEle triggers,
- from DoubleMuon, if they pass the diMuon or triMuon triggers and fail the diEle and triEle triggers,
- from MuEG, if they pass the MuEle or MuDiEle or DiMuEle triggers and fail the diEle, triEle, diMuon, and triMuon triggers,
- from SingleElectron, if they pass the singleElectron trigger and fail all the above triggers,
- from SingleMuon, if they pass the singleMuon trigger and fail all the above triggers.

For 2018 datasets, instead, four PDs are used (*DoubleMuon*, *MuEG*, *EGamma*, *SingleMuon*) and events are taken from the PDs as follow:

- from EGamma, if they pass the diEle or triEle or singleElectron triggers,
- from DoubleMuon, if they pass the diMuon or triMuon triggers and fail the diEle and triEle triggers,
- from MuEG, if they pass the MuEle or MuDiEle or DiMuEle triggers and fail the diEle, triEle, singleElectron, diMuon, and triMuon triggers,
- from SingleMuon, if they pass the singleMuon trigger and fail all the above triggers.

The efficiency of the combination of triggers used in the analysis with respect to the offline reconstruction and selection is measured in data and MC simulations using a Tag-and-Probe technique [58]. The measurement is performed considering 4ℓ events triggered by single lepton triggers. One of the four reconstructed leptons (the "tag") is geometrically matched to a trigger-level lepton that fires a single-muon or single-electron path. The other three leptons are used as "probe". In each 4ℓ event there are four possible combinations of one tag and three probes, and all of them are counted in the denominator of the efficiency. A set of probes

Table 3.1: Trigger paths used in 2016 collisions. The convention for path and primary dataset names is explained in the text.

HLT path	primary dataset
HLT_Ele17_Ele12_CaloIdL_TrackIdL_IsoVL_DZ	DoubleEG
HLT_Ele23_Ele12_CaloIdL_TrackIdL_IsoVL_DZ	DoubleEG
HLT_DoubleEle33_CaloIdL_GsfTrkIdVL	DoubleEG
HLT_Ele16_Ele12_Ele8_CaloIdL_TrackIdL	DoubleEG
HLT_Mu17_TrkIsoVVL_Mu8_TrkIsoVVL	DoubleMuon
HLT_Mu17_TrkIsoVVL_TkMu8_TrkIsoVVL	DoubleMuon
HLT_TripleMu_12_10_5	DoubleMuon
HLT_Mu8_TrkIsoVVL_Ele17_CaloIdL_TrackIdL_IsoVL	MuonEG
HLT_Mu8_TrkIsoVVL_Ele23_CaloIdL_TrackIdL_IsoVL	MuonEG
HLT_Mu17_TrkIsoVVL_Ele12_CaloIdL_TrackIdL_IsoVL	MuonEG
HLT_Mu23_TrkIsoVVL_Ele12_CaloIdL_TrackIdL_IsoVL	MuonEG
HLT_Mu23_TrkIsoVVL_Ele8_CaloIdL_TrackIdL_IsoVL	MuonEG
HLT_Mu8_DiEle12_CaloIdL_TrackIdL	MuonEG
HLT_DiMu9_Ele9_CaloIdL_TrackIdL	MuonEG
HLT_Ele25_eta2p1_WPTight	SingleElectron
HLT_Ele27_WPTight	SingleElectron
HLT_Ele27_eta2p1_WPLoose_Gsf	SingleElectron
HLT_IsoMu20 OR HLT_IsoTkMu20	SingleMuon
HLT_IsoMu22 OR HLT_IsoTkMu22	SingleMuon

is then counted in the numerator whenever the three corresponding trigger-level leptons fire at least one of the 4ℓ-dedicated paths. The trigger efficiency is found to be $\geq 98\%$ in both data and simulation.
Using a combination of triggers allows us to take advantage from characteristics of all the triggers and improve the overall trigger efficiency, since triggers which require less leptons suffer less from trigger reconstruction inefficiency, despite their higher thresholds.

3.2 Datasets used

3.2.1 Data samples

The analysis is performed using pp collision data collected by the CMS experiment at a centre-of-mass energy $\sqrt{s} = 13$ TeV during the years 2016, 2017, and 2018. These datasets correspond to a total integrated luminosity of 137 fb^{-1}.
The data samples used in 2016, 2017, and 2018 are listed in Table 3.4,3.5,3.6, respectively.

3.2.2 Signal and background simulation samples

Monte Carlo generators are used to simulate background and signal predictions, both in SM and BSM scenarios. The simulated samples are used to optimize

Table 3.2: Trigger paths used in 2017 collisions. The convention for path and primary dataset names is explained in the text.

HLT path	primary dataset
HLT_Ele23_Ele12_CaloIdL_TrackIdL_IsoVL_	DoubleEG
HLT_DoubleEle33_CaloIdL_GsfTrkIdVL	DoubleEG
HLT_Ele16_Ele12_Ele8_CaloIdL_TrackIdL	DoubleEG
HLT_Mu17_TrkIsoVVL_Mu8_TrkIsoVVL_DZ_Mass3p8	DoubleMuon
HLT_Mu17_TrkIsoVVL_Mu8_TrkIsoVVL_DZ_Mass8	DoubleMuon
HLT_TripleMu_12_10_5	DoubleMuon
HLT_TripleMu_10_5_5_D2	DoubleMuon
HLT_Mu23_TrkIsoVVL_Ele12_CaloIdL_TrackIdL_IsoVL	MuonEG
HLT_Mu8_TrkIsoVVL_Ele23_CaloIdL_TrackIdL_IsoVL_DZ	MuonEG
HLT_Mu12_TrkIsoVVL_Ele23_CaloIdL_TrackIdL_IsoVL_DZ	MuonEG
HLT_Mu23_TrkIsoVVL_Ele12_CaloIdL_TrackIdL_IsoVL_DZ	MuonEG
HLT_DiMu9_Ele9_CaloIdL_TrackIdL_DZ	MuonEG
HLT_Mu8_DiEle12_CaloIdL_TrackIdL	MuonEG
HLT_Mu8_DiEle12_CaloIdL_TrackIdL_DZ	MuonEG
HLT_Ele35_WPTight_Gsf_v	SingleElectron
HLT_Ele38_WPTight_Gsf_v	SingleElectron
HLT_Ele40_WPTight_Gsf_v	SingleElectron
HLT_IsoMu27	SingleMuon

Table 3.3: Trigger paths used in 2018 collisions. The convention for path and primary dataset names is explained in the text.

HLT path	primary dataset
HLT_Ele23_Ele12_CaloIdL_TrackIdL_IsoVL_v*	EGamma
HLT_DoubleEle25_CaloIdL_MW_v*	EGamma
HLT_Ele32_WPTight_Gsf_v*	EGamma
HLT_Mu17_TrkIsoVVL_Mu8_TrkIsoVVL_DZ_Mass3p8_v*	DoubleMuon
HLT_TripleMu_10_5_5_DZ_v*	DoubleMuon
HLT_TripleMu_12_10_5_v*	DoubleMuon
HLT_Mu23_TrkIsoVVL_Ele12_CaloIdL_TrackIdL_IsoVL_v*	MuEG
HLT_Mu8_TrkIsoVVL_Ele23_CaloIdL_TrackIdL_IsoVL_DZ_v*	MuEG
HLT_Mu12_TrkIsoVVL_Ele23_CaloIdL_TrackIdL_IsoVL_DZ_v*	MuEG
HLT_Mu23_TrkIsoVVL_Ele12_CaloIdL_TrackIdL_IsoVL_DZ_v*	MuEG
HLT_DiMu9_Ele9_CaloIdL_TrackIdL_DZ_v*	MuEG
HLT_Mu8_DiEle12_CaloIdL_TrackIdL_DZ_v*	MuEG
HLT_IsoMu24_v*	SingleMuon

Table 3.4: 2016 data samples used in the analysis, corresponding to an integrated luminosity of 35.8 fb^{-1}. The sample names correspond to the sample labels in the CMS database system and contain the information on the data taking conditions and on the reprocessing version of the samples used in the analysis.

Run-range	Dataset
273150-275376	/DoubleMuon/Run2016B-17Jul2018-ver2-v1/MINIAOD /DoubleEG/Run2016B-17Jul2018-ver2-v1/MINIAOD /MuonEG/Run2016B-17Jul2018-ver2-v1/MINIAOD /SingleElectron/Run2016B-17Jul2018-ver2-v1/MINIAOD /SingleMuon/Run2016B-17Jul2018-ver2-v1/MINIAOD
275656-276283	/DoubleMuon/Run2016C-17Jul2018-v1/MINIAOD /DoubleEG/Run2016C-17Jul2018-v1/MINIAOD /MuonEG/Run2016C-17Jul2018-v1/MINIAOD /SingleElectron/Run2016C-17Jul2018-v1/MINIAOD /SingleMuon/Run2016C-17Jul2018-v1/MINIAOD
276315-276811	/DoubleMuon/Run2016D-17Jul2018-v1/MINIAOD /DoubleEG/Run2016D-17Jul2018-v1/MINIAOD /MuonEG/Run2016D-17Jul2018-v1/MINIAOD /SingleElectron/Run2016D-17Jul2018-v1/MINIAOD /SingleMuon/Run2016D-17Jul2018-v1/MINIAOD
276831-277420	/DoubleMuon/Run2016E-17Jul2018-v1/MINIAOD /DoubleEG/Run2016E-17Jul2018-v1/MINIAOD /MuonEG/Run2016E-17Jul2018-v1/MINIAOD /SingleElectron/Run2016E-17Jul2018-v1/MINIAOD /SingleMuon/Run2016E-17Jul2018-v1/MINIAOD
277932-278808	/DoubleMuon/Run2016F-17Jul2018-v1/MINIAOD /DoubleEG/Run2016F-17Jul2018-v1/MINIAOD /MuonEG/Run2016F-17Jul2018-v1/MINIAOD /SingleElectron/Run2016F-17Jul2018-v1/MINIAOD /SingleMuon/Run2016F-17Jul2018-v1/MINIAOD
278820-280385	/DoubleMuon/Run2016G-17Jul2018-v1/MINIAOD /DoubleEG/Run2016G-17Jul2018-v1/MINIAOD /MuonEG/Run2016G-17Jul2018-v1/MINIAOD /SingleElectron/Run2016G-17Jul2018-v1/MINIAOD /SingleMuon/Run2016G-17Jul2018-v1/MINIAOD
281207-284068	/DoubleMuon/Run2016H-17Jul2018-v1/MINIAOD /DoubleEG/Run2016H-17Jul2018-v1/MINIAOD /MuonEG/Run2016H-17Jul2018-v1/MINIAOD /SingleElectron/Run2016H-17Jul2018-v1/MINIAOD /SingleMuon/Run2016H-17Jul2018-v1/MINIAOD

Table 3.5: 2017 data samples used in the analysis, corresponding to an integrated luminosity of 41.5 fb^{-1}. The sample names correspond to the sample labels in the CMS database system and contain the information on the data taking conditions and on the reprocessing version of the samples used in the analysis.

Run-range	Dataset
297046-299329	/DoubleMuon/Run2017B-31Mar2018-v1/MINIAOD /DoubleEG/Run2017B-31Mar2018-v1/MINIAOD /MuonEG/Run2017B-31Mar2018-v1/MINIAOD /SingleElectron/Run2017B-31Mar2018-v1/MINIAOD /SingleMuon/Run2017B-31Mar2018-v1/MINIAOD
299368-300676	/DoubleMuon/Run2017C-31Mar2018-v1/MINIAOD /DoubleEG/Run2017C-31Mar2018-v1/MINIAOD /MuonEG/Run2017C-31Mar2018-v1/MINIAOD /SingleElectron/Run2017C-31Mar2018-v1/MINIAOD /SingleMuon/Run2017C-31Mar2018-v1/MINIAOD
302030-303434	/DoubleMuon/Run2017D-31Mar2018-v1/MINIAOD /DoubleEG/Run2017D-31Mar2018-v1/MINIAOD /MuonEG/Run2017D-31Mar2018-v1/MINIAOD /SingleElectron/Run2017D-31Mar2018-v1/MINIAOD /SingleMuon/Run2017D-31Mar2018-v1/MINIAOD
303824-304797	/DoubleMuon/Run2017E-31Mar2018-v1/MINIAOD /DoubleEG/Run2017E-31Mar2018-v1/MINIAOD /MuonEG/Run2017E-31Mar2018-v1/MINIAOD /SingleElectron/Run2017E-31Mar2018-v1/MINIAOD /SingleMuon/Run2017E-31Mar2018-v1/MINIAOD
305040-306462	/DoubleMuon/Run2017F-31Mar2018-v1/MINIAOD /DoubleEG/Run2017F-31Mar2018-v1/MINIAOD /MuonEG/Run2017F-31Mar2018-v1/MINIAOD /SingleElectron/Run2017F-31Mar2018-v1/MINIAOD /SingleMuon/Run2017F-31Mar2018-v1/MINIAOD

Table 3.6: 2018 data samples used in the analysis, corresponding to an integrated luminosity of 59.7 fb^{-1}. The sample names correspond to the sample labels in the CMS database system and contain the information on the data taking conditions and on the reprocessing version of the samples used in the analysis.

Run-range	Dataset
315252-316995	/DoubleMuon/Run2018A-17Sep2018-v2/MINIAOD /MuonEG/Run2018A-17Sep2018-v1/MINIAOD /SingleMuon/Run2018A-17Sep2018-v2/MINIAOD /EGamma/Run2018A-17Sep2018-v2/MINIAOD
317080-319310	/DoubleMuon/Run2018B-17Sep2018-v1/MINIAOD /MuonEG/Run2018B-17Sep2018-v1/MINIAOD /SingleMuon/Run2018B-17Sep2018-v1/MINIAOD /EGamma/Run2018B-17Sep2018-v1/MINIAOD
319337-320065	/DoubleMuon/Run2018C-17Sep2018-v1/MINIAOD /MuonEG/Run2018C-17Sep2018-v1/MINIAOD /SingleMuon/Run2018C-17Sep2018-v1/MINIAOD /EGamma/Run2018C-17Sep2018-v1/MINIAOD
320673-325175	/DoubleMuon/Run2018D-PromptReco-v2/MINIAOD /MuonEG/Run2018D-PromptReco-v2/MINIAOD /SingleMuon/Run2018D-PromptReco-v2/MINIAOD /EGamma/Run2018D-PromptReco-v2/MINIAOD

Table 3.7: HH signal samples used in the analysis for SM and BSM hypotheses. They are divided per year and reported together with the corresponding value of k_λ and the sample cross section. The SM samples have $k_\lambda = 1$. The names of the samples reported represent the sample labels in the CMS database system.

k_λ	σ	HH MC sample
2016 samples		
1	31.05 fb	/SM-HH-NLO_POWHEG_GEN-SIM/ilmargje-MiniAOD-53f8667ba4b240d5eafd36e71bf34742/USER
2	13.81 fb	/HH_bb4l_2016_NLO_kLambda_2_GEN-SIM/ilmargje-MiniAOD-53f8667ba4b240d5eafd36e71bf34742/USER
5	94.82 fb	/HH_bb4l_2016_NLO_kLambda_5_GEN-SIM/ilmargje-MiniAOD-53f8667ba4b240d5eafd36e71bf34742/USER
2017 samples		
1	31.05 fb	/HH_bb4l_2017_NLO_152kPart2_gen-sim/ilmargje-MiniAOD-7c2f65f61e72ee224088fc41982d0d62/USER
2	13.81 fb	/HH_bb4l_2017_NLO_k_lambda_2_GEN-SIM/ilmargje-MiniAOD-320a10544d366c5c2cbf9f153fc62ac6/USER
5	94.82 fb	/HH_bb4l_2017_NLO_k_lambda_5_GEN-SIM/ilmargje-MiniAOD-320a10544d366c5c2cbf9f153fc62ac6/USER
2018 samples		
1	31.05 fb	/HH_bb4l_2018_NLO_152kPart2_gen-sim/ilmargje-processed_gen-sim-premix_DR_MiniAODstep3-0bd58594e6ade05f64e0c3a8301c3139/USER
2	13.81 fb	/HH_bb4l_2018_NLO_k_lambda_2_GEN-SIM/ilmargje-MiniAOD-0bd58594e6ade05f64e0c3a8301c3139/USER
5	94.82 fb	/HH_bb4l_2018_NLO_k_lambda_5_GEN-SIM/ilmargje-MiniAOD-0bd58594e6ade05f64e0c3a8301c3139/USER

the event selection, evaluate signal efficiency and acceptance, and estimate the expected signal and background contributions.

Signal samples

Signal samples for the SM gg $\rightarrow$ HH $\rightarrow 4\ell b\bar{b}$ process are generated at next-to-leading-order (NLO) in QCD using the POWHEG V2 [59, 60, 61] generator with the implementation described in [62, 63]. Using the same model, BSM signal samples are generated with alternative values of k_λ.
All samples are produced separately for each data taking year in order to take into account in the samples description the evolution of the CMS detector, the different trigger requirements, and the instantaneous luminosity conditions for the different years.
Signal samples used in the analysis for SM ($k_\lambda = 1$) and BSM hypotheses are reported in Table 3.7.

Background samples

The main background for this analysis is constituted by the single SM Higgs boson production processes. The description of H production is obtained with the POWHEG V2 generator for the six main production modes: gluon fusion (ggH), vector boson fusion (VBF) [64], and associated production (WH, ZH, $b\bar{b}$H, and $t\bar{t}$H [65]). For ggH, WH and ZH the MINLO extension of POWHEG is used [66, 67] to increase the accuracy in the two jet phase space. The description of the H boson decay to four leptons is obtained using the JHUGEN generator [68]. In the case of WH, ZH, $b\bar{b}$H, and $t\bar{t}$H, H boson decays H$\rightarrow$ ZZ $\rightarrow 2\ell$2X are allowed in order to take into account also events where two leptons originate from the decay

of associated Z, W bosons or top quarks. Showering of parton-level events is then performed by allowing QCD emissions at all energies in the shower and vetoing them afterwards according to the POWHEG internal scale.

Other background processes that contribute significantly to the analysis include genuine non resonant ZZ^* events.
Production of ZZ^* via quark-antiquark annihilation is generated at NLO using MadGraph5_aMCatNLO up to one extra parton, with appropriate settings to merge jet multiplicities. As this simulation covers a large range of ZZ invariant masses, dynamical QCD factorization and renormalization scales have been chosen. While the fully differential cross section has been computed at NNLO [69], this computation is not yet available in a partonic level event generator. NNLO/NLO k-factors are therefore applied to the Monte Carlo sample differentially as a function of $m(ZZ)$. Additional NLO electroweak corrections which depend on the initial state quark flavour and kinematics are also applied in the region $m(ZZ) > 2m(Z)$, where the corrections have been computed.
The $gg \to ZZ^*$ process is simulated at LO with MCFM 7.0 [70, 71]. In order to match the $gg \to H \to ZZ^*$ transverse momentum spectra predicted at NLO, the showering for MCFM samples is performed with different settings, allowing only emissions up to the parton-level scale. An exact calculation beyond the NLO does not exist for the $gg \to ZZ^*$ process, but it has been shown [72] that the soft collinear approximation is able to describe the background cross section and the interference term at NNLO. NNLO k-factors are then applied to the MC samples as a function of $m(ZZ^*)$ [73, 74, 75].
Further calculations showed that the k-factors are very similar at NLO for the $gg \to H \to ZZ$ and the $gg \to ZZ$ processes [76], and at NNLO for the $gg \to H \to ZZ$ process and the interference terms [77]. Therefore the same k-factor is used for the $gg \to H \to ZZ$ and the $gg \to ZZ$ processes [78]. The NNLO k-factor for the $gg \to H \to ZZ$ process is obtained as a function of $m_{4\ell}$ using the HNNLO v2 Monte Carlo program [73, 74, 75] by calculating the NNLO and LO $gg \to H \to 2\ell 2\ell'$ cross sections at the small H boson decay width of 4.07 MeV and taking their ratios.

Triboson production with at least one Z boson with leptonic decays, $t\bar{t}Z$ and $t\bar{t}W$ production, contribute to the backgrounds of this analysis and are generated at the NLO using MadGraph5_aMCatNLO, using similar settings as for the previous samples.

The PYTHIA 8 [79, 80] package is used for parton showering, hadronization and the underlying event simulation, both for signal and background samples, with parameters set by the CUETP8M1 tune [81] for the 2016 data taking period and the CP5 tune [82] for the 2017 and 2018 data taking periods. The NNPDF set of parton distribution functions (PDFs) [83] is used (NNPDF3.0 for the 2016, NNPDF3.1 for 2017 and 2018).

Table 3.8: Background Monte Carlo samples used in the analysis and correspondent cross sections. The names of the samples reported represent the sample labels in the CMS database system.

Process	Dataset Name	$\sigma \times BR(\times\epsilon_{\text{filter}})$
$gg \to H \to ZZ \to 4\ell$	/GluGluHToZZTo4L_M125_13TeV_powheg2_JHUgenV709_pythia8/[1]	12.18 fb
$qq \to Hqq \to ZZqq \to 4\ell qq$	/VBF_HToZZTo4L_M125_13TeV_powheg2_JHUgenV709_pythia8/[1]	1.044 fb
$q\bar{q} \to W^+H \to W^+ZZ \to 4\ell + X$	/WplusH_HToZZTo4L_M125_13TeV_powheg2-minlo-HWJ_JHUgenV709_pythia8/[1]	0.232 fb
$q\bar{q} \to W^-H \to W^-ZZ \to 4\ell + X$	/WminusH_HToZZTo4L_M125_13TeV_powheg2-minlo-HWJ_JHUgenV709_pythia8/[1]	0.147 fb
$q\bar{q} \to ZH \to ZZZ \to 4\ell + X$	/ZH_HToZZ_4LFilter_M125_13TeV_powheg2-minlo-HZJ_JHUgenV709_pythia8/[1]	0.668 fb
$gg \to ttH \to ttZZ \to 4\ell + X$	/ttH_HToZZ_4LFilter_M125_13TeV_powheg_JHUgenV709_pythia8/[1]	0.393 fb
$gg \to bbH \to bbZZ \to 4\ell + X$	/bbH_ToZZTo4L_M125_13TeV_JHUGenV7011_pythia8/[1]	0.135 fb
$qq \to ZZ \to 4\ell$	/ZZTo4L_13TeV_powheg_pythia8/[1]	1.256 pb
$gg \to ZZ \to 4e$	/GluGluToContinToZZTo4e_13TeV_MCFM701/[1]	0.00159 pb
$gg \to ZZ \to 4\mu$	/GluGluToContinToZZTo4mu_13TeV_MCFM701/[1]	0.00159 pb
$gg \to ZZ \to 4\tau$	/GluGluToContinToZZTo4tau_13TeV_MCFM701/[1]	0.00159 pb
$gg \to ZZ \to 2e2\mu$	/GluGluToContinToZZTo2e2mu_13TeV_MCFM701/[1]	0.00319 pb
$gg \to ZZ \to 2e2\tau$	/GluGluToContinToZZTo2e2tau_13TeV_MCFM701/[1]	0.00319 pb
$gg \to ZZ \to 2\mu 2\tau$	/GluGluToContinToZZTo2mu2tau_13TeV_MCFM701/[1]	0.00319 pb
WWZ	/WWZ_TuneCP5_13TeV-amcatnlo-pythia8/[1]	0.1651 pb
WZZ	/WZZ_TuneCP5_13TeV-amcatnlo-pythia8/[1]	0.05565 pb
ZZZ	/ZZZ_TuneCP5_13TeV-amcatnlo-pythia8/[1]	0.01398 pb
TTZ($\ell\ell$)	/TTZToLLNuNu_M-10_TuneCP5_13TeV-amcatnlo-pythia8/[1]	0.25271 pb
TTW($\ell\nu$)	/TTWJetsToLNu_TuneCP5_13TeV-amcatnloFXFX-madspin-pythia8/[1]	0.2149 pb

The label [1] in the datasets name stands for a string that is different for each data taking year i.e.:
RunIISummer16MiniAODv3-PUMoriond17_94X_mcRun2_asymptotic for 2016
RunIIFall17MiniAODv2-PU2017_12Apr2018_94X_mc2017_realistic_v14 for 2017
RunIIAutumn18MiniAOD-102X_upgrade2018_realistic_v15 for 2018

The detector response is simulated using a detailed description of the CMS detector implemented in the GEANT4 package [84, 85], both for signal and background samples. Simulated events are reconstructed using the same algorithms used for the data. Simulated samples include additional interactions in the same and neighbouring bunch crossings, referred to as pileup, and they are weighted to match the pileup distribution observed in data. This procedure is performed for each year separately.
Monte Carlo background samples used in the analysis are reported in Table 3.8.

3.3 Physics objects selection

After physics objects are reconstructed, as described in Section 2.2.7, they need to pass selection criteria in order to be used in the analysis. Physics objects selection is necessary in order to consider those coming from signal events and reject the ones deriving from backgrounds. The selection criteria applied to the specific object types are described in the following sections.

3.3.1 Electrons

Electrons are reconstructed by combining ECAL and tracker information as described in Section 2.2.7.

Electron candidates are preselected using loose cuts on track-cluster matching observables, in order to preserve the highest possible efficiency while rejecting part of the QCD background. In order to be considered for the analysis, electrons candidates are required to have a transverse momentum $p_T > 7$ GeV and a pseudorapidity $|\eta| < 2.5$. In order to suppress the selection of electrons from photon conversions whose tracks do not point to the main primary vertex of the event, electrons are also required to satisfy a loose primary vertex constraint:

$$|d_{xy}| < 0.5 \text{ cm} \qquad \text{and} \qquad |d_z| < 1 \text{ cm}, \tag{3.1}$$

where d_{xy} and d_z are the electron impact parameter with respect to the primary vertex in the transverse plane and in the longitudinal direction, respectively.
Electrons that pass all these requirements are called **loose electrons**.

Reconstructed electrons are identified and isolated using a Gradient Boosted Decision Tree (GBDT) multivariate classifier algorithm, which exploits observables sensitive to bremsstrahlung along the electron trajectory, the geometrical and energy-momentum compatibility between the electron track and the associated energy cluster in the ECAL, the shape of the electromagnetic shower, variables that discriminate against electrons originating from photon conversions, and the particle-flow (PF) lepton isolation [41]. The classifier was developed in the context of the $H \to ZZ^* \to 4\ell$ analysis [57] and trained separately for each data taking year on a Drell-Yan plus jets MC sample.

In order to ensure that the electrons are consistent with a common primary vertex (PV), they are required to have an associated track with a small impact parameter with respect to the event primary vertex. For this requirement the 3D impact parameter significance ($\text{SIP}_{3\text{D}}$) is defined as the ratio of the impact parameter of the lepton track in three dimensions ($\text{IP}_{3\text{D}}$) with respect to the chosen primary vertex position, and its uncertainty:

$$\text{SIP}_{3\text{D}} = \frac{\text{IP}_{3\text{D}}}{\sigma_{\text{IP}_{3\text{D}}}} \tag{3.2}$$

Electrons are required to satisfy $|\text{SIP}_{3\text{D}}| < 4$.
Loose electrons passing also identification, isolation and $\text{SIP}_{3\text{D}}$ requirements are defined **tight electrons**.

3.3.2 Muons

As described in Section 2.2.7, muons are reconstructed using information from the tracker detector and the muon system.
Muon candidates are preselected as either global muons or tracker muons. Standalone muon tracks that are only reconstructed in the muon system are rejected.

Table 3.9: The requirements for a muon to pass the Tracker High-p_T ID.

Requirement	Description
Muon station matching	Muon track in the tracker is matched to segments in at least two muon stations
Good p_T measurement	$\frac{p_T}{\sigma_{p_T}} < 0.3$
Vertex compatibility $(x-y)$	$\lvert d_{xy}\rvert < 2$ mm
Vertex compatibility (z)	$\lvert d_z\rvert < 5$ mm
Pixel hits	At least one pixel hit
Tracker hits	Hits in at least six tracker layers

In order to be considered in the analysis, muons are required to have transverse momentum $p_T > 5$ GeV and pseudorapidity $|\eta| < 2.4$. Also for muons, like for electrons, a loose primary vertex constraint is required in order to suppress the selection of non-prompt muons coming from in-flight decays of hadrons and cosmic rays:

$$|d_{xy}| < 0.5 \text{ cm} \qquad \text{and} \qquad |d_z| < 1 \text{ cm}, \tag{3.3}$$

where d_{xy} and d_z are the muon impact parameter with respect to the primary vertex in the transverse plane and in the longitudinal direction, respectively.
Muons that pass all these requirements are called **loose muons**.

Loose muons with $p_T < 200$ GeV are *identified* if they pass the PF muon identification [41]. Loose muons with $p_T > 200$ GeV are *identified* if they pass the PF identification [41] or the Tracker High $- p_T$ identification, the definition of which is reported in Table 3.9.
An additional *ghost cleaning* step is performed in order to treat situations where a single muon can be incorrectly reconstructed as two or more candidates:

- Tracker Muons that are not Global Muons are required to be matched to reconstructed segments in at least two stations of the muon system;
- if two muons are sharing 50% or more of their segments then the muon with lower quality is removed.

A particle-flow based isolation criterion is used in order to suppress the contamination from the hadron jets. The relative isolation for muons is defined as:

$$\text{RelPFIso} = \frac{\sum^{\text{charged}}_{\text{hadrons}} p_{\text{T}} + \max(\sum^{\text{neutral}}_{\text{hadrons}} p_{\text{T}} + \sum^{\text{photon}} p_{\text{T}} - \Delta\beta, 0)}{p^{\text{muon}}_{\text{T}}} \tag{3.4}$$

where the sums run over the charged, neutral hadrons and photons, in a cone defined by $\Delta R = \sqrt{(\Delta\eta)^2 + (\Delta\phi)^2} = 0.3$ around the lepton trajectory. To minimize the contribution of charged particles from pileup to the isolation computation,

charged hadrons are included only if they originate from the primary vertex. The correction factor $\Delta\beta = \frac{1}{2}\sum_{\text{PU}}^{\text{charged hadrons}} p_{\text{T}}$ corresponds to the estimate of the energy deposit of neutral particles (hadrons and photons) originated from pileup vertices. Muons with RelPFIso < 0.35 are considered isolated.

As for electrons, also for muons a condition on the 3D impact parameter significance is required in order to ensure muons to be consistent with a common primary vertex. Muons are required to satisfy the condition $|\text{SIP}_{\text{3D}}| < 4$.
Loose muons passing also identification, isolation and SIP_{3D} requirements are defined **tight muons**.

3.3.3 Lepton momentum calibration

The determination of the electron momentum relies on a combination from ECAL and tracker, while for muons it involves the tracker and the muon chambers. The calibration of the tracker, the ECAL and the muon system relies on the best knowledge of the detector conditions, but some small discrepancies can remain between data and simulation. Therefore the scale and the resolution of lepton momenta have to be calibrated. This is done in bins of p_{T}^{ℓ} and η^{ℓ}, exploiting some well-known di-lepton resonances.

The scale of electrons is calibrated using a $\text{Z} \to e^+e^-$ control sample, correcting the momenta as to align the reconstructed di-electron mass spectrum in the data to that in the MC, and to minimize the width of the distribution. Time-dependent variation of electron momenta may also happen, due to loss of the transparency of ECAL crystals. In order to account this variations, the correction is derived as a function of time. In addition, a smearing of the electron energies is applied in simulation so as to make the $\text{Z} \to e^+e^-$ mass resolution in simulation match the one observed in data.

The scale of muons, instead, is calibrated using a Kalman filter approach developed in the context of the W-like measurement of the Z boson mass [86], using the J/ψ meson and the Z boson decays into muons. This technique corrects the muon track in the silicon tracker for three different effects: accuracy of the knowledge of the magnetic field, residual misalignment, and the imperfect modelling of the amount of material traversed by muons. Then, as for electrons, the muon momentum resolution in simulation is smeared to match the one observed in data.

3.3.4 Lepton efficiency measurements

The efficiency of reconstructing and selecting signal leptons is an important point of the analysis. It needs to be optimized with respect to background leptons and to be accurately measured both in data and MC in order to correct possible

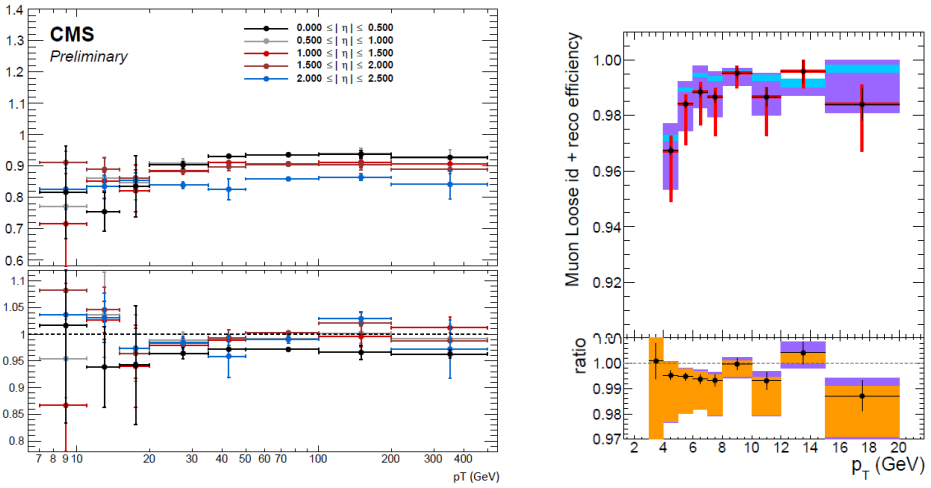

Figure 3.1: (left) Electron selection efficiencies vs p_{T} measured using the Tag-and-Probe technique, together with the corresponding data/MC ratio, for 2016 samples. (right) Muon reconstruction and identification efficiencies vs p_{T} measured with the Tag-and-Probe technique, together with the corresponding data/MC ratio, for 2016 samples. This plot is obtained for low p_{T} muons in the barrel region of the detector, both in upper and lower pads the violet rectangles include both statistic and systematic uncertainties [57].

discrepancies. Lepton efficiency measurements are based on the Tag-and-Probe technique [58], and the measurement is done in several bins of p_{T}^{ℓ} and η^{ℓ}.
As an example, Figure 3.1 reports the efficiency measured in data and simulations for electrons (left) and muons (right) in 2016 samples.
The efficiency measurement is done in data and MC simulations with the same method, in order to avoid any bias. Therefore it is possible to define a per-lepton efficiency scale factor as:

$$\mathrm{SF}_{\ell}(p_{\mathrm{T}}^{\ell}, \eta^{\ell}) = \frac{\epsilon_{\mathrm{data}}(p_{\mathrm{T}}^{\ell}, \eta^{\ell})}{\epsilon_{\mathrm{MC}}(p_{\mathrm{T}}^{\ell}, \eta^{\ell})} \tag{3.5}$$

Then, considering that for each event four leptons are selected, a per-event data/MC scale factor is defined as the product of the scale factor of the selected leptons:

$$\mathrm{SF}_{4\ell} = \prod_{\ell=1}^{4} \mathrm{SF}_{\ell}(p_{\mathrm{T}}^{\ell}, \eta^{\ell}) \tag{3.6}$$

which is used to re-weight MC samples event by event in order to match reconstruction efficiency in simulation to that of data.

3.3.5 Photons for FSR recovery

Leptons from Z bosons decays can radiate a high-energy photon due to *final state radiation* (FSR). This can cause accuracy loss in the information extracted from the four leptons selected in the analysis. In order to fully reconstruct the Higgs boson decay system, it is important to identify and collect the FSR photons, associating them to their parent leptons. The FSR recovery algorithms is designed to discriminate FSR photons from the background, due to pileup interactions or initial state radiation. This is done exploiting the particular kinematics of FSR photons, that are irradiated in a direction collinear to the one of their parent lepton, and tend to be isolated from other particles.

The selection of FSR photons is performed per-lepton, starting from the collection of PF photons provided by the particle-flow algorithm.
FSR photons candidates are considered if they satisfy the requirements of pseudo-rapidity $|\eta| < 2.4$, transverse momentum $p_{\mathrm{T}} > 2\mathrm{GeV}$ and isolation $\mathcal{I}^{\gamma} < 1.8$. The relative isolation $\mathcal{I}^{\gamma}$ for photon candidates is computed as:

$$\mathcal{I}^{\gamma} \equiv \frac{1}{p_{\mathrm{T}}^{\gamma}} \left(\sum p_{\mathrm{T}}^{\gamma} + \sum p_{\mathrm{T}}^{\mathrm{neutral}} + \sum p_{\mathrm{T}}^{\mathrm{charged}} \right) \tag{3.7}$$

where the $\sum p_{\mathrm{T}}^{\gamma}$, $\sum p_{\mathrm{T}}^{\mathrm{neutral}}$ and $\sum p_{\mathrm{T}}^{\mathrm{charged}}$ are the scalar sums of the transverse momenta of photons, neutral and charged hadrons contained inside a cone of radius $\mathrm{R} = 0.3$. The contribution from pileup is included in the sums.
Then selected photons are associated to the closest lepton in the event among all those that pass both the loose ID and SIP cuts. Photons that do not satisfy the cut $\Delta\mathrm{R}(\gamma, \ell)/(E_{\mathrm{T}}^{\gamma})^2 < 0.012$ and $\Delta\mathrm{R}(\gamma, \ell) < 0.5$ are discarded. This is required to consider only FSR photons, avoiding the selection of independent photons that can be present in the event. If more than one FSR photon is associated to the same lepton, only the one with the lowest $\Delta\mathrm{R}(\gamma, \ell)/(E_{\mathrm{T}}^{\gamma})^2$ is selected.
Since the FSR photons are often located in the isolation cone of their lepton, they tend to make it fail the isolation requirement. Therefore, all selected FSR photons are explicitly subtracted from the isolation sums of all loose leptons in the event, not only of their associated leptons.
More details on the optimization of the FSR photon selection can be found in Ref. [55].

3.3.6 Jets

As described in Section 2.2.7, jets are reconstructed by using the anti $-k_T$ clustering algorithm starting from particle-flow candidates, with a distance parameter $R > 0.4$, after rejecting the charged hadrons that are associated to pileup primary vertices.

In order to ensure a good reconstruction efficiency and to reduce the instrumental background as well as the contamination from pileup, tight identification criteria based on the multiplicities and energy fractions carried by charged and neutral hadrons are imposed on jets [87]. To be considered in the analysis, jets are required to have transverse momentum $p_T > 20$ GeV and pseudorapidity $|\eta| < 2.4$, in order to reject events coming from the vector boson fusion production of single Higgs bosons. Jets are also required to be separated from identified leptons by a distance $\Delta R(jet, \ell) > 0.3$, in order to avoid lepton-jet contamination [88].

Jet energy corrections are applied to account for the effects of pileup, uniformity of the detector response, and residual differences between the jet energy scale in the data and in the simulation. The jet energy scale calibration [89, 90, 91] relies on corrections parameterized in terms of the jet p_T and η.

For the 2016 and 2017 data taking years, the ECAL gradual timing shift was not propagated to the L1 trigger primitives properly and this resulted in an incorrect association of a large fraction of high-η trigger primitives to the previous bunch crossing. Since the L1 trigger is protected against firing over two consecutive bunch crossings, this resulted in events that self vetoed if a large deposit of ECAL energy was found in the pseudorapidity region $2 < |\eta| < 3$. Since these large energy deposits are left by jets with a large electromagnetic component, and since this effect is not described in the MC simulation, *L1 pre-firing* event weights are computed to correct for this effect.These corrections are obtained considering the contributions of all the jets in the event and are applied to correct the MC simulations for the 2016 and 2017 years.

In order to select the $4\ell b\bar{b}$ final state, it is necessary to identify b quark jets. For this purpose, the *DeepCSV* algorithm is employed as b tagging algorithm. It combines impact parameter significance, secondary vertex and jet kinematics information to provide a final output discriminator whose score is computed with a Deep Neural Network technique.
Data to simulation b tagging scale factors are applied as a function of the jet p_T, η and flavour to correct possible discrepancies of b tagging efficiencies in data and MC. They are applied as event weights and they are computed following the formula:

$$SF_{weight} = \Pi_i^{N_{jets}} SF(D_i, p_{Ti}, \eta_i, h_{flavour}) \tag{3.8}$$

where D_i is the b tagging discriminant value and $h_{flavour}$ is the hadron flavour of the considered jet. The scale factors are applied and computed separately for all three years. As an example of the b tagging scale factors effect, Figure 3.2 reports the distribution of the b tagger discriminator of the jet with the highest b tagger score in the event before (in blue) and after (red) applying the b tagging scale factor event weights. The plot is obtained using the HH signal sample for 2018.

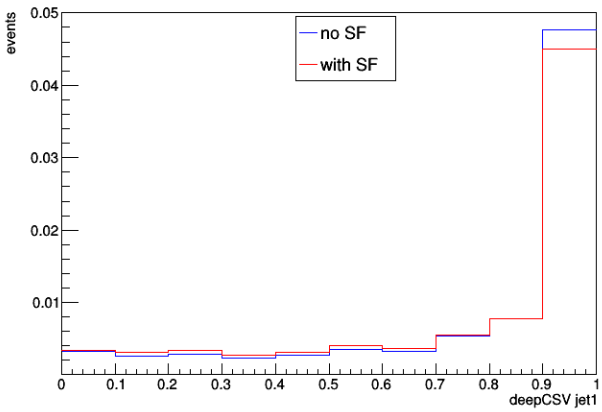

Figure 3.2: Distribution of the b tagger discriminator before (in blue) and after (red) applying the b tagging scale factor event weights. The distribution is obtained using the HH signal sample for 2018.

Chapter 4

Event selection and Analysis strategy

4.1 Event selection

The HH $\rightarrow 4\ell b\bar{b}$ process considered in this analysis is characterized by a clear signature of four isolated leptons and the presence of two b tagged jets. The process has a low cross section but with an appropriate event selection it is possible to achieve a good signal purity. The four lepton selection used in this analysis is similar to the one used in the H $\rightarrow$ ZZ* $\rightarrow 4\ell$ analysis [55, 56, 57].
The selection of events relies on the trigger selection, the selection of the Higgs boson to four lepton candidate and the selection of the Higgs boson to two b jets candidate.

4.1.1 Trigger selection

Events are required to have fired at least one path of the HLT menu described in Section 3.1. As discussed in the dedicated section, only inclusive lepton triggers are used in the analysis. No trigger requirements are set to exploit jets coming from the H $\rightarrow b\bar{b}$ decay. The set of inclusive lepton triggers used, in fact, grants already a very high total trigger efficiency, thus making the request of additional jet triggers not necessary for improving the trigger efficiency.

4.1.2 The H $\rightarrow 4\ell$ candidate selection

The analysis selection is designed to reconstruct a final state with 4ℓ ($4e$, 4μ, or $2e2\mu$) plus 2 jets, and the first step of this selection consists in the reconstruction of the Higgs boson decay to four leptons.

The four-lepton candidates are built from the selected leptons, which are the reconstructed leptons that pass the impact parameter, identification and FSR-corrected

isolation requirements described in Sections 3.3.1,3.3.2,3.3.5. A lepton cross cleaning is applied by discarding electrons which are within $\Delta R(e,\mu) < 0.05$ of selected muons, in order to avoid the muon track to be used to build an electron if an accidental match with an ECAL deposit happens. From this starting point, the selection of the four-lepton candidates proceeds according to the following steps.

Z candidates are defined as pairs of selected leptons of opposite charge and matching flavour (e^+e^-, $\mu^+\mu^-$) that satisfy $12 < m_{\ell\ell(\gamma)} < 120\,\mathrm{GeV}/c^2$, where the Z candidate mass includes the selected FSR photons if any.

ZZ candidates, which are the four leptons candidates, are built from pairs of non-overlapping Z candidates. The Z candidate with reconstructed mass $m_{\ell\ell}$ closest to the nominal Z boson mass is called Z_1, and the other one Z_2. The selected FSR photons are included in invariant mass computations. ZZ candidates are required to satisfy the following list of requirements:

- **Ghost removal:** there must be an angular distance $\Delta\mathrm{R}(\eta,\phi) > 0.02$ between each of the four leptons. This requirement protects from "ghost tracks" made by using a fraction of the hits left by a lepton in the tracker detector to make a second lepton candidate;
- **Lepton p_T:** two of the four selected leptons should pass $p_{\mathrm{T},1} > 20\,\mathrm{GeV}/c$ and $p_{\mathrm{T},2} > 10\,\mathrm{GeV}/c$, in order to assure a tighter selection than the simple trigger selection;
- **QCD suppression:** all four opposite-sign pairs that can be built with the four leptons (regardless of lepton flavour) must satisfy $m_{\ell\ell} > 4\,\mathrm{GeV}/c^2$. This cut suppresses pairs of leptons from cascade decays, which may be different-flavour and are found to broadly peak at very low invariant masses. In this case, selected FSR photons are not used in computing $m_{\ell\ell}$, since a QCD-induced low mass di-lepton (eg. J/ψ) may have photons nearby (eg. from a π_0).
- **Z_1 invariant mass:** $m_{\mathrm{Z}1} > 40\,\mathrm{GeV}/c^2$;
- **Wrong pairing suppression for same-flavour candidates ($4e$, 4μ):** defining Z_a and Z_b as the mass-sorted alternative pairing Z candidates (Z_a being the one closest to the nominal Z boson mass), the ZZ candidate is excluded if $m_{\mathrm{Z}_b} < 12\,\mathrm{GeV}/c^2$ while m_{Z_a} is closer to the nominal Z boson mass than m_{Z_1} is (i.e. $\mathrm{NOT}(|m_{\mathrm{Z}_a} - m_\mathrm{Z}| < |m_{\mathrm{Z}_1} - m_\mathrm{Z}|\ \mathrm{AND}\ m_{\mathrm{Z}_b} < 12\,\mathrm{GeV}/c^2)$). This cut discards 4μ and $4e$ candidates that are actually originated by an on-shell Z and a low-mass $\ell^+\ell^-$ resonance, which form an otherwise valid $\mathrm{Z}_1\mathrm{Z}_2$ combination with the alternative pairing of leptons.
- **Four-lepton invariant mass**: $m_{4l} > 70\ \mathrm{GeV/c^2}$

A single ZZ candidate per event is retained if more than one survives all kinematic cuts reported above. In this case, the one with the highest value of the scalar sum of the four-lepton p_T is chosen.
The signal efficiency within the geometrical acceptance after the $H \to 4\ell$ selection amounts to $\sim$ 50%, $\sim$ 34%, and $\sim$ 25% for the 4μ, $2e2\mu$, and $4e$ final states respectively.

4.1.3 The $H \to b\bar{b}$ candidate selection

After selecting the four-lepton candidate, the event selection proceeds by selecting the two additional jets coming from the $H \to b\bar{b}$ decay.

Events that contain less than 2 jets are discarded. The pairs of jet candidates (**bb candidates**) are built from the jets that pass all criteria described in section 3.3.6 with $|\eta| < 2.4$ in order to reduce the background coming from the vector boson fusion single-Higgs boson production mode.
The following possible cases can happen:

- If there are only two jets in the event, the bb candidate is formed with these two jets.
- If there are more than two jets in the event, the bb candidate is formed taking the two jets with the highest b tagger score in the event.

This criterion was chosen based on a study on the SM HH signal Monte Carlo samples in order to define the most efficient method to select the two signal jets. Three different methods were considered for selecting the signal jets if more than two jets survived in the event. The performances of the considered methods were verified by applying the bb candidate selection on reconstructed (RECO) jets in a MC signal sample, and counting how many times the selected jet were coming from the Higgs boson decay in two b jets, according to the generated (GEN) information of the MC.
A cone of radius $\Delta R = 0.4$ was built around each selected RECO jet and a GEN b jet from the decay of the Higgs boson was searched inside of it. The considered RECO jet was then checked for matching with the GEN b jet. For this study three different methods for selecting the two jets for building the di-jet candidate were considered:

- select the two highest p_T jets in the event;
- select the two highest b tagger score jets in the event;
- select the highest b tagger score jet and the highest p_T jet in the event, among the remaining ones.

Figure 4.1 reports the result of this study. The method that selects the two highest p_{T} jets in the event (blue line) is not very efficient: most of the times only one of the selected jets matches with a GEN jet from the Higgs boson decay. In a fraction of the cases, none of the selected jets matches. For the method that selects the highest b tagger score jet and the highest p_{T} jet in the event (green line), correct matching is more frequent, but also with this method there are some cases where none of the two selected jets match with a GEN jet coming from the Higgs boson. The method that selects two highest b tagger score jets in the event (red line), instead, is the most efficient since in most of the cases both selected jets match those coming from the Higgs boson decay.
The latter method was chosen (two highest b tagger jets) for selecting the two jets for building the di-jet candidate, since it was found to be the most efficient.
Figure 4.2 reports the invariant mass built from the two jets selected with the three methods. It is possible to notice that the invariant mass built from the RECO jets selected with the 2-highest-b-tagger-jets method (red line) has less events in the right tail of the distribution with respect to the other methods (green and blue lines), since with this method less backgound jets (i.e. jets not coming from the Higgs boson decay in two b jets) are selected.

In any case, the b tagger requirement is not used to further discard events. The complete distribution of the b tagging discriminant will be used as input of the multivariate analysis performed to discriminate signal and background events (Section 4.3).

4.1.4 Signal region

Events containing one selected ZZ candidate and one bb candidate and passing the further requirement of $115 < m_{4l} < 135$ GeV/c^2 form the **signal region**.

The overall signal acceptance after the full selection amounts to $\sim 36\%$, $\sim 26\%$, and $\sim 20\%$ for the bb4μ, bb2e2μ, and bb4e final states respectively, with the main source of acceptance loss being the geometrical acceptance of the detector, followed by the inefficiency on the selection requirements on the leptons p_{T}.

4.2 Background estimation

The background sources to the $4\ell\mathrm{b}\bar{\mathrm{b}}$ final state are various. Some of them are evaluated from the MC samples while others are estimated from data directly. In the following sections the estimation of the different contributions is presented.

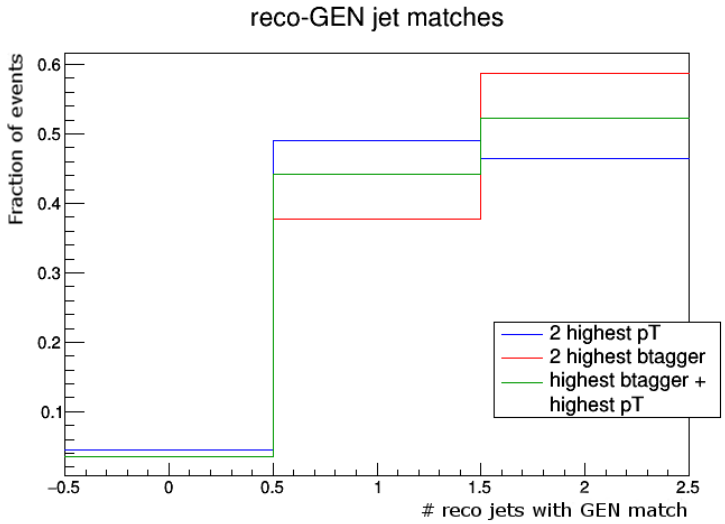

Figure 4.1: RECO-GEN jet matching study performed on the signal Monte Carlo sample. RECO jets selected with one of the three method considered are matched with GEN jets coming from the decay of the Higgs boson. For the method that selects the two highest p_T jets (blue line) most of the times only one of the RECO jet selected matches with a GEN jet; for the method that selects the highest b tagger score jet and the highest p_T jet (green line) most of the times both of the RECO jets selected matches with a GEN jet but there are cases where none of the two RECO jets selected match with a signal GEN jet; for the method that selects the two highest b tagger score jets in the event (red line) most of the times both the selected RECO jets are matched with GEN jets coming from the decay of the Higgs boson and less background jets are selected.

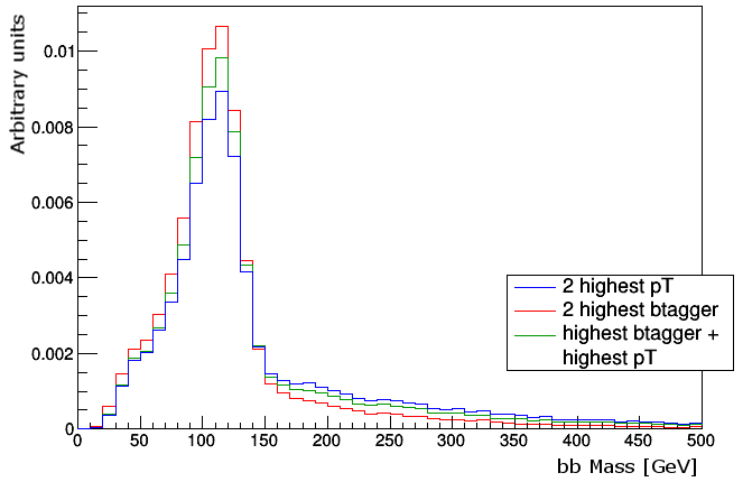

Figure 4.2: Di-jet invariant mass built from RECO jets selected with the three different methods considered: the two highest p_T jets (blue line), the highest b tagger score jet and the highest p_T jet (green line), the two highest b tagger score jets in the event (red line).

4.2.1 Single SM Higgs boson background

The single SM Higgs boson processes constitute the main background source for this analysis. They can present, in fact, a real Higgs boson decaying into four leptons, which is one of the fundamental requirement for selecting events in the analysis. The other condition necessary to select events is the presence of at least two jets passing the selection. This can happen if jets coming from the hadronization of initial state gluons or from the decay of particles produced in association with the Higgs boson pass the selection described in Section 3.3.6.
Among the different single Higgs boson production modes, the gluon fusion and the vector boson fusion mechanisms represent the main sources of background. The first one because of its large cross section, the second one because of the presence of two jets in the final state.
The description of these single SM Higgs boson processes is obtained using the POWHEG V2 generator, as described in Section 3.2.2, and the estimation of the contribution of these processes to the analysis is extracted from the MC simulations.

4.2.2 $q\bar{q} \to ZZ$ background

The ZZ^* production via quark-antiquark annihilation is another important background for the analysis. It can present, in fact, four leptons in the final state, with a non distinguishable signature with respect to the single SM Higgs boson production, while jets passing the selection described in Section 3.3.6 can arise from the hadronization of initial state gluons.
This background contribution is estimated from the MC simulation (Section 3.2.2). K-factors are applied to the Monte Carlo sample differentially as a function of $m(ZZ)$ to account for the different order between the MC simulation and the theoretical computation for the cross section of this process. Additional NLO electroweak corrections depending on the initial state quark flavour and kinematics are also applied in the region $m(ZZ) > 2m(Z)$, where they have been computed.

4.2.3 $gg \to ZZ$ background

The ZZ^* production via gluon fusion represents another important source of background for the analysis. Similarly to the $q\bar{q} \to ZZ$ background, the $gg \to ZZ$ process presents four leptons in the final state, with a non distinguishable signature with respect to the single SM Higgs boson production, and jets passing the selection (Section 3.3.6) can arise from the hadronization of initial state gluons.
This background is estimated from the MC simulation presented in Section 3.2.2. K-factors are applied to the MC samples as a function of $m(ZZ^*)$ to account for the different order between the MC simulations and theoretical calculations for this process.

4.2.4 VVV and TTV backgrounds

Other background sources for the analysis are represented by triboson production with at least one Z boson with leptonic decays, and by $t\bar{t}Z$ and $t\bar{t}W$ production. These processes, in fact, can present four leptons and two jets in the final state, passing the event selection. Leptons can derive from the leptonic decays of the W or Z bosons, or from the leptonic decay of the W boson deriving from the top quark decay, while jets can derive from hadronic decays of the same objects. In particular, b jets are produced in almost every decay of the top quark.
The contribution of these background processes is estimated from the MC simulation (Section 3.2.2).

4.2.5 Z+X background

We define as $Z + X$ the background arising from lepton candidates that do not correspond to prompt, real leptons. This background originates from processes that contain one or more non-prompt or mis-reconstructed leptons. The main

sources of non-prompt leptons are non-isolated electrons and muons coming from decays of heavy flavour mesons or electrons from γ conversions, while sources of mis-reconstructed leptons are jets (usually originating from light-flavour quarks) that are mistakenly reconstructed as leptons. In the following discussion we will consider a *fake lepton* any non-prompt or mis-reconstructed lepton, coming from the sources mentioned above.

To estimate the expected $Z + X$ background yield in the signal region, dedicated control regions are defined with requirements similar to the signal region but in such a way not to contain signal events and to be enriched with lepton candidates that pass the *loose* lepton selection criteria (defined in Section 3.3.1 and 3.3.2). The $Z+X$ background yield in the signal region is extrapolated from these regions on the basis of the probability for loose lepton candidates to pass also the final selection criteria (defined in Section 4.1.2). These probabilities, referred to as *fake rates*, are estimated independently from data as illustrated in the following section.

The control regions defined for the estimation of the Z+X background are obtained as subsets of Z + 2 jets event samples which pass the first step of the selection (First Z step, see Section 4.1.2), requiring an additional pair of loose leptons of same flavour and opposite charge, that pass the $\text{SIP}_{3\text{D}}$ cut. The events must satisfy all kinematic cuts applied for the Higgs phase space selection (see 4.1.2).
The first control sample is obtained by requiring that the two loose leptons which do not form the Z_1 candidate do not pass the final identification and isolation criteria. The other two leptons pass the final selection criteria by definition of the Z_1. The presence of two jets is also required. This sample is denoted as *2 Prompt + 2 Fail + 2 jets* ($2P + 2F$) sample. It is expected to be populated with events that intrinsically have only two prompt leptons (mostly DY, with a small fraction of $t\bar{t}$ and $Z\gamma$ events).
The second control sample is obtained by requiring one of the four leptons not to pass the final identification and isolation criteria, while the other three leptons should pass the final selection criteria. Also in this case, the presence of two jets is required. This control sample is denoted as *3 Prompt + 1 Fail + 2 jets* ($3P + 1F$) sample. It is expected to be populated with the type of events that populate the $2P + 2F$ region, but with different relative proportions, with also a contribution from WZ events that intrinsically have three prompt leptons.
The control samples obtained in this way, orthogonal by construction to the signal region, are enriched with fake leptons and are used to estimate the Z+X background in the signal region.

Fake rate determination

In order to evaluate the fake rates (defined as the probability for loose lepton candidates to pass also the tight selection criteria) and then estimate the Z+X

contribution in the signal region of the analysis, which is composed by event containing four leptons and at least two isolated jets, control samples are defined by selecting events containing two leptons coming from a Z boson, a loose lepton (electron or muon), and at least 2 jets isolated with respect to the leptons ($Z(\ell\ell)+e+at\ least\ 2\ isolated\ jets$ or $Z(\ell\ell)+\mu+at\ least\ 2\ isolated\ jets$). Events in these control regions are required to have two same flavour, opposite charge leptons with $p_T > 20$ GeV for the first lepton and $p_T > 10$ GeV for the second lepton, passing the tight selection criteria, thus forming the Z candidate. In addition, events are required to have exactly one lepton passing the loose selection criteria and at least two isolated jets. The loose lepton is used as probe lepton for the fake rate measurement. The invariant mass of this lepton and the opposite sign lepton from the reconstructed Z candidate should satisfy $m_{2\ell} > 4$ GeV. All these conditions are required to select a kinematic region matching as closely as possible the signal region.

The fake rates are evaluated using the tight requirement $|M_{\text{inv}}(\ell_1\ell_2)-M_{\text{Z}}| < 7$ GeV, to reduce the contribution from photon (asymmetric) conversions populating the low mass region. The fake rates are measured in bins of the loose lepton transverse momentum and are computed separately for the barrel and the endcap regions of the CMS detector. The estimates are obtained separately for electrons and muons, and for the different data taking years. The estimates for 2016, 2017, and 2018 data are shown in Figure 4.3 (dark green markers), Figure 4.4 (dark green markers), and Figure 4.5 (dark green markers), respectively.

In order to validate the procedure two other control regions are considered selecting events with similar characteristics of the region just defined above, but removing some of the requirements for event selection. One control region is built removing the requirement on the jets isolation, thus selecting events with two leptons coming from a Z boson, a fake lepton (electron or muon), and two jets not explicitly isolated (i.e. no requirements are set on the jets isolation) with respect to leptons ($Z(\ell\ell)+e+at\ least\ 2\ not\ isolated\ jets$ or $Z(\ell\ell)+\mu+at\ least\ 2\ not\ isolated\ jets$). The other control region is built selecting events containing two leptons coming from a Z boson and a fake lepton, electron or muon, ($Z(\ell\ell)+e$ or $Z(\ell\ell)+\mu$), removing requirements on the jet selection.
Fake rate curves are evaluated in these other regions and then compared with those obtained in the initial region ($Z(\ell\ell)+e+at\ least\ 2\ isolated\ jets$ and $Z(\ell\ell)+\mu+at\ least\ 2\ isolated\ jets$). Figure 4.3 reports the fake rate curves obtained in these three regions using the 2016 data. It is possible to notice that the curve with the blue markers (obtained in the $Z(\ell\ell)+e$ and $Z(\ell\ell)+\mu$ control regions) and the curve with red markers (obtained in the $Z(\ell\ell)+e+at\ least\ 2\ not\ isolated\ jets$ and $Z(\ell\ell)+\mu+at\ least\ 2\ not\ isolated\ jets$ regions) are very similar. This means that requiring two additional not isolated jets in the $Z(\ell\ell)+e$ and $Z(\ell\ell)+\mu$ control regions does not modify the phase space in which the loose lepton is selected, and

thus the probability of mis-reconstructing some other objects as leptons is similar, as a function of p_T. Adding the requirement of having two isolated jets (dark green markers), the loose lepton is forced to be far away from jets, excluding all the events where the objects that can be mis-reconstructed as leptons come from the surroundings of the jets. This results in a lower fake rate probability especially at low p_T, where most of the b jets can be mis-reconstructed as leptons.
Since in this analysis events are required to have at least 2 isolated jets, the fake rate is estimated in the $Z(\ell\ell) + \ell + at\ least\ 2\ isolated\ jets$ region.

In Figure 4.4 and Figure 4.5 the fake rate distributions for the 2017 and 2018 datasets are shown, respectively. Dark green markers represent the fake rates computed in the $Z(\ell\ell) + \ell + at\ least\ 2\ isolated\ jets$ control region, used in the analysis, while the fake rates obtained in the control region $Z(\ell\ell) + \ell$ used for validation are shown with blue markers.

Fake rate application

Once the fake rates are estimated they are applied to the $2P + 2F$ and $3P + 1F$ dedicated control regions to estimate the $Z + X$ background yield in the signal region.
The expected number of $Z + X$ background events in the $3P + 1F$ region, N^{bkg}_{3P1F}, can be computed from the number of events observed in the $2P + 2F$ control region, N_{2P2F}, by weighting each event in the region with the factor $(\frac{f_i}{1-f_i} + \frac{f_j}{1-f_j})$, where f_i and f_j correspond to the fake rates of the two loose leptons:

$$N^{bkg}_{\mathrm{3P1F}} = \Sigma(\frac{f_i}{1-f_i} + \frac{f_j}{1-f_j})N_{\mathrm{2P2F}} \tag{4.1}$$

The expected reducible background in the signal region is given by the sum of two terms:

- a *2P2F component*, obtained from the number of events observed in the $2P + 2F$ control region, N_{2P2F}, by weighting each event in that region with the factor $(\frac{f_i}{1-f_i} + \frac{f_j}{1-f_j})$, where f_i and f_j correspond to the fake rates of the two loose leptons

- a *3P1F component*, obtained from the difference between the number of observed events in the $3P + 1F$ control region, N_{3P1F}, and the expected contribution from the $2P + 2F$ region and ZZ processes in the signal region, $N^{\mathrm{ZZ}}_{\mathrm{3P1F}} + N^{\mathrm{bkg}}_{\mathrm{3P1F}}$. The $N^{\mathrm{bkg}}_{\mathrm{3P1F}}$ is given by the equation 4.1 and the $N^{\mathrm{ZZ}}_{\mathrm{3P1F}}$ is the contribution from ZZ which is taken from the simulation. The difference $N_{\mathrm{3P1F}} - N^{\mathrm{bkg}}_{\mathrm{3P1F}} - N^{\mathrm{ZZ}}_{\mathrm{3P1F}}$, which may be negative, is obtained for each (p_T, η) bin for the F lepton, and is weighted by $\frac{f_i}{1-f_i}$, where f_i denotes the fake rate of this lepton. This *3P1F component* accounts for the contribution of

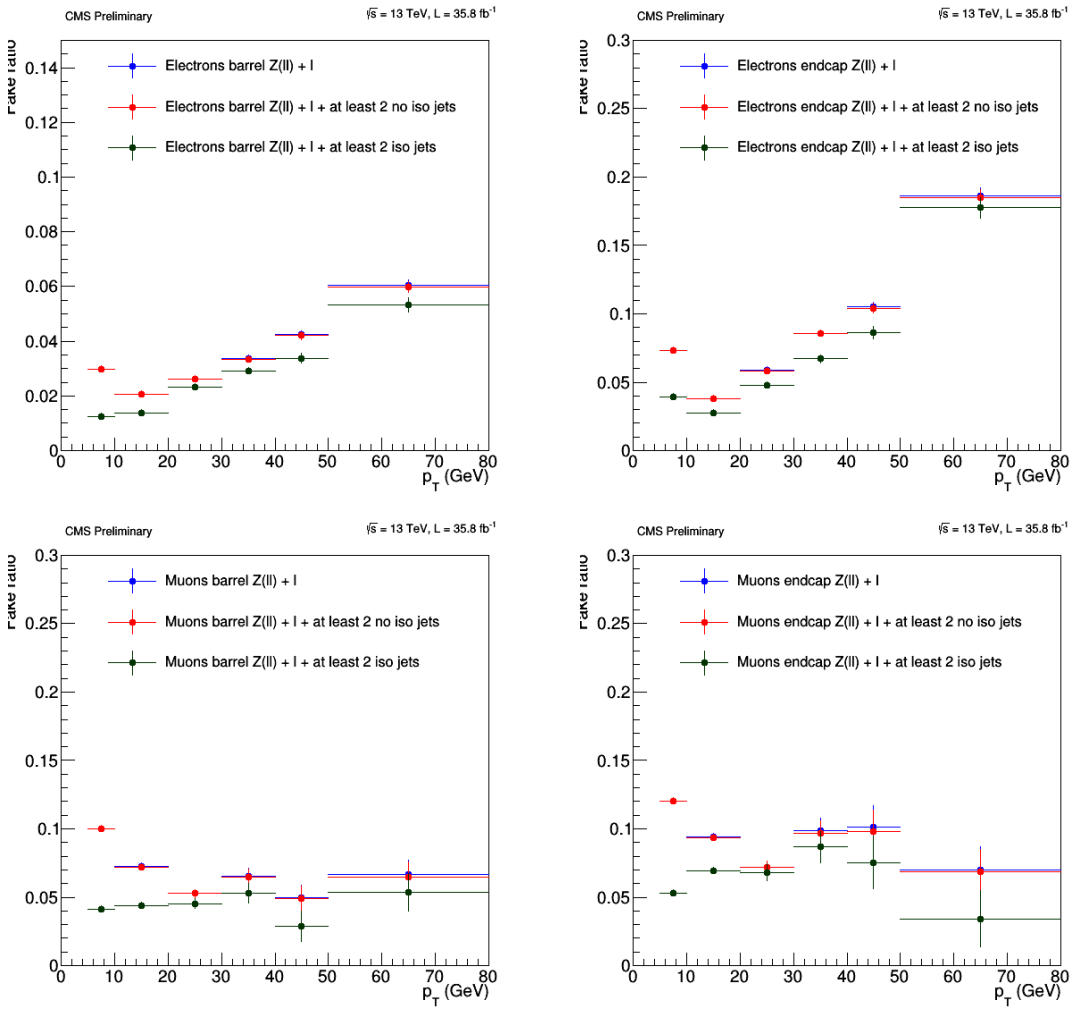

Figure 4.3: Fake rate as a function of the loose lepton probe p_T for electrons and muons obtained with 2016 datasets. Dark green markers represent the curves obtained in the $Z(\ell\ell) + \ell + at\ least\ 2\ isolated\ jets$ control regions, used in the analysis. The fake rate curves obtained in the two control regions used for validation are shown with red markers ($Z(\ell\ell) + \ell + at\ least\ 2\ not\ isolated\ jets$) and blue markers ($Z(\ell\ell) + \ell$). The fake rates are shown after the removal of WZ contribution from MC.

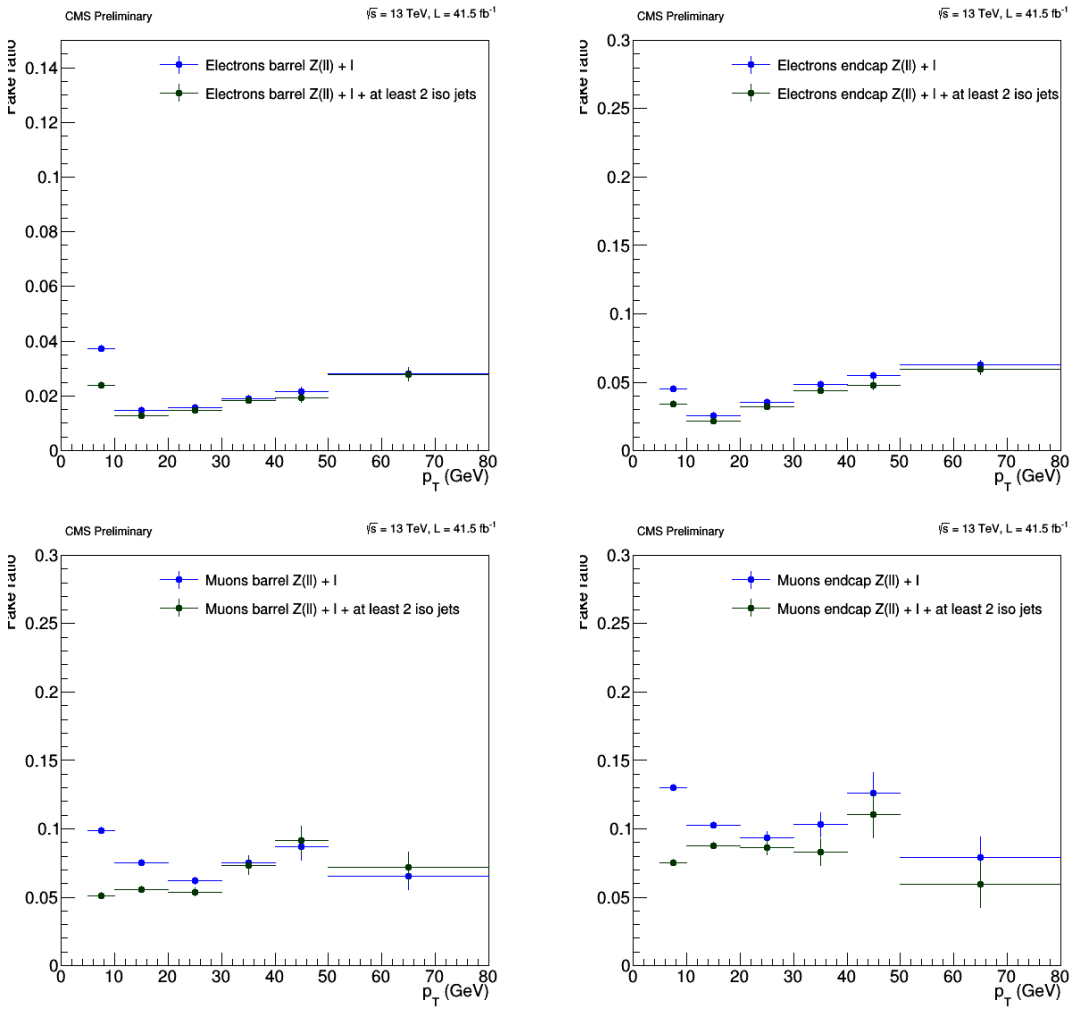

Figure 4.4: Fake rate as a function of the loose lepton probe p_T for electrons and muons obtained with 2017 datasets. Dark green markers represent the fake rate curve obtained in the $Z(\ell\ell) + \ell + at\ least\ 2\ isolated\ jets$ control region, used in the analysis. The fake rate curves obtained in the control region $Z(\ell\ell) + \ell$ used for validation are shown with blue markers. The fake rates are shown after the removal of WZ contribution from MC.

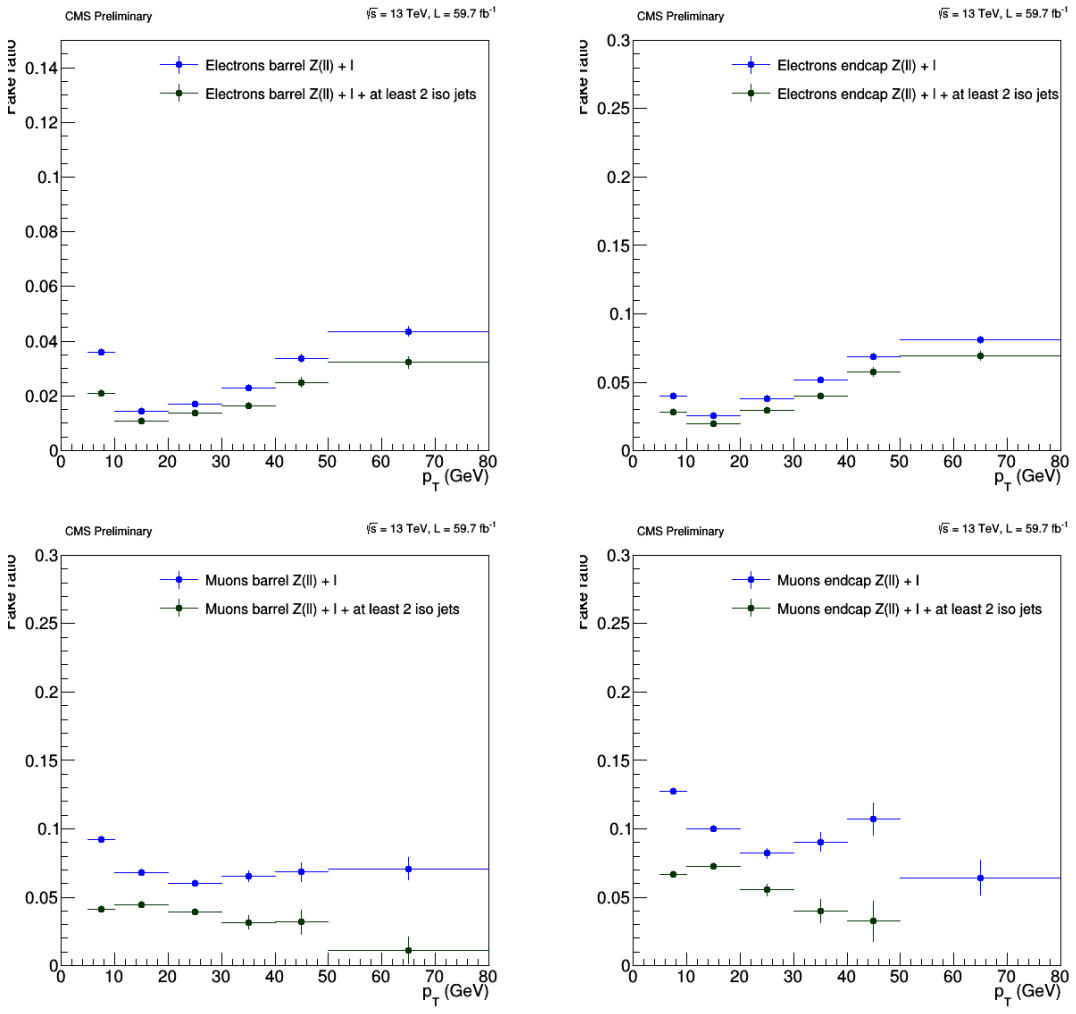

Figure 4.5: Fake rate as a function of the loose lepton probe p_T for electrons and muons obtained with 2018 datasets. Dark green markers represent the fake rate curve obtained in the $Z(\ell\ell) + \ell + at\ least\ 2\ isolated\ jets$ control region, used in the analysis. The fake rate curves obtained in the control region $Z(\ell\ell) + \ell$ used for validation are shown with blue markers. The fake rates are shown after the removal of WZ contribution from MC.

Table 4.1: $Z + X$ background yields for the three leptonic final states and for the three data taking years.

year	4e	4μ	$2e2\mu$
2016	1.40 ± 0.67 (stat+syst)	0.79 ± 0.28 (stat+syst)	2.64 ± 1.10 (stat+syst)
2017	0.52 ± 0.22 (stat+syst)	1.48 ± 0.48 (stat+syst)	2.00 ± 0.72 (stat+syst)
2018	0.72 ± 0.28 (stat+syst)	1.60 ± 0.50 (stat+syst)	2.58 ± 0.89 (stat+syst)

reducible background processes with only one fake lepton (like WZ events), and for the contribution of other processes (e.g. photon conversions) that are not properly estimated by the *2P2F component*, because of the fake rates used, which is estimated in a region of different composition from the one in which is applied.

The full expression for the prediction of the reducible background in the signal region can be written as:

$$N_{\mathrm{SR}}^{\mathrm{bkg}} = \Sigma \frac{f_i}{(1-f_i)}(N_{\mathrm{3P1F}} - N_{\mathrm{3P1F}}^{\mathrm{bkg}} - N_{\mathrm{3P1F}}^{\mathrm{ZZ}}) + \Sigma \frac{f_i}{(1-f_i)} \frac{f_j}{(1-f_j)} N_{\mathrm{2P2F}} \qquad (4.2)$$

The Z+X event yields in the signal region is obtained after applying the additional cuts of the selection; yields obtained for the three data taking years and for the three leptonic final states are reported in Table 4.1.

Uncertainties on Z+X background estimation

The uncertainty on the $Z + X$ background estimation arises from the difference in composition of the $Z + X$ background processes in the region where the fake rate is measured and where it is applied. This uncertainty can be estimated by measuring the fake rates for individual background processes in the Z + 1ℓ region in simulation. The weighted average of these individual fake rates is the fake rate that is measured in this sample (in simulation). The exact composition of the background processes in the 2P+2F region where the fake rates are applied can be determined from simulation, and one can reweigh the individual fake rates according to the 2P+2F composition. The difference between the reweighed fake rate and the average one can be used as a measure of the uncertainty on the measurement of the fake rates.
The uncertainties are estimated separately per 4-lepton final states and are reported in the Table 4.2.

Table 4.2: Systematic uncertainties on the $Z + X$ background estimate for the 3 years.

year	4μ	4e	$2e2\mu$
2016	30%	41%	35%
2017	30%	38%	33%
2018	30%	37%	33%

4.3 Multivariate methods for background rejection

In order to better discriminate between signal and background events and to improve the analysis sensitivity, a Boosted Decision Tree (BDT) is trained exploiting different kinematic variables.
In this paragraph a quick introduction to the BDT concept is presented, and then the implementation used in the analysis is reported.

4.3.1 The Boosted decision tree concept

Decision Trees are supervised Machine Learning algorithms that can perform both classification and regression tasks. In the analysis presented here, this algorithm is used for classification purposes, i.e. classifying data events in signal or background "categories", allowing a better separation between signal and background events to be achieved.

Decision trees can be represented as a binary tree structure, like in Figure 4.6. Following the scheme, starting from the initial root node, a sequence of binary divisions is applied to the data, using the discriminating variables x_i. Each split uses the variable that at the considered node gives the best separation between signal and background when being cut on. The same variable may thus be used in several nodes, while others might not be used at all. The phase space is thus divided into many regions that are eventually classified as signal or background, depending on the majority of training events that end up in the final leaf node. The training of a decision tree is the process that defines the splitting criteria for each node.

Boosting of a decision tree is a way of improving the performance of the algorithm. There are various boosting methods, but the general idea is to combine several weak MVA algorithms (like decision trees) into a stronger one. The combination is performed training MVA algorithms sequentially, each trying to correct its predecessor.
Boosting stabilizes the response of the decision trees with respect to statistical fluctuations in the sample used for training, and enhances considerably the performance with respect to a single decision tree. The trees used are derived from the same training sample by reweighting events, and are combined into a single

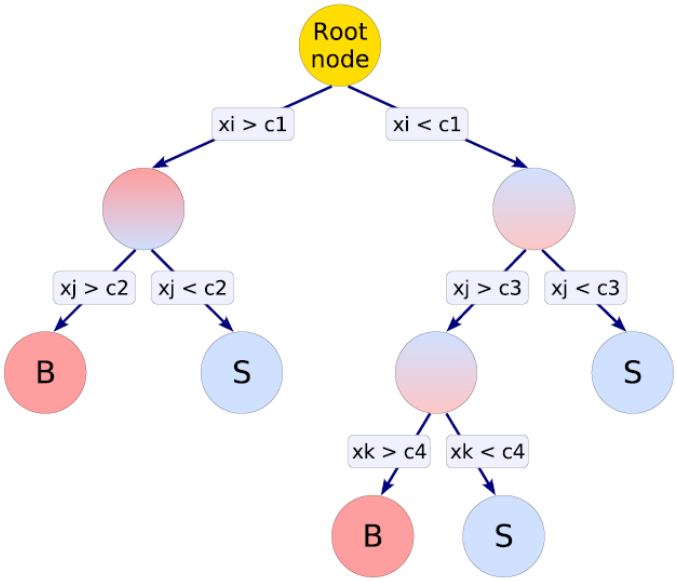

Figure 4.6: Schematic view of a decision tree. Starting from the root node, a sequence of binary splits using the discriminating variables x_i is applied to the data. Each split uses the variable that at the considered node gives the best separation between signal and background when being cut on. The same variable may thus be used at several nodes, while others might not be used at all. The leaf nodes at the bottom of the tree are labelled S (signal) or B (background), depending on the majority of events that finish in the respective nodes [92].

classifier which is a weighted response of each individual tree. Decision trees need to be boosted a few hundred times to effectively stabilise the BDT response and achieve optimal performance.

In what follows a combination of boosting and *bagging* (contraption of *bootstrap aggregating*) is used. Bagging is a technique used to combine several trees into one algorithm (forming a forest), to improve stability to small changes in the training samples. The resulting machine learning model is therefore formed by more than one decision tree and overall boosted using the gradient boosting method.

Further details on this topic can be found in Ref. [92].

4.3.2 BDT configuration

The analysis relies on a BDT to improve the signal vs background separation.
The algorithm is trained in the signal region, defined in Section 4.1.4, i.e. on events containing one $H \to 4\ell$ candidate (Section 4.1.2) and one $H \to b\bar{b}$ candidate (Section 4.1.3), and passing the further mass requirement $115 < m_{4l} < 135$ GeV/c^2.
The BDT training is performed on MC samples. The signal is trained against all the backgrounds that survive in the signal region after the event selection: ggH, VBF, WH, ZH, ttH, bbH, ttZ, ttW, ZZ (qqZZ and ggZZ), i.e. the processes described by the MC samples in Table 3.8.
The MC samples considered are divided into training and testing subsets, maintaining the proportions in the processes composition inside the samples. The algorithm is then trained on the former while the latter is used to test the generalisation capabilities and predictions.
The training is performed separately for each data taking year and for each of the three different four-lepton final states ($b\bar{b}4\mu$, $b\bar{b}4e$, and $b\bar{b}2e2\mu$), in order to improve the analysis sensitivity with a better description of the subsample considered. Such subsamples can present in fact differences due to the evolution and updates of the CMS detector across the data taking years. The distributions obtained from the BDT response for all cases are then used as input for the statistical analysis performed in the following to extract the results (Chapter 5).

BDT configuration tests

The BDT training takes as input different kinematic variables present in the final state containing four leptons and (at least) two jets. In order to find the best and most efficient BDT settings for background rejection, various tests were performed using different sets of variables as input of the algorithm. The kinematic variables considered are the p_T, η, and ϕ of the four leptons in the final state, the p_T, η, ϕ, and b tag score of the two selected jets in the final state (see Section 4.1.3), the missing transverse energy in the event (E_{T}^{miss}), the angular distances ΔR and $\Delta\phi$

between the momenta of the two reconstructed Higgs bosons, and the invariant mass m_{jj} built from the two selected jets.
All the tests were performed on 2016 MC samples, in the $b\bar{b}4\mu$ final state. The chosen set of variables was then checked to perform well also in the other two final states and for 2017 and 2018 samples.
For each set of variables considered, the BDT is trained and the Receiver Operating Characteristic (ROC) curve is computed. The ROC curve is a diagram used to display the performance of a classification algorithm. As an example, Figure 4.7 represents the ROC curve obtained for the training and testing for 2016 samples using the final set of input variables of the BDT. The x axis reports the efficiency in signal selection while the y axis indicates the efficiency in background rejection. Better performance of the algorithm corresponds to a larger area under the ROC curve (AUC).[1] The area under the ROC curve is used as a figure of merit for choosing the final configuration.
The different sets of variables tested are reported in Table 4.3 together with the area under the ROC curve obtained on the test samples. Although inclusion of missing energy led to well-performing classifiers according to MC, the degree of data-MC agreement for this variable was considered unsatisfactory, and would have required data/MC correction factors that were not available at the time of writing. Classifiers using this variable were therefore discarded.
The set of kinematic variables chosen as inputs for the BDT for performing the analysis is the one reported in the Table 4.3 for the configuration number 11, i.e. including the p_T of the four leptons in the final state, the p_T and the b tag score of the two selected jets, the ΔR between the momenta of the two reconstructed Higgs bosons and the invariant mass of the di-jet system.
All the tests were performed checking the ROC curve for algorithm over-training. Over-training occurs when the algorithm is learning specific features of the training sample and it is not retaining enough generalization capabilities. An indication that the algorithm is not over-training is given by the ROC plot if the curves obtained for training and testing samples are superimposed.

Summarizing, the BDT training was based on the following input variables:

- the p_T of the four leptons selected in the final state;
- the p_T and the b tag score of the two selected jets in the final state (i.e. the two jets with the highest b tag score in the event, see Section 4.1.3);
- the angular distance ΔR between the two reconstructed Higgs bosons;
- the di-jet invariant mass, built from the two selected jets.

[1] As performance comparison, a classifier based on a totally random choice has an area under the ROC curve of 0.5, represented by a straight line going from top left to bottom right of the plot.

Table 4.3: Sets of variables tested as inputs of the BDT algorithm, together with the area under the ROC curve (AUC) obtained for each set, used as performance metric. The tests were performed on 2016 MC samples, in the $b\bar{b}4\mu$ final state.

Config.	leptons p_T	leptons η	leptons ϕ	jets p_T	jets η	jets ϕ	jets b tag	ΔR_{HH}	E_T^{miss}	$\Delta\phi_{\mathrm{HH}}$	m_{jj}	AUC
1	x						x	x		x		0.894
2	x						x	x	x	x		0.901
3	x						x	x	x			0.901
4	x			x			x	x	x			0.904
5	x			x	x	x	x	x	x			0.905
6	x			x	x		x	x	x			0.904
7	x	x			x		x	x	x			0.901
8	x	x		x	x		x	x	x		x	0.917
9	x			x	x		x	x	x		x	0.917
10	x			x			x	x	x		x	0.917
11	x			x			x	x			x	0.920
12	x			x	x		x	x			x	0.909
13	x	x	x	x	x	x	x	x	x	x	x	0.917

Table 4.4: Configuration options used for the BDT training for 2016 samples. Other options used in the algorithm are kept to their default values [92].

Option	Value	Description
`NTrees`	`800`	Number of decision trees in the forest
`MinNodeSize`	`2.5%`	Minimum percentage of training events required in a leaf node
`BoostType`	`Grad`	Boosting method used
`Shrinkage`	`0.10`	Learning rate for GradBoost algorithm
`UseBaggedBoost`	`true`	Boost the forest of decision trees
`BaggedSampleFraction`	`0.5`	Relative size of bagged event sample to original size of the data sample
`nCuts`	`20`	Number of cuts performed on one decision tree
`MaxDepth`	`3`	Max depth of the decision tree

The features and distributions of the input variables and classifiers for the different data taking years and final states are described in the following sections.

BDT configuration for 2016

The BDT training was performed separately for the three different four lepton final states ($b\bar{b}4\mu$, $b\bar{b}4e$, and $b\bar{b}2e2\mu$) and the configuration options used for the algorithm training are reported in Table 4.4. The area under the ROC curve values obtained in these three cases are reported in Table 4.5. The ROC curves obtained for training and testing samples in the $b\bar{b}4\mu$ final state are shown in Figure 4.7.

Table 4.5: Area under the ROC curve (AUC) values obtained in the three different final states for 2016 datasets.

	$b\bar{b}4\mu$	$b\bar{b}4e$	$b\bar{b}2e2\mu$
AUC	0.920	0.908	0.916

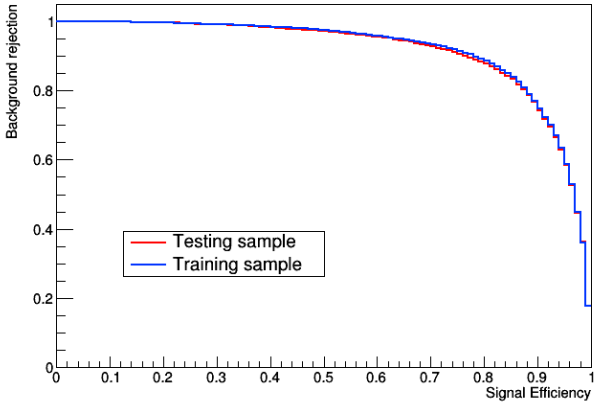

Figure 4.7: ROC curves obtained for training and testing 2016 samples in the $b\bar{b}4\mu$ final state.

Table 4.6: Ranking of the BDT input variables for 2016 samples.

order	variable	ranking
1	$bdisc_{j1}$	$1.181e-01$
2	m_{jj}	$1.141e-01$
3	$bdisc_{j2}$	$1.098e-01$
4	ΔR_{HH}	$1.095e-01$
5	pT_{lep2}	$9.877e-02$
6	pT_{j1}	$9.584e-02$
7	pT_{lep4}	$9.351e-02$
8	pT_{lep1}	$9.194e-02$
9	pT_{lep3}	$8.688e-02$
10	pT_{j2}	$8.164e-02$

From the plot, it is possible to notice that the two ROC curves are superimposed. This is an indication that the algorithm is retaining enough generalisation capabilities and does not present signs of over-fitting the training set (i.e. it is not *over-training*).
The BDT input variables distributions for signal and background samples, obtained in the $b\bar{b}4\mu$ final state, are shown in Figure 4.8. In these plots it is possible to observe the differences between signal and background distributions. The ranking of the BDT input variables is reported in Table 4.6. These figures are obtained by counting how often the variables are used to split the decision tree nodes, and by weighting each split occurrence by the signal-background separation gain-squared it has achieved and by the number of events in each node [92]. The ranking values of the different variables are very similar, but it is possible to notice that the jets

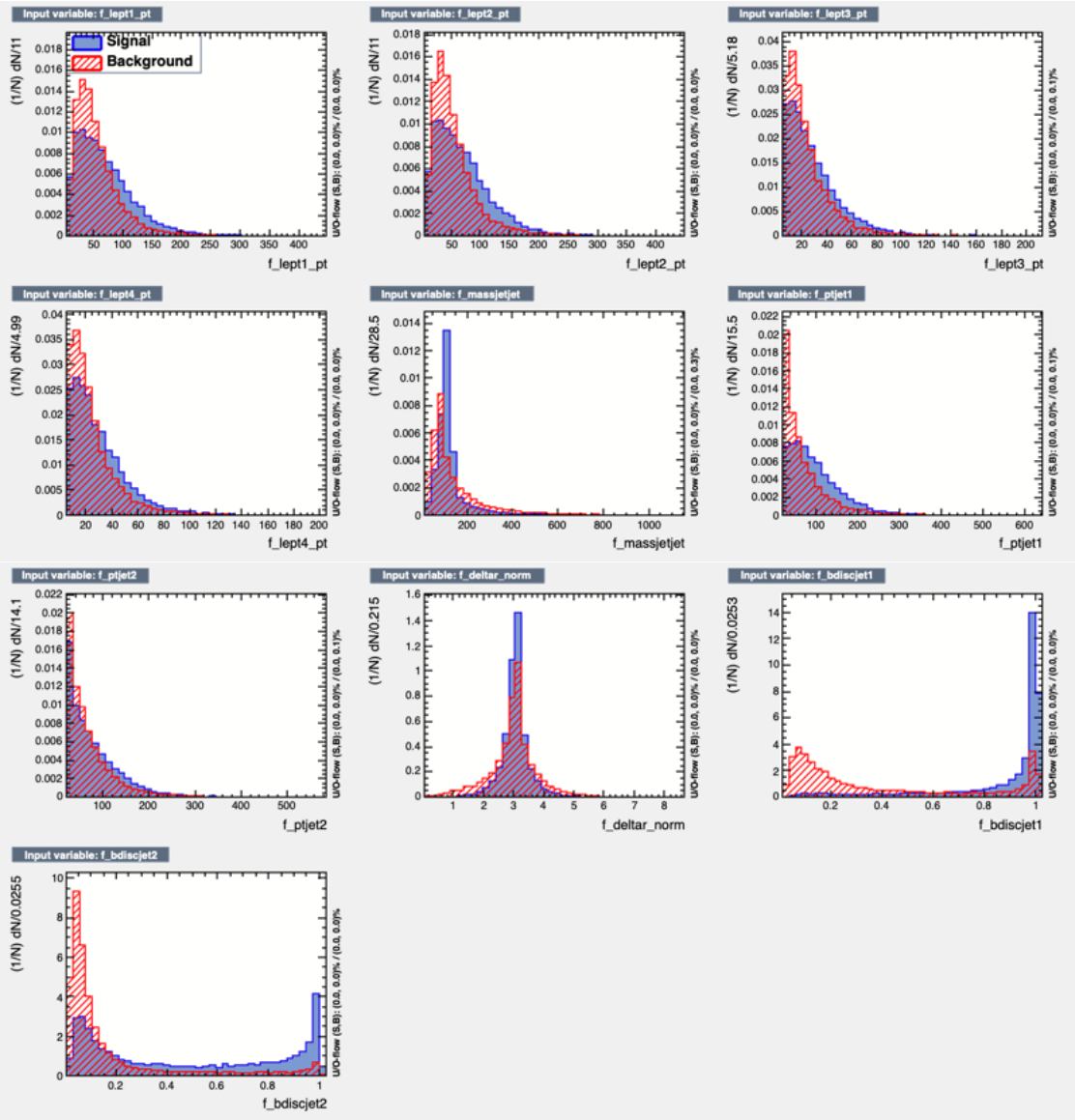

Figure 4.8: Distributions of BDT input variables for signal (solid blue) and background (striped red) 2016 samples, in the $b\bar{b}4\mu$ final state.

Table 4.7: Configuration options used for the BDT training for 2017 samples. Other options used in the algorithm are kept to their default values [92].

Option	Value	Description
NTrees	400	Number of decision trees in the forest
MinNodeSize	2.5%	Minimum percentage of training events required in a leaf node
BoostType	Grad	Boosting method used
Shrinkage	0.10	Learning rate for GradBoost algorithm
UseBaggedBoost	true	Boost the forest of decision trees
BaggedSampleFraction	0.5	Relative size of bagged event sample to original size of the data sample
nCuts	20	Number of cuts performed on one decision tree
MaxDepth	2	Max depth of the decision tree

Table 4.8: Area under the ROC curve (AUC) values obtained in the three different final states for 2017 datasets.

	$b\bar{b}4\mu$	$b\bar{b}4e$	$b\bar{b}2e2\mu$
AUC	0.942	0.943	0.941

variables, especially the b tag discriminant of the two jets and the di-jet invariant mass, are the most important for discriminating the signal and background events. The data-MC agreement for the BDT input variables was checked and Figure 4.9 reports the distributions of these variables obtained in the signal region (Section 4.1.4), with all the three final states ($b\bar{b}4\mu$, $b\bar{b}4e$, and $b\bar{b}2e2\mu$) summed together.

The BDT response is obtained applying the BDT to data, MC samples, and Z+X data-driven background, for each of the three final states. The response distributions of data, signal, and all background contributions are then used as input for the statistical analysis performed for extracting the final results. The distribution of the BDT response showing the data, signal, and all backgrounds contributions is reported in Figure 4.10. It is obtained combining the contributions of the three final states for 2016 samples. The BDT response distribution ranges from -1 to 1. Events that present background-like characteristics are distributed towards -1, while events more signal-like are concentrated around 1.

BDT configuration for 2017

The BDT training was performed separately for the three different four lepton final states ($b\bar{b}4\mu$, $b\bar{b}4e$, and $b\bar{b}2e2\mu$) and the configuration options used for the algorithm training are reported in Table 4.7. The area under the ROC curve values obtained in these three cases are reported in Table 4.8. The ROC curves obtained for training and testing samples in the $b\bar{b}4\mu$ final state are shown in Figure 4.11. The two ROC curves are superimposed, and thus the algorithm is retaining enough

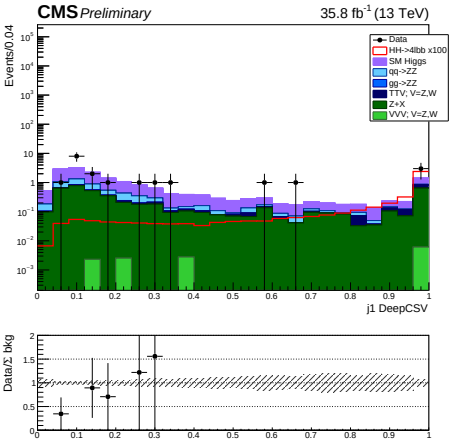

(a) B tagger score of the jet with the highest value of the deepCSV discriminant

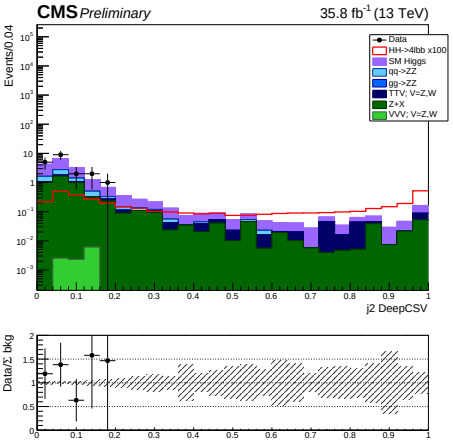

(b) B tagger score of the jet with the second-highest value of the deepCSV discriminant

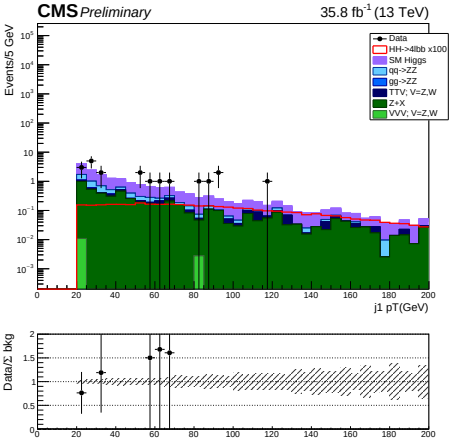

(c) p_T of jet with the highest value of the deepCSV discriminant

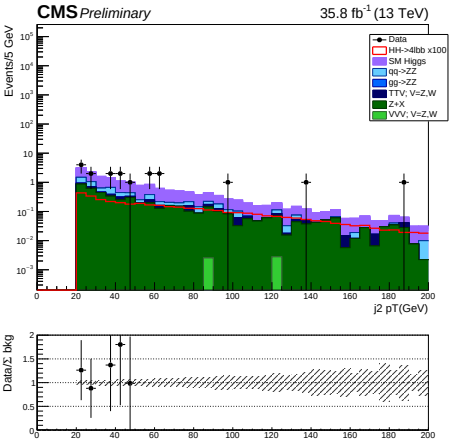

(d) p_T of jet with the second-highest value of the deepCSV discriminant

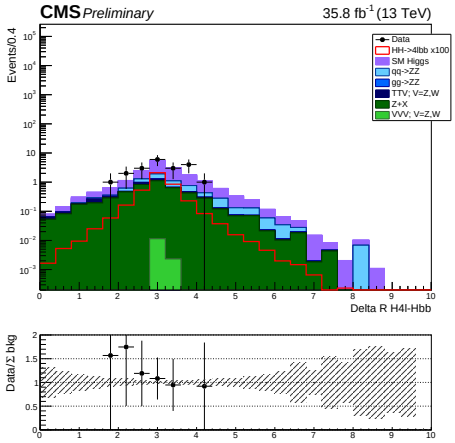

(e) ΔR between the $H \to 4\ell$ and $H \to b\bar{b}$

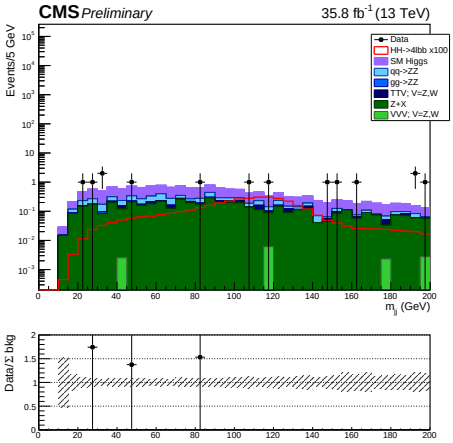

(f) Invariant di-jet mass built with the two jets with the highest value of the deepCSV discriminant

Figure 4.9: BDT input variables distributions for 2016 samples, obtained in the signal region. In the ratio plot, the grey dashed shades represent the relative statistical uncertainty on the total estimated background.

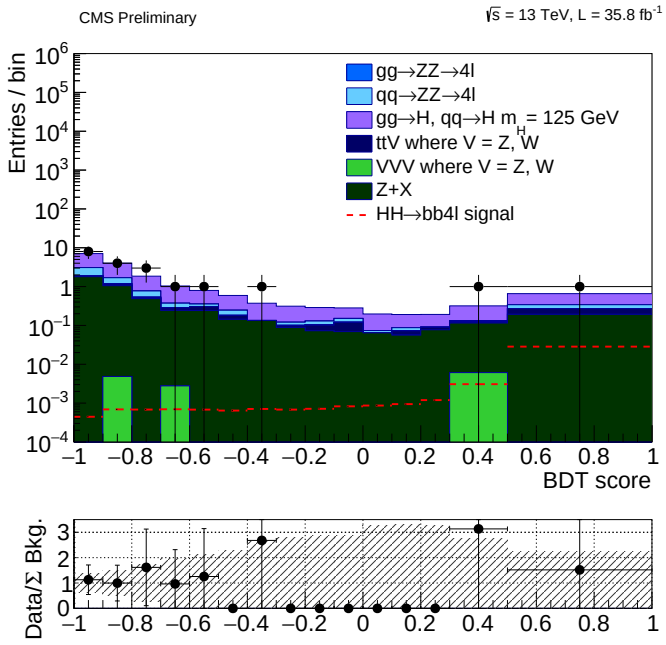

Figure 4.10: BDT response distribution obtained in the signal region for 2016 datasets. The distribution is obtained combining the contribution of the three final states ($b\bar{b}4\mu$, $b\bar{b}4e$, and $b\bar{b}2e2\mu$). In the ratio plot, the grey dashed shades represent the relative statistical uncertainty on the total estimated background.

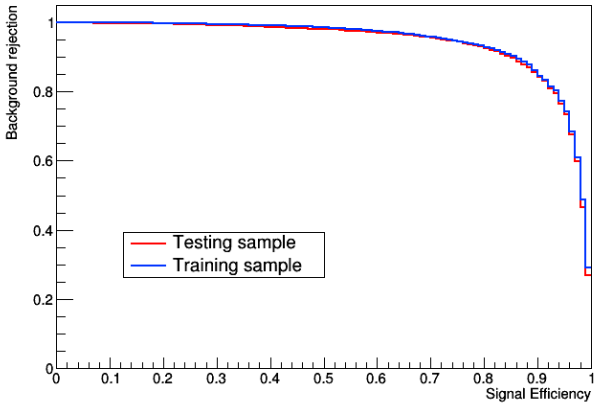

Figure 4.11: ROC curves obtained for training and testing 2017 samples in the $b\bar{b}4\mu$ final state.

Table 4.9: Ranking of the BDT input variables for 2017 samples.

order	variable	ranking
1	ΔR_{HH}	$1.261e-01$
2	$bdisc_{j1}$	$1.254e-01$
3	m_{jj}	$1.130e-01$
4	pT_{lep2}	$1.024e-01$
5	pT_{lep1}	$9.753e-02$
6	$bdisc_{j2}$	$9.504e-02$
7	pT_{lep4}	$9.431e-02$
8	pT_{j1}	$8.927e-02$
9	pT_{lep3}	$8.516e-02$
10	pT_{j2}	$7.180e-02$

generalisation capabilities and does not present signs of over-training.
The BDT input variables distributions for signal and background samples, obtained in the $b\bar{b}4\mu$ final state, are shown in Figure 4.12. The ranking of the BDT input variables is reported in Table 4.9. The ranking values of the different variables are very similar, but it is possible to notice that, as is 2016 dataset, the jets variables, especially the b tag discriminant of the two jets and the di-jet invariant mass, are important for discriminating the signal and background events. Also the angular difference between the two reconstructed Higgs bosons ΔR_{HH} plays an important role in discriminating signal and background events. The data-MC agreement for the BDT input variables was checked and Figure 4.13 reports the distributions of these variables obtained in the signal region (Section 4.1.4), with all the three final states ($b\bar{b}4\mu$, $b\bar{b}4e$, and $b\bar{b}2e2\mu$) summed together.

The BDT response is obtained with the same procedure used for 2016 dataset. The distribution of the BDT response showing the data, signal, and all backgrounds contributions is reported in Figure 4.14. It is obtained combining the contributions of the three final states for 2017 samples.

BDT configuration for 2018

The BDT training was performed separately for the three different four lepton final states ($b\bar{b}4\mu$, $b\bar{b}4e$, and $b\bar{b}2e2\mu$) and the configuration options used for the algorithm training are reported in Table 4.10. The area under the ROC curve values obtained in these three cases are reported in Table 4.11. The ROC curves obtained for training and testing samples in the $b\bar{b}4\mu$ final state are shown in Figure 4.15. The two ROC curves are superimposed, and thus the algorithm is retaining enough generalisation capabilities and does not present signs of over-training.

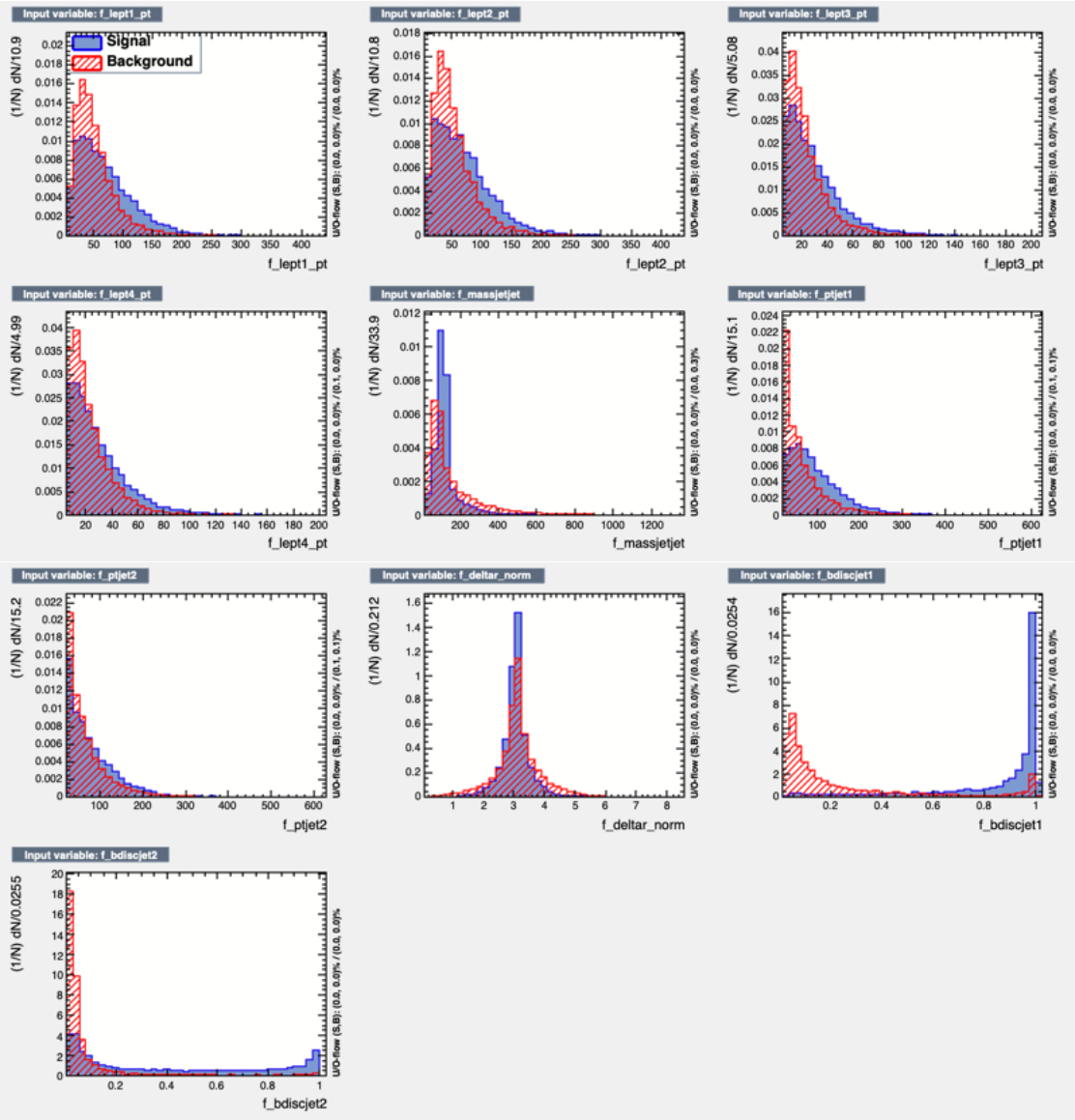

Figure 4.12: Distributions of BDT input variables for signal (solid blue) and background (striped red) 2017 samples, in the $b\bar{b}4\mu$ final state.

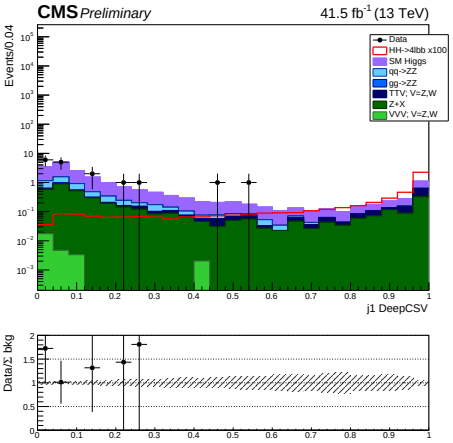

(a) B tagger score of the jet with the highest value of the deepCSV discriminant

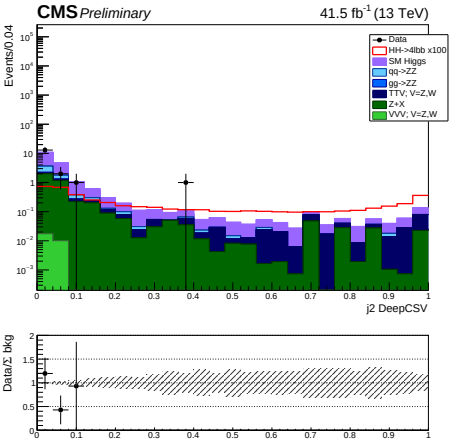

(b) B tagger score of the jet with the second-highest value of the deepCSV discriminant

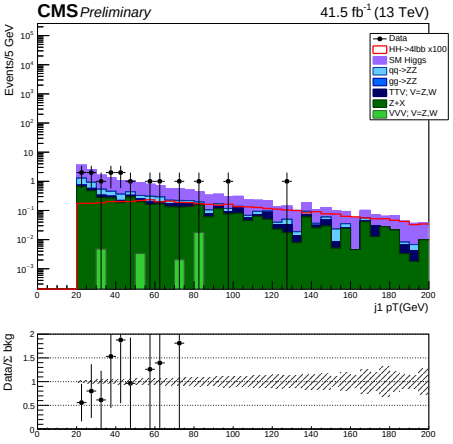

(c) p_T of jet with the highest value of the deepCSV discriminant

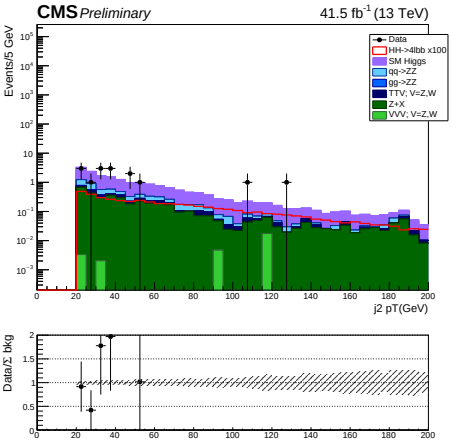

(d) p_T of jet with the second-highest value of the deepCSV discriminant

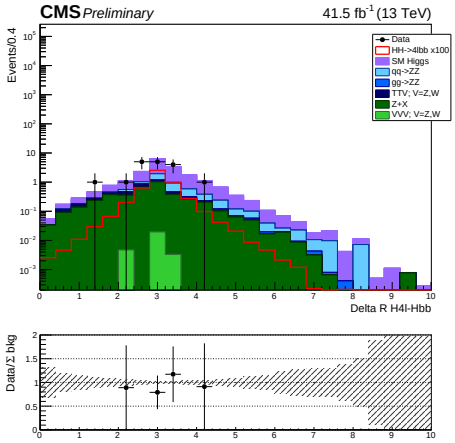

(e) ΔR between the H $\to 4\ell$ and H $\to b\bar{b}$

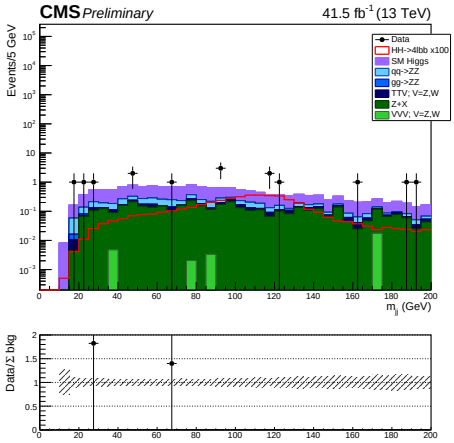

(f) Invariant di-jet mass built with the two jets with the highest value of the deepCSV discriminant

Figure 4.13: BDT input variables distributions for 2017 samples, obtained in the signal region. In the ratio plot, the grey dashed shades represent the relative statistical uncertainty on the total estimated background.

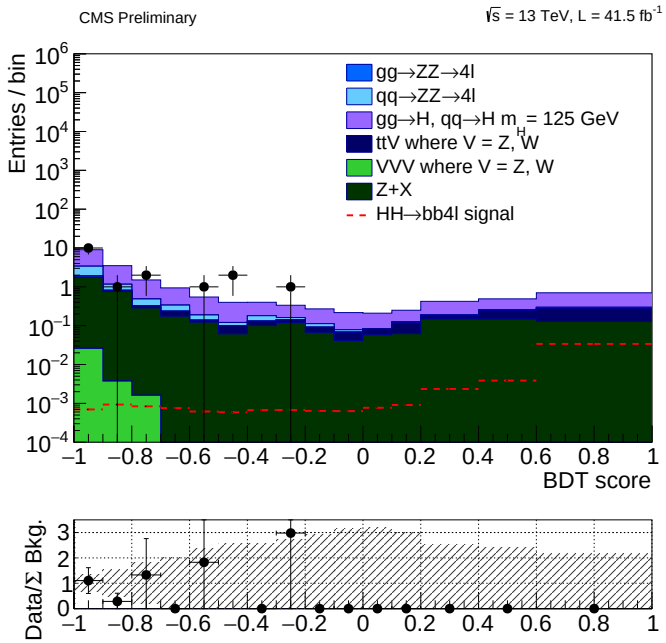

Figure 4.14: BDT response distribution obtained in the signal region for 2017 datasets. The distribution is obtained combining the contribution of the three final states ($b\bar{b}4\mu$, $b\bar{b}4e$, and $b\bar{b}2e2\mu$). In the ratio plot, the grey dashed shades represent the relative statistical uncertainty on the total estimated background.

Table 4.10: Configuration options used for the BDT training for 2018 samples. Other options used in the algorithm are kept to their default values [92].

Option	Value	Description
`NTrees`	`400`	Number of decision trees in the forest
`MinNodeSize`	`2.5%`	Minimum percentage of training events required in a leaf node
`BoostType`	`Grad`	Boosting method used
`Shrinkage`	`0.10`	Learning rate for GradBoost algorithm
`UseBaggedBoost`	`true`	Boost the forest of decision trees
`BaggedSampleFraction`	`0.5`	Relative size of bagged event sample to original size of the data sample
`nCuts`	`20`	Number of cuts performed on one decision tree
`MaxDepth`	`2`	Max depth of the decision tree

Table 4.11: Area under the ROC curve (AUC) values obtained in the three different final states for 2018 datasets.

	$b\bar{b}4\mu$	$b\bar{b}4e$	$b\bar{b}2e2\mu$
AUC	0.924	0.920	0.926

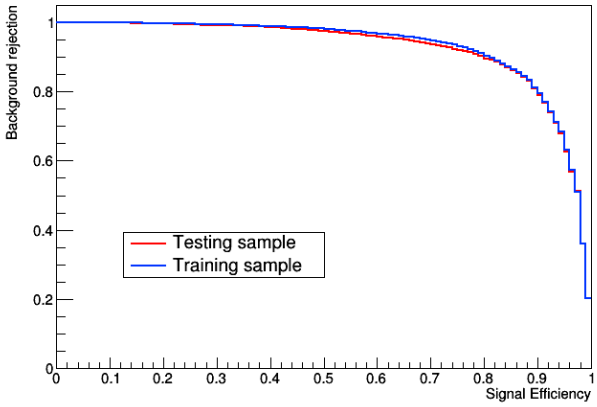

Figure 4.15: ROC curves obtained for training and testing 2018 samples in the $b\bar{b}4\mu$ final state.

Table 4.12: Ranking of the BDT input variables for 2018 samples.

order	variable	ranking
1	$bdisc_{j1}$	$1.276e-01$
2	ΔR_{HH}	$1.111e-01$
3	$bdisc_{j2}$	$1.088e-01$
4	m_{jj}	$1.075e-01$
5	pT_{lep1}	$1.001e-01$
6	pT_{lep2}	$9.905e-02$
7	pT_{j1}	$9.376e-02$
8	pT_{lep4}	$9.262e-02$
9	pT_{lep3}	$8.229e-02$
10	pT_{j2}	$7.721e-02$

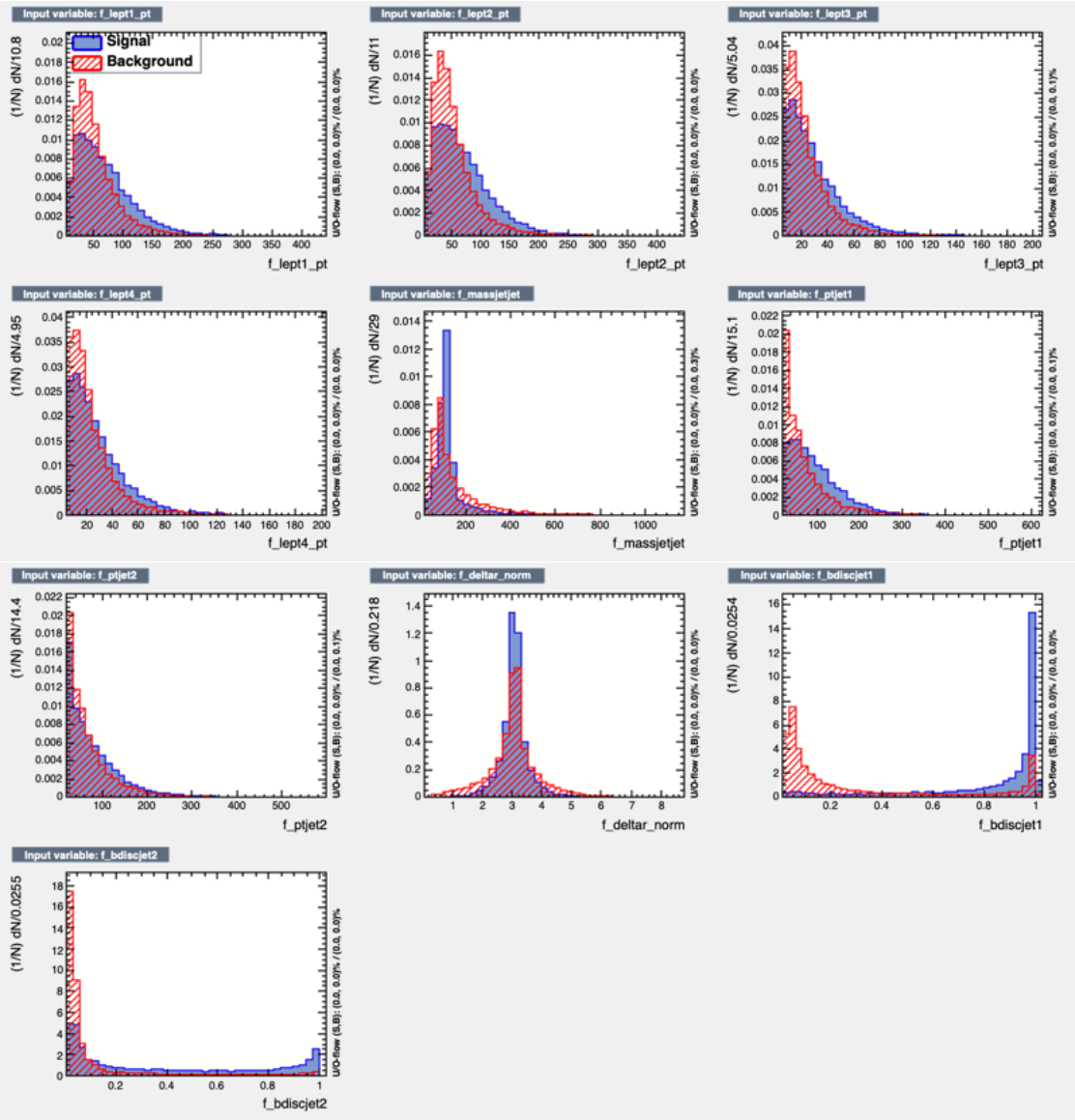

Figure 4.16: Distributions of BDT input variables for signal (solid blue) and background (striped red) 2018 samples, in the $b\bar{b}4\mu$ final state.

The BDT input variables distributions for signal and background samples, obtained in the $b\bar{b}4\mu$ final state, are shown in Figure 4.16. The ranking of the BDT input variables is reported in Table 4.12. The ranking values of the different variables are very similar, but it is possible to notice that the jets variables, especially the b tag discriminant of the two jets and the di-jet invariant mass, and the angular difference between the two reconstructed Higgs bosons ΔR_{HH} are important for discriminating the signal and background events. The data-MC agreement for the BDT input variables was checked and Figure 4.17 reports the distributions of these variables obtained in the signal region (Section 4.1.4), with all the three final states ($b\bar{b}4\mu$, $b\bar{b}4e$, and $b\bar{b}2e2\mu$) summed together.

The BDT response is obtained with the same procedure used for 2016 and 2017 datasets. The distribution of the BDT response showing the data, signal, and all backgrounds contributions is reported in Figure 4.18. It is obtained combining the contributions of the three final states for 2018 samples.

4.3.3 Control regions

In order to validate the BDT strategy, the data-MC agreement for the BDT input variables was checked in regions containing a higher number of events with respect to the signal region, before looking at variables description in the region of interest (presented in the previous section 4.3.2). Three *control regions* were defined for this purpose:

- 4ℓ side-bands, built to check the distribution of lepton-related variables,
- $2\ell 2jets$ control region, useful for checking jet variables,
- $4\ell 2jets$ side-bands, built to check BDT input variables in a region similar to the signal region but containing more events.

4l side-bands

The 4ℓ side-bands control region is built to check the level of agreement of the lepton variables distributions between data and MC. In particular, the distribution of the p_T of the four selected leptons is checked in this region. The control region is built from events passing the $\mathrm{H} \to 4\ell$ selection (Section 4.1.2), and considering only events outside the mass window $115 < m_{4\ell} < 135$ GeV/c^2, thus excluding the signal. The distributions of the p_T of the four selected leptons are reported in Figure 4.19, obtained separately for the three different data taking years. The plots are obtained summing together the contributions of the three possible 4ℓ final states (4μ, $4e$, and $2e2\mu$). From the plots it is possible to observe a good data-MC agreement, thus the description of lepton-related variables considered in the analysis is under control.

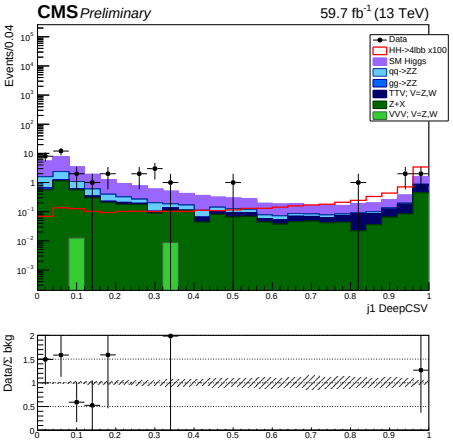

(a) B tagger score of the jet with the highest value of the deepCSV discriminant

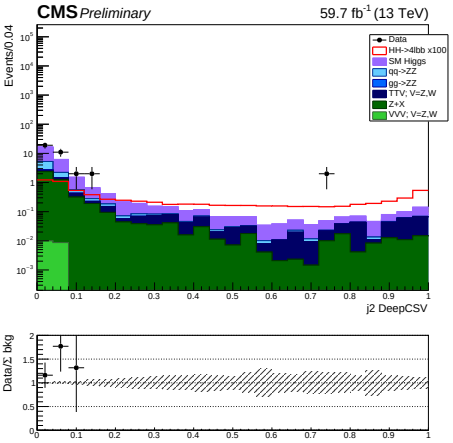

(b) B tagger score of the jet with the second-highest value of the deepCSV discriminant

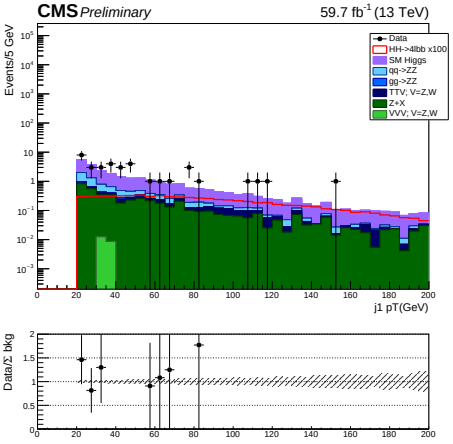

(c) p_T of jet with the highest value of the deepCSV discriminant

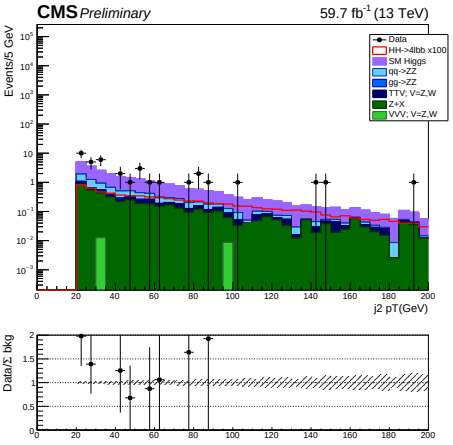

(d) p_T of jet with the second-highest value of the deepCSV discriminant

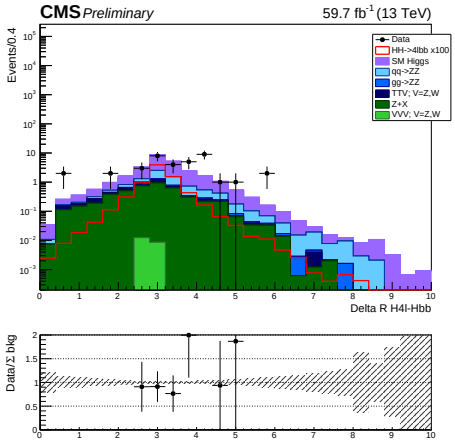

(e) ΔR between the $H \to 4\ell$ and $H \to b\bar{b}$

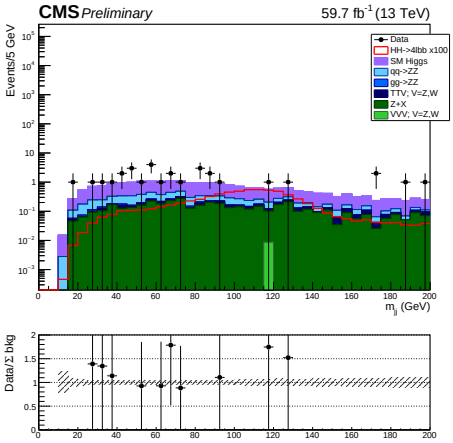

(f) Invariant di-jet mass built with the two jets with the highest value of the deepCSV discriminant

Figure 4.17: BDT input variables distributions for 2018 samples, obtained in the signal region. In the ratio plot, the grey dashed shades represent the relative statistical uncertainty on the total estimated background.

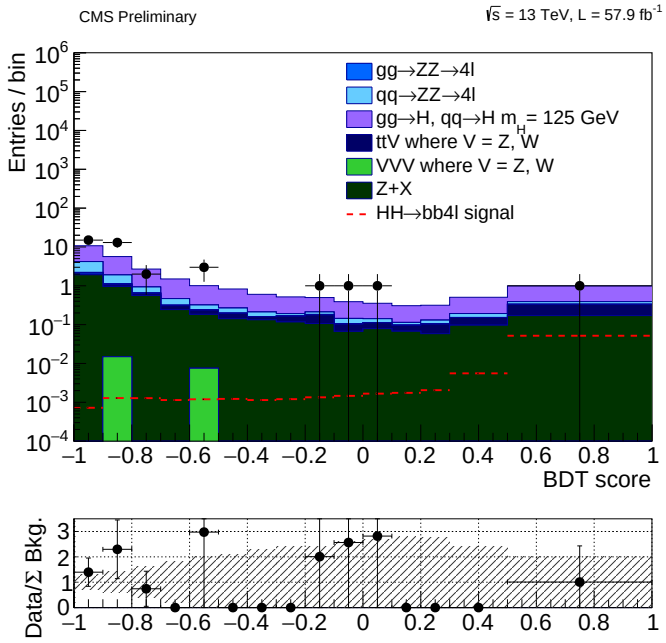

Figure 4.18: BDT response distribution obtained in the signal region for 2018 datasets. The distribution is obtained combining the contribution of the three final states ($b\bar{b}4\mu$, $b\bar{b}4e$, and $b\bar{b}2e2\mu$) for each year. In the ratio plot, the grey dashed shades represent the relative statistical uncertainty on the total estimated background.

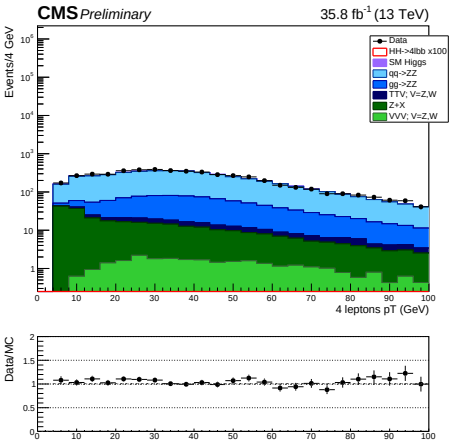

(a) Four-lepton transverse momentum distribution for 2016 datasets.

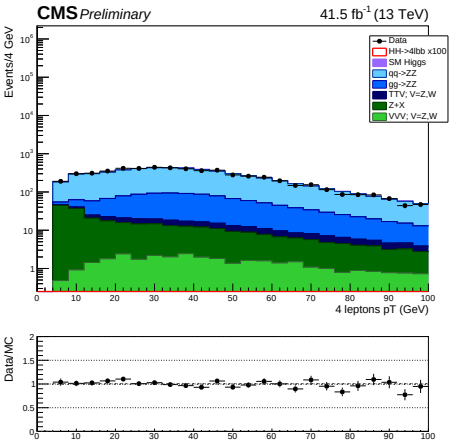

(b) Four-lepton transverse momentum distribution for 2017 datasets.

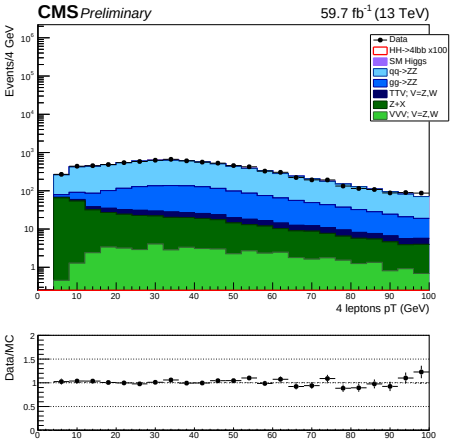

(c) Four-lepton transverse momentum distribution for 2018 datasets.

Figure 4.19: Four-lepton transverse momentum distributions, obtained in the 4ℓ sidebands control region.

2l2jets control region

The $2\ell 2jets$ control region is built requiring the presence of two leptons forming a Z candidate (Section 4.1.2) and two jets passing the selection required for the $H \to b\bar{b}$ candidate (Section 4.1.3). This region is chosen to check the data-MC agreement for jets variables distributions. In particular, the p_T and the b tag score of the two selected jets are considered. The di-jet invariant mass is also checked. The distributions of these variables, together with the invariant mass distribution of the two selected leptons, are reported in Figure 4.20, 4.21, and 4.22 for 2016, 2017, and 2018 samples, respectively.
In this region the Drell-Yan and $t\bar{t}$ contributions are estimated using dedicated MC samples, since the selection is less stringent with respect to the signal region, where these contributions are estimated with a data-driven method (Z+X background, see Section 4.2.5).
The data-MC agreement observed from the plots is good, thus the jets variables considered in the analysis are well described by MC samples.

4l2jets side-bands

The $4\ell 2jets$ side-bands control region is built requiring event to pass the $H \to 4\ell$ selection, defined in Section 4.1.2, and the $H \to b\bar{b}$ selection, defined in Section 4.1.3. Then, only events contained in the regions $95 < m_{4\ell} < 115$ GeV/c^2 and $135 < m_{4\ell} < 170$ GeV/c^2 are considered. This control region is defined to check the data-MC agreement of the variables used as input of the BDT algorithm in a region similar to the signal region (Section 4.1.4) but containing more events. The distributions of these variables are reported in Figure 4.23, Figure 4.24, and Figure 4.25 for 2016, 2017, and 2018 samples, respectively. From these plots, obtained summing together the contributions of the three possible 4ℓ final states ($b\bar{b}4\mu$, $b\bar{b}4e$, and $b\bar{b}2e2\mu$), it is possible to observe a good agreement between data and background estimation, despite the low number events contained in this control region.
The data-MC agreement is checked also looking at the yields obtained in this control region for the three 4ℓ final states. The yields reported in Table 4.13 for 2016, 2017, and 2018 samples show a good agreement between data and backgrounds estimation.

4.4 Systematic uncertainties

The imperfect knowledge of the detector response, or uncertainties in the theoretical predictions are some of the known "unknowns" that can make the modelling of signal backgrounds imperfect, biasing the final results of the analysis. Estimating these "unknowns"is therefore a fundamental step for the extraction of the analy-

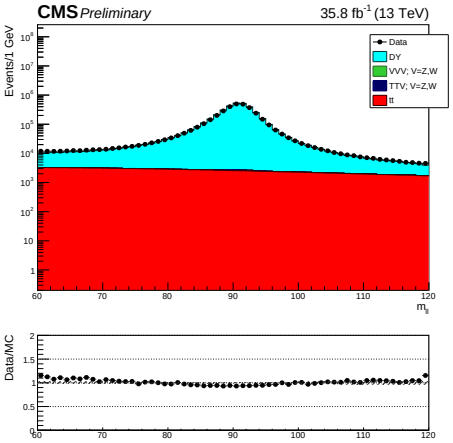

(a) Di-lepton invariant mass distribution.

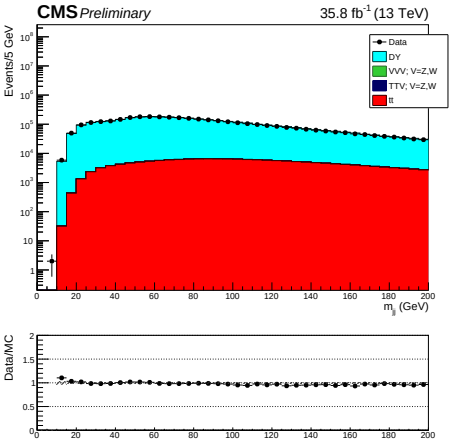

(b) Di-jet invariant mass distribution.

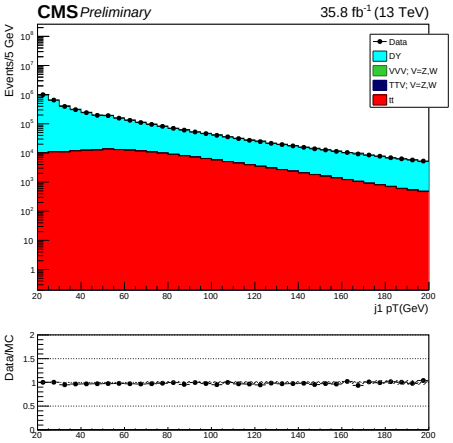

(c) Transverse momentum of the jet with the highest value of the b tagger discriminant.

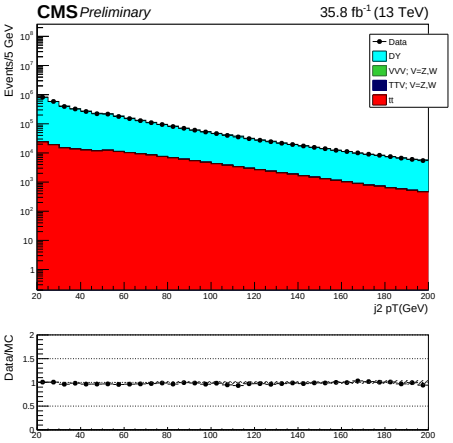

(d) Transverse momentum of the jet with the second highest value of the b tagger discriminant.

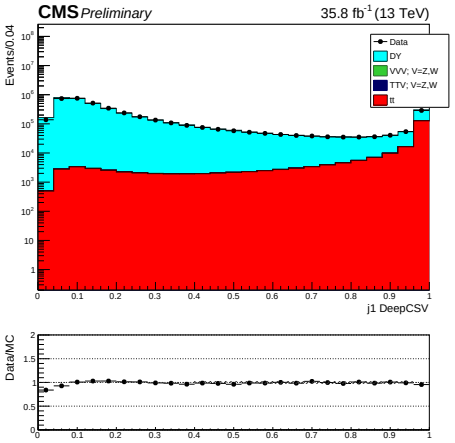

(e) B tagger score of the jet with the highest value of the btagger discriminant.

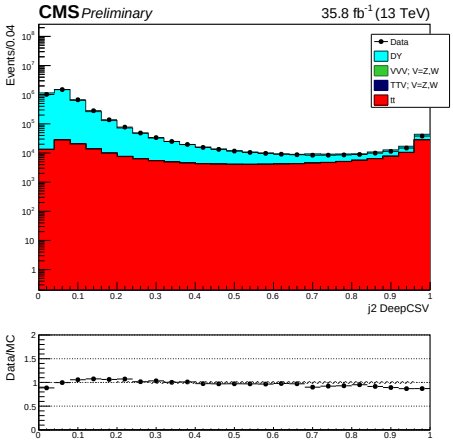

(f) B tagger score of the jet with the second highest value of the b tagger discriminant.

Figure 4.20: Distributions of jet variables obtained in the $2\ell 2jets$ control region, for the 2016 dataset.

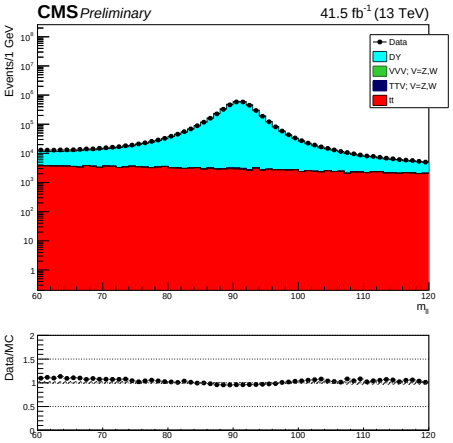

(a) Di-lepton invariant mass distribution.

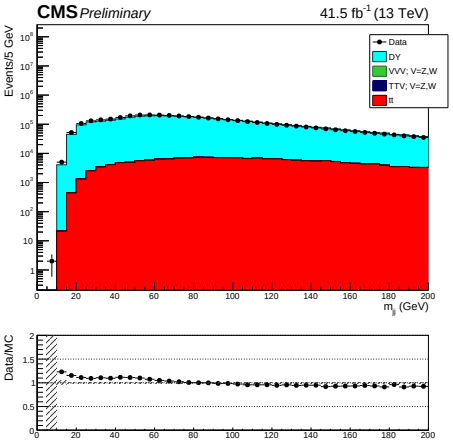

(b) Di-jet invariant mass distribution.

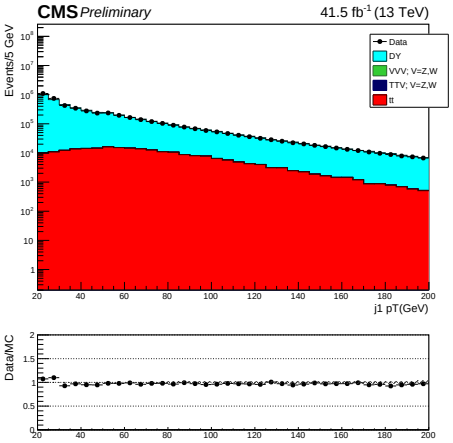

(c) Transverse momentum of the jet with the highest value of the b tagger discriminant.

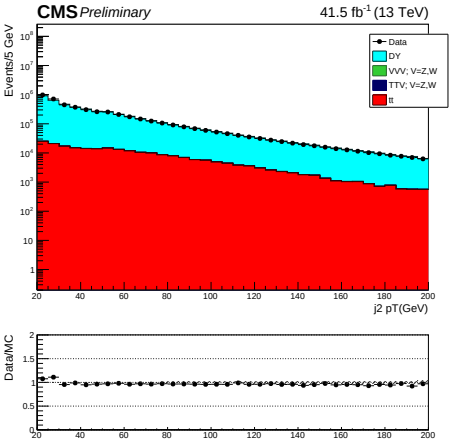

(d) Transverse momentum of the jet with the second highest value of the b tagger discriminant.

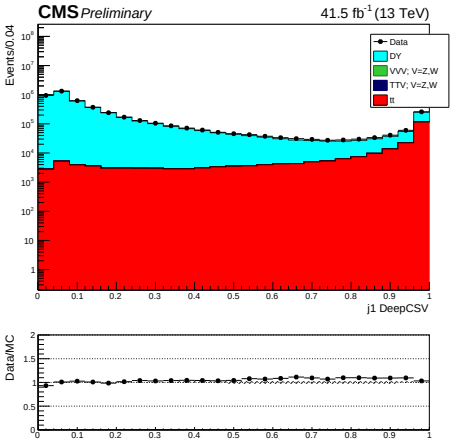

(e) B tagger score of the jet with the highest value of the btagger discriminant.

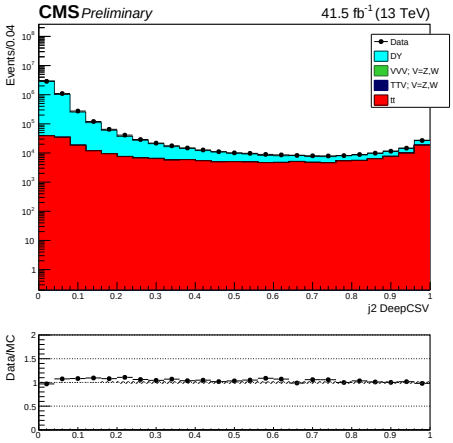

(f) B tagger score of the jet with the second highest value of the b tagger discriminant.

Figure 4.21: Distributions of jet variables obtained in the $2\ell 2jets$ control region, for the 2017 dataset.

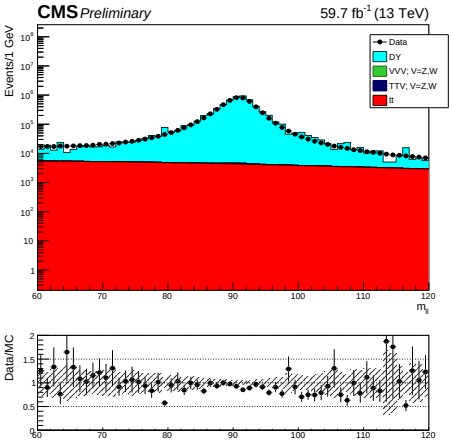

(a) Di-lepton invariant mass distribution.

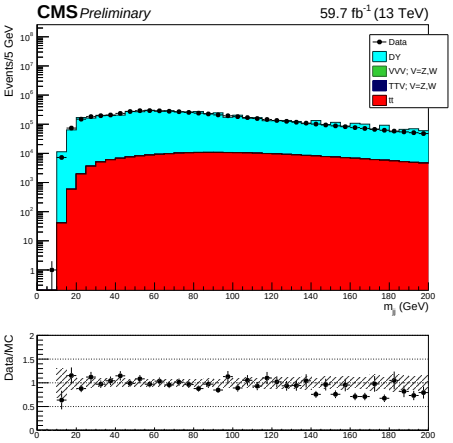

(b) Di-jet invariant mass distribution.

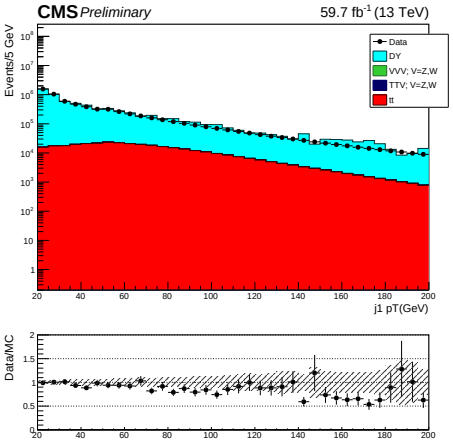

(c) Transverse momentum of the jet with the highest value of the b tagger discriminant.

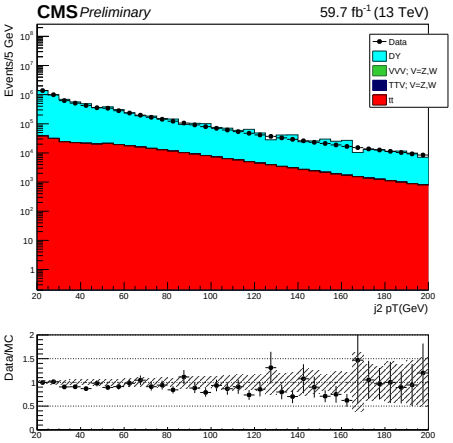

(d) Transverse momentum of the jet with the second highest value of the b tagger discriminant.

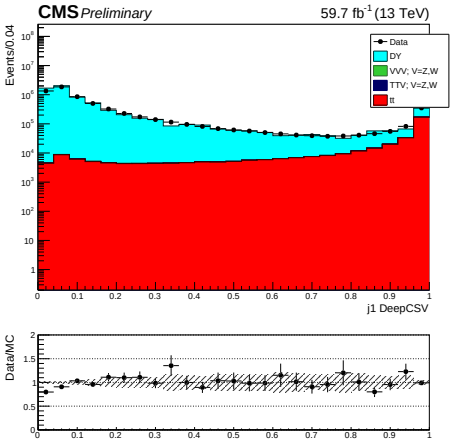

(e) B tagger score of the jet with the highest value of the btagger discriminant.

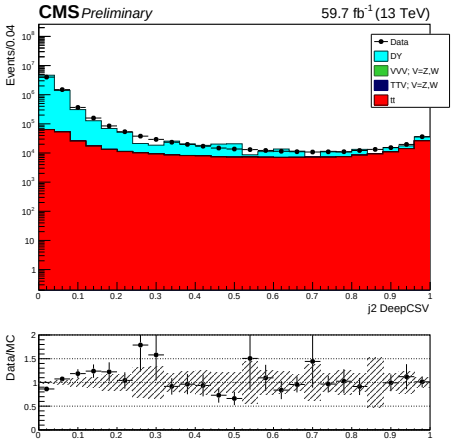

(f) B tagger score of the jet with the second highest value of the b tagger discriminant.

Figure 4.22: Distributions of jet variables obtained in the $2\ell 2jets$ control region, for the 2018 dataset.

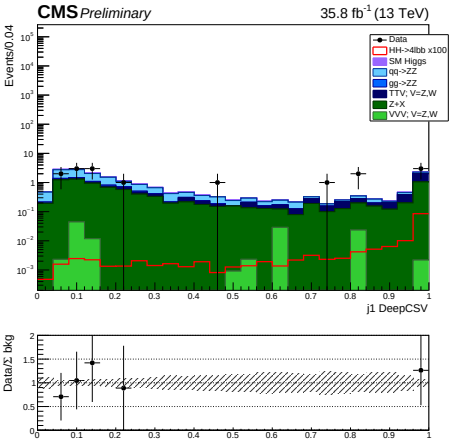

(a) B tagger score of the jet with the highest value of the b tagger discriminant.

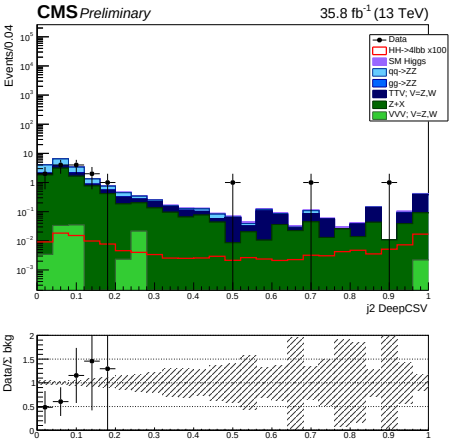

(b) B tagger score of the jet with the second highest value of the b tagger discriminant.

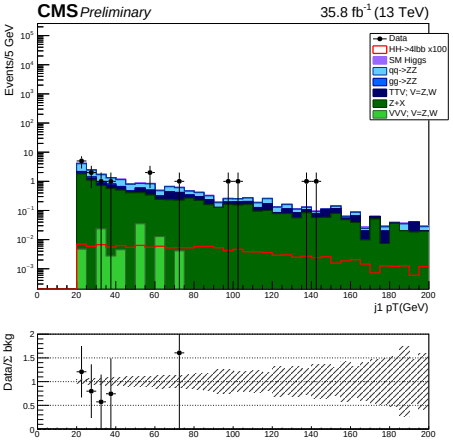

(c) p_T of jet with the highest value of b tagger discriminant.

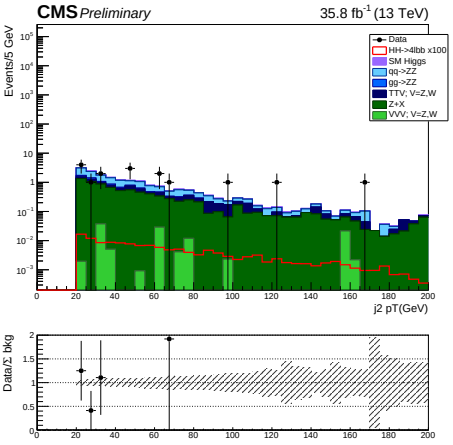

(d) p_T of jet with the second highest value of b tagger discriminant.

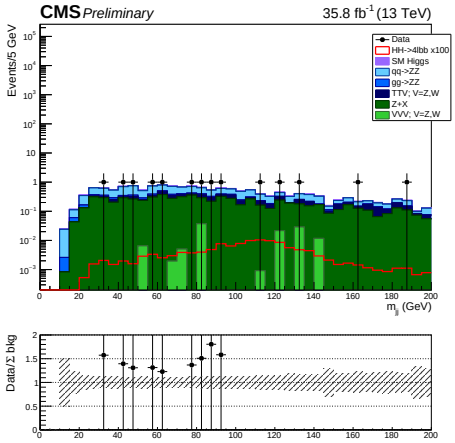

(e) Di-jet invariant mass distribution.

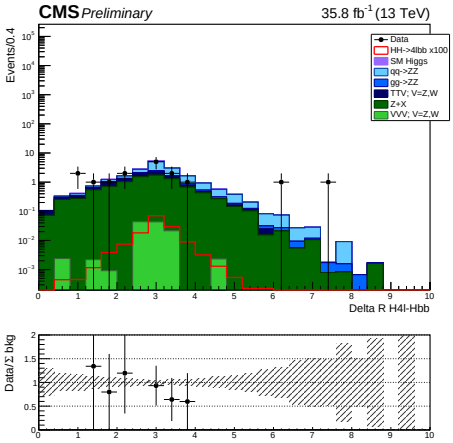

(f) ΔR between $H \to 4\ell$ and $H \to b\bar{b}$.

Figure 4.23: Distributions of BDT input variables obtained in the $4\ell 2jets$ side-bands control region for the 2016 dataset.

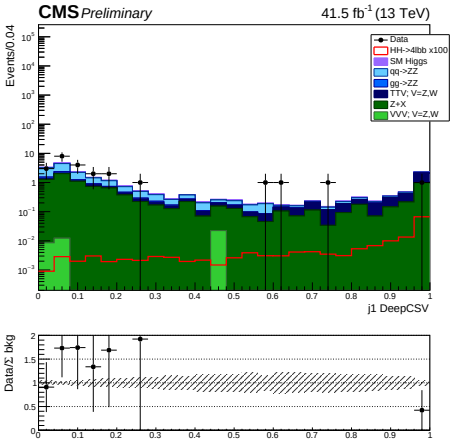

(a) B tagger score of the jet with the highest value of the b tagger discriminant.

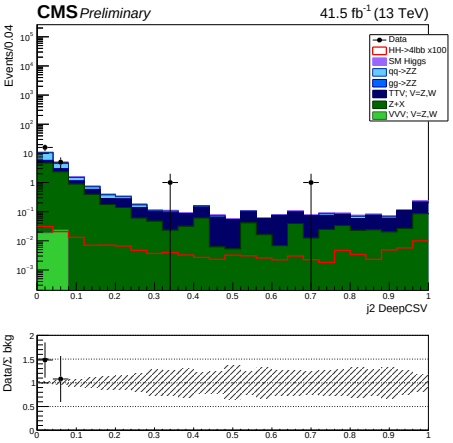

(b) B tagger score of the jet with the second highest value of the b tagger discriminant.

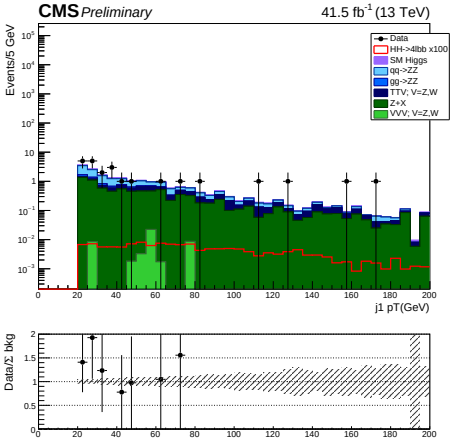

(c) p_T of jet with the highest value of b tagger discriminant.

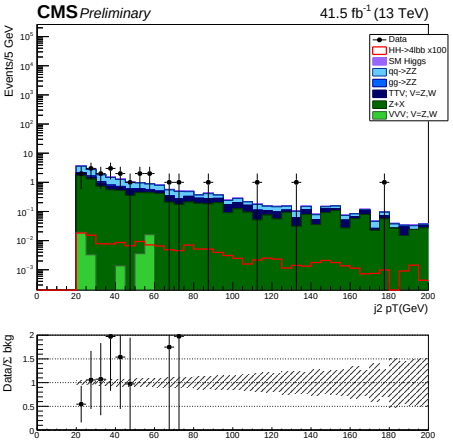

(d) p_T of jet with the second highest value of b tagger discriminant.

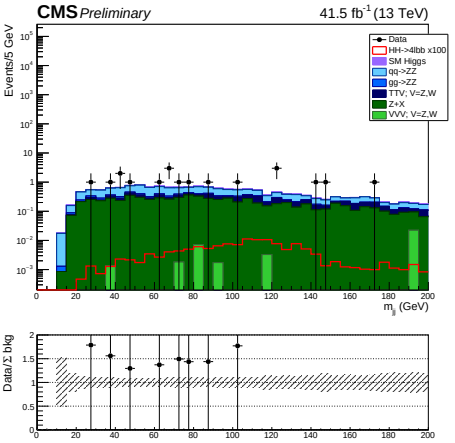

(e) Di-jet invariant mass distribution.

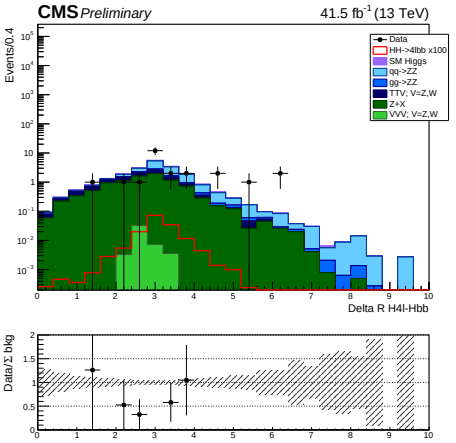

(f) ΔR between $H \to 4\ell$ and $H \to b\bar{b}$.

Figure 4.24: Distributions of BDT input variables obtained in the $4\ell 2jets$ side-bands control region for the 2017 dataset.

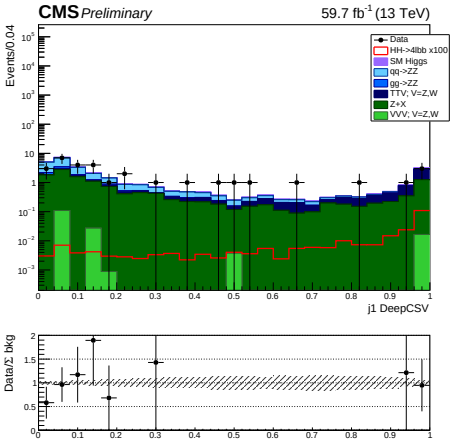

(a) B tagger score of the jet with the highest value of the b tagger discriminant.

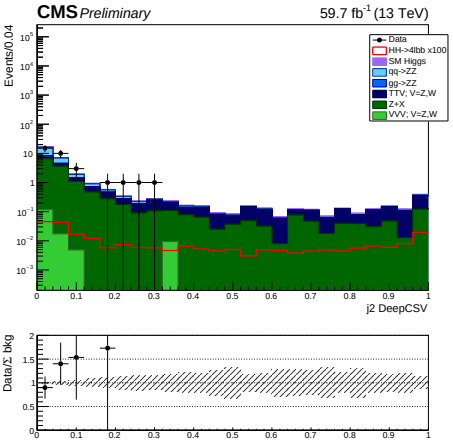

(b) B tagger score of the jet with the second highest value of the b tagger discriminant.

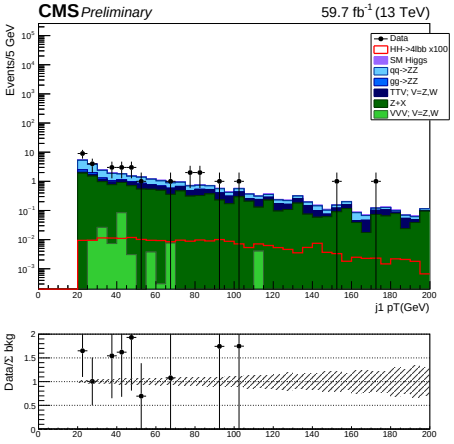

(c) p_T of jet with the highest value of b tagger discriminant.

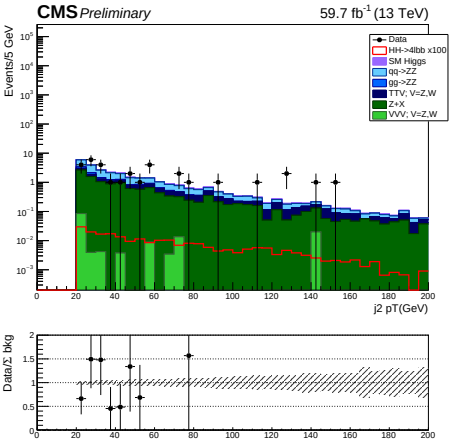

(d) p_T of jet with the second highest value of b tagger discriminant.

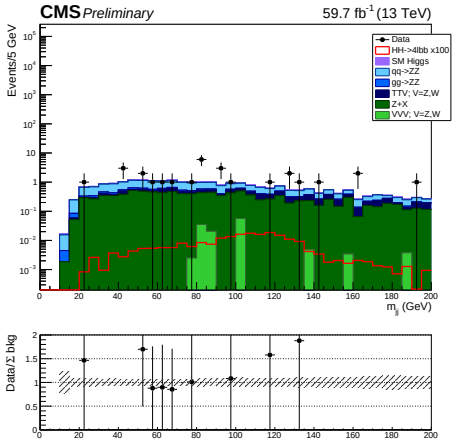

(e) Di-jet invariant mass distribution.

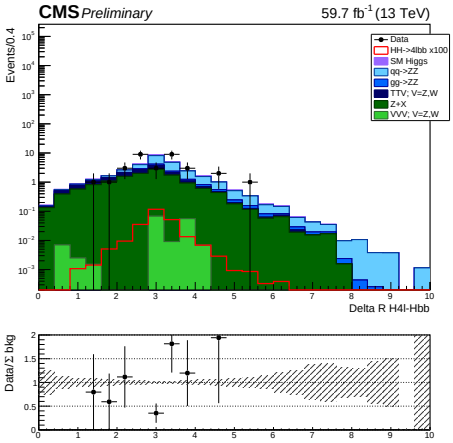

(f) ΔR between H $\to 4\ell$ and H $\to b\bar{b}$.

Figure 4.25: Distributions of BDT input variables obtained in the $4\ell 2jets$ side-bands control region for the 2018 dataset.

Table 4.13: Yields obtained in the $4\ell 2jets$ side-bands control region for 2016, 2017, and 2018 datasets. The column "TTV" contains contributions from TTW and TTV processes, while the column "VVV" contains the contributions from WWZ, WZZ, and ZZZ processes.

Final state	HH signal	SM Higgs	qqZZ	ggZZ	TTV	Z+X	VVV	All backgrounds	Data
2016 dataset									
$b\bar{b}4\mu$	0.0003	0.21	2.71	0.27	0.61	3.53	0.004	7.33	6
$b\bar{b}4e$	0.0004	0.17	1.53	0.20	0.42	1.04	0.031	3.39	4
$b\bar{b}2e2\mu$	0.0007	0.35	2.79	0.37	1.11	4.47	0.081	9.17	6
$b\bar{b}4\ell$	0.0014	0.73	7.03	0.84	2.14	9.04	0.116	19.89	16
2017 dataset									
$b\bar{b}4\mu$	0.0004	0.23	2.88	0.33	0.89	3.73	0.007	8.07	11
$b\bar{b}4e$	0.0004	0.17	1.33	0.21	0.48	0.89	0.026	3.11	5
$b\bar{b}2e2\mu$	0.0008	0.39	3.10	0.38	1.27	4.70	0.011	9.85	8
$b\bar{b}4\ell$	0.0016	0.79	7.31	0.92	2.64	9.32	0.044	21.03	24
2018 dataset									
$b\bar{b}4\mu$	0.0006	0.35	4.46	0.53	1.16	5.84	0.07	12.4	12
$b\bar{b}4e$	0.0006	0.27	2.07	0.30	0.67	1.31	0.03	4.67	6
$b\bar{b}2e2\mu$	0.0012	0.57	4.87	0.62	2.00	6.15	0.05	14.3	14
$b\bar{b}4\ell$	0.0024	1.19	11.4	1.45	3.83	13.3	0.15	31.37	32

sis results. These effects are taken into account as *systematic uncertainties*, that are then included as *nuisance parameters* in the statistical analysis performed to extract the results (Section 5.2).
The systematic uncertainties considered in the analysis can have different effects. *Normalization* uncertainties affect the normalization of processes, describing the possible modifications to the expected yields; *shape* uncertainties describe the possible modifications to the shape of the BDT response distributions, independently from the normalisation. Yields and BDT response distributions are used as input to the statistical analysis (Section 5.2).
The different sources of systematics can be divided in *theoretical* uncertainties, related theory hypotheses and computations, and *experimental* uncertainties, associated to detector response or data-driven methods for background estimation.
The sources of systematic uncertainties considered in this analysis are reported in the following sections.

4.4.1 Theoretical uncertainties

Theoretical uncertainties arise from the choice of the PDF set, the uncertainty on α_s, the renormalization and factorization QCD scale ([93]). These sources of uncertainties affect both signal and backgrounds processes. For the HH signal [94], in addition to the sources just described, an additional uncertainty related to missing finite top-quark mass effects considered for the cross-section computation is present. Systematic uncertainties affecting the HH signal and the single Higgs boson backgrounds are determined centrally in CMS for all relevant analyses. For

all the other backgrounds, the systematic uncertainties are evaluated by varying the QCD scale and the PDF set used for computing the considered sample cross section.
An additional uncertainty of 10% on the k-factor is used for the gg $\rightarrow$ ZZ prediction and of 0.1% for the qq $\rightarrow$ ZZ prediction. The summary of theoretical systematic uncertainties is reported in Table 4.14.
All theoretical sources of systematics are normalization uncertainties and are considered correlated among the three data taking years.

4.4.2 Experimental uncertainties

Experimental uncertainties considered in the analysis are diverse and arise from different sources. The uncertainty on the integrated luminosity, ranging from 2.3 to 2.6% for the different data taking years, affects normalization. The uncertainty on the lepton identification and reconstruction efficiency ranges from 1 to 15.5% on the overall event yield for the different final states.
Uncertainties on the b tagging scale factors (see Section 3.3.6) are obtained by propagating through the event reconstruction chain, up to the BDT response, the up and down variations of the b tagging scale factors due to different sources of uncertainties related to the jets p_T, η and hadron flavour composition. They result in shape uncertainties on the BDT response distributions.
The uncertainties on the jet energy scale (JES) and jet energy resolution (JER) are accounted for by changing the jet response by one standard deviation for each source [89]. The effects on the signal acceptance are also considered. JES and JER systematics result in shape uncertainties on the BDT response distributions. As an example, Figure 4.26 reports the different BDT response distributions obtained for the JES and JER up and down variations for the 2016 signal and background samples. All background contributions are summed together in these plots.
The above uncertainties apply equally to all simulated signal and backgrounds.
The experimental uncertainties originating from the Z+X background estimation, described in Section 4.2.5, are also considered. The main contribution arises from the mismatch in the composition of backgrounds between the samples where the misidentification rate is derived and where it is applied. This uncertainty affects the normalization of the Z+X yield estimation. A summary of experimental systematic uncertainties is reported in Table 4.15.

Table 4.14: Summary of theoretical systematic uncertainties.

Theory uncertainties	
PDF and α_s	
PDF set and α_s HH	3.0%
m_{top} unc HH	2.6%
PDF set ggH	1.8%
α_s ggH	$2.59 - 2.62\%$
PDF set and α_s VBFH	2.1%
PDF set and α_s ZH	1.6%
PDF set and α_s WH	1.3%
PDF set and α_s bbH	3.2%
PDF set and α_s ttH	3.6%
PDF set and α_s qqZZ	$3.1 - 3.4\%$
PDF set and α_s ttW	$25 - 37.5\%$
PDF set and α_s ttZ	$7 - 14\%$
PDF set and α_s VVV	$2 - 17\%$
PDF set and α_s ggZZ	3.2%
QCD scale	
HH	$2.2 - 5\%$
ggH	$4.27 - 6.49\%$
VBFH	$0.3 - 0.4\%$
ZH	$2.7 - 3.5\%$
WH	0.5%
bbH	$4.6 - 6.7\%$
ttH	$6.0 - 9.2\%$
qqZZ	$3.2 - 4.2\%$
ttW	$3 - 4\%$
ttZ	$2 - 3\%$
VVV	3%
ggZZ	$4.6 - 6.7\%$
Electroweak corrections	
qqZZ	0.1%
ggZZ	10.0%

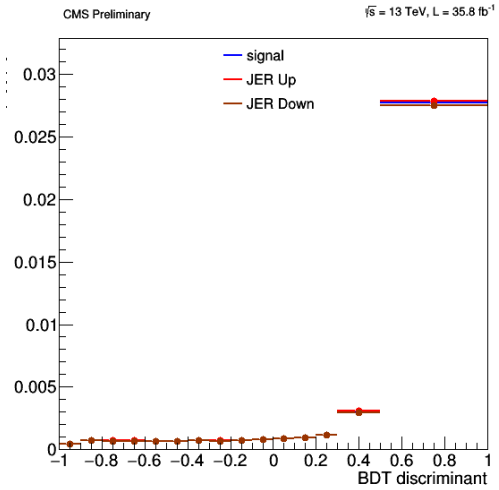

(a) JER for signal sample.

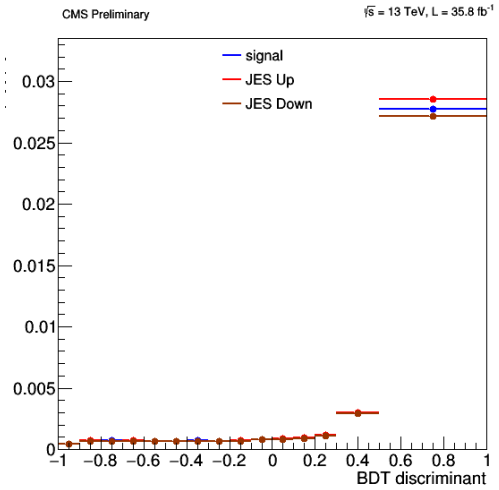

(b) JES for signal sample.

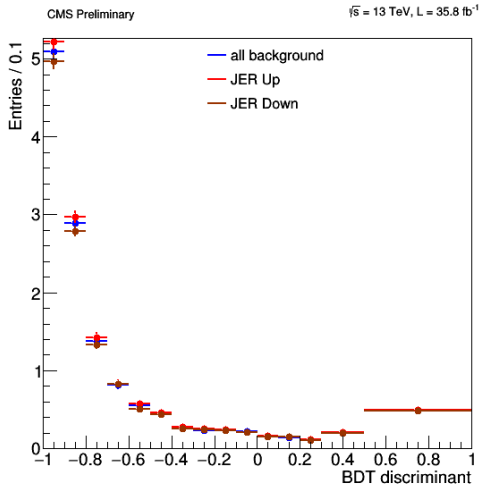

(c) JER for background samples.

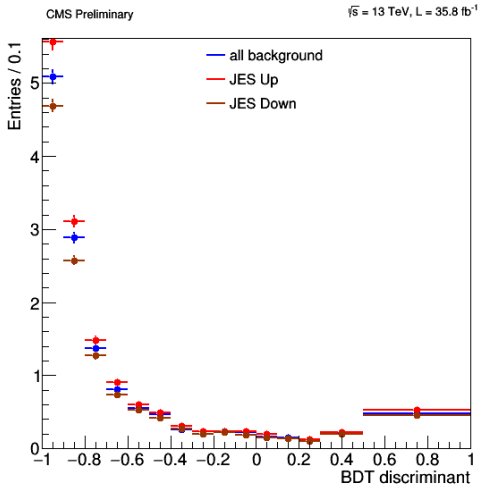

(d) JES for background samples.

Figure 4.26: Distribution of BDT response obtained for JES and JER up (red markers) and down (brown markers) variations for the 2016 signal and background samples. All background contributions (ggH, VBF, ttH, bbH, ttZ, VVV, VH where V = Z, W) are merged together. The nominal BDT response distribution is also reported (blue markers).

Table 4.15: Summary of experimental systematic uncertainties considered in the analysis. The effects of b tagging scale factors, jet energy scale (JES) and jet energy resolution (JER) uncertainties result in a shape contribution on the BDT response distributions.

Experimental uncertainties			
source	2016	2017	2018
Luminosity	2.6%	2.3%	2.5%
Leptons ID and reco eff	$1.6 - 15.5\%$	$1.1 - 12.1\%$	$1.0 - 11\%$
b tagging SF	shape	shape	shape
JES	shape	shape	shape
JER	shape	shape	shape
Z+X uncertainties	$30 - 41\%$	$30 - 38\%$	$30 - 37\%$

Chapter 5

Statistical analysis and Analysis results

5.1 Yields and kinematic distributions

After the event selection described in Section 4.1, the yields expected for signal and background processes, and the yields observed in data are extracted in the signal region (Section 4.1.4) and are reported in Table 5.1,5.2,5.3 for the 2016, 2017, and 2018 datasets, respectively. Figure 5.1 shows the invariant mass distributions of the two reconstructed Higgs bosons after the full event selection (Section 4.1). The reconstructed $H \to 4\ell$ mass is plotted in Figure 5.1 (a) after the full selection excluding the cut on $m_{4\ell}$ itself (Section 4.1.4). The reconstructed $H \to b\bar{b}$ mass after the full selection is shown in Figure 5.1 (b). A good data-MC agreement is observed.

The BDT algorithm (Section 4.3) is then applied to data, MC samples, and Z+X data-driven background, selected in the signal region. The BDT response distributions are obtained for each of the three final states ($b\bar{b}4\mu$, $b\bar{b}4e$, and $b\bar{b}2e2\mu$), for each data taking year, and, in case of MC, separately for each process. The distributions of the BDT response for the data, signal, and all backgrounds contributions obtained for the three different data taking years, combining together the contributions of the three final states for each year, are reported in Figure 4.10,4.14,4.18. The inclusive BDT response distribution, obtained combining the contributions of the three data taking years and of the three final states, is reported in Figure 5.2. The binning of the BDT response distributions is chosen to have (approximately) the same statistical uncertainties in the last five bins, in order to flatten the statistical fluctuations. A good data-MC agreement is observed and a good signal-background separation is obtained, for all the three years. In particular, it is possible to notice that the significance expressed as $S/\sqrt{B}$ (where S is the signal and B the background in each bin) is higher in the last three bins of the BDT

Table 5.1: Expected and observed yields in the signal region for 2016 datasets. The yield "others" contains contributions from TTW, WWZ, WZZ, and ZZZ processes. The contribution "bkg sum" contains the sum of all background yields. The reported uncertainties include only the statistical contribution.

Process	$b\bar{b}4\mu$	$b\bar{b}4e$	$b\bar{b}2e2\mu$	$b\bar{b}4\ell$
HH signal	0.013 ± 0.001	0.007 ± 0.001	0.020 ± 0.002	0.040 ± 0.002
ggH	2.635 ± 0.310	1.417 ± 0.291	3.457 ± 0.568	7.509 ± 0.709
VBFH	0.392 ± 0.029	0.201 ± 0.037	0.497 ± 0.067	1.090 ± 0.082
WH	0.215 ± 0.014	0.113 ± 0.019	0.274 ± 0.034	0.602 ± 0.041
ZH	0.175 ± 0.012	0.100 ± 0.018	0.238 ± 0.031	0.513 ± 0.038
ttH	0.169 ± 0.015	0.096 ± 0.017	0.226 ± 0.031	0.491 ± 0.038
bbH	0.040 ± 0.005	0.020 ± 0.004	0.050 ± 0.008	0.110 ± 0.010
ttZ	0.176 ± 0.047	0.120 ± 0.036	0.212 ± 0.063	0.508 ± 0.086
qqZZ	0.928 ± 0.159	0.345 ± 0.082	0.996 ± 0.191	2.269 ± 0.262
ggZZ	0.086 ± 0.018	0.043 ± 0.011	0.086 ± 0.020	0.215 ± 0.029
others	0.008 ± 0.003	0.014 ± 0.006	0.028 ± 0.011	0.050 ± 0.013
Z+X	0.790 ± 0.121	1.400 ± 0.073	2.640 ± 0.225	4.830 ± 0.265
bkg sum	5.614 ± 0.374	3.869 ± 0.317	8.704 ± 0.649	18.187 ± 0.813
Data	6	3	11	20

Table 5.2: Expected and observed yields in the signal region for 2017 datasets. The yield "others" contains contributions from TTW, WWZ, WZZ, and ZZZ processes. The contribution "bkg sum" contains the sum of all background yields. The reported uncertainties include only the statistical contribution.

Process	$b\bar{b}4\mu$	$b\bar{b}4e$	$b\bar{b}2e2\mu$	$b\bar{b}4\ell$
HH signal	0.016 ± 0.001	0.009 ± 0.001	0.024 ± 0.003	0.049 ± 0.003
ggH	3.260 ± 0.366	1.538 ± 0.284	3.985 ± 0.595	8.783 ± 0.754
VBFH	0.470 ± 0.032	0.231 ± 0.036	0.588 ± 0.068	1.289 ± 0.083
WH	0.277 ± 0.016	0.138 ± 0.021	0.349 ± 0.039	0.764 ± 0.047
ZH	0.211 ± 0.014	0.108 ± 0.016	0.290 ± 0.031	0.609 ± 0.037
ttH	0.209 ± 0.019	0.119 ± 0.020	0.279 ± 0.036	0.607 ± 0.045
bbH	0.051 ± 0.006	0.022 ± 0.004	0.059 ± 0.009	0.132 ± 0.011
ttZ	0.194 ± 0.033	0.131 ± 0.033	0.316 ± 0.059	0.641 ± 0.075
qqZZ	0.964 ± 0.136	0.318 ± 0.067	1.005 ± 0.174	2.287 ± 0.231
ggZZ	0.103 ± 0.018	0.045 ± 0.011	0.083 ± 0.017	0.231 ± 0.027
others	0.013 ± 0.004	0.005 ± 0.002	0.042 ± 0.015	0.060 ± 0.015
Z+X	1.480 ± 0.146	0.520 ± 0.028	2.000 ± 0.121	4.000 ± 0.192
Bkg sum	7.232 ± 0.421	3.175 ± 0.299	8.996 ± 0.641	19.403 ± 0.820
Data	9	2	6	17

Table 5.3: Expected and observed yields in the signal region for 2018 datasets. The yield "others" contains contributions from TTW, WWZ, WZZ, and ZZZ processes. The contribution "bkg sum" contains the sum of all background yields. The reported uncertainties include only the statistical contribution.

Process	$b\bar{b}4\mu$	$b\bar{b}4e$	$b\bar{b}2e2\mu$	$b\bar{b}4\ell$
HH signal	0.025 ± 0.002	0.013 ± 0.002	0.036 ± 0.004	0.074 ± 0.005
ggH	4.420 ± 0.509	2.217 ± 0.365	5.694 ± 0.786	12.331 ± 1.005
VBFH	0.721 ± 0.053	0.345 ± 0.049	0.860 ± 0.093	1.926 ± 0.118
WH	0.397 ± 0.025	0.197 ± 0.026	0.502 ± 0.049	1.096 ± 0.061
ZH	0.322 ± 0.023	0.161 ± 0.022	0.408 ± 0.042	0.891 ± 0.053
ttH	0.298 ± 0.029	0.166 ± 0.026	0.390 ± 0.049	0.854 ± 0.063
bbH	0.071 ± 0.009	0.032 ± 0.005	0.085 ± 0.012	0.188 ± 0.016
ttZ	0.242 ± 0.040	0.167 ± 0.036	0.476 ± 0.070	0.885 ± 0.088
qqZZ	1.507 ± 0.214	0.576 ± 0.104	1.556 ± 0.247	3.639 ± 0.343
ggZZ	0.143 ± 0.028	0.076 ± 0.018	0.125 ± 0.027	0.344 ± 0.043
others	0.027 ± 0.011	0.003 ± 0.002	0.048 ± 0.018	0.078 ± 0.021
Z+X	1.600 ± 0.134	0.720 ± 0.041	2.580 ± 0.306	4.900 ± 0.336
Bkg sum	9.748 ± 0.575	4.660 ± 0.389	12.724 ± 0.891	27.132 ± 1.129
Data	14	7	16	37

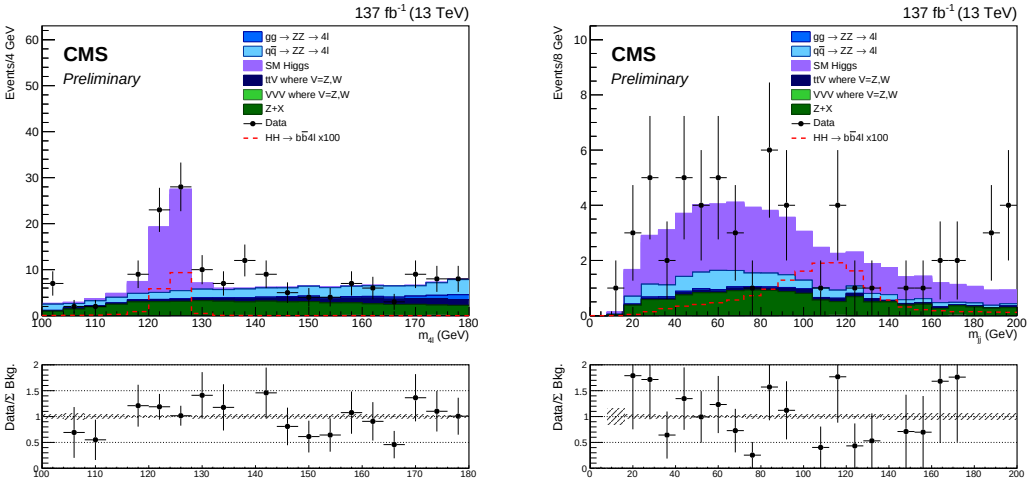

(a) Invariant mass distribution of the reconstructed H → 4ℓ after the full event selection excluding the cut on $m_{4\ell}$ itself.

(b) Invariant mass distribution of the reconstructed H → $b\bar{b}$ after the full event selection.

Figure 5.1: Invariant mass distributions of the two reconstructed Higgs bosons after the full event selection. The signal, represented by the red line, is enlarged to 100 times the SM expectation in order to make it visible. In the ratio plot, the grey dashed shades represent the relative statistical uncertainty on the total estimated background.

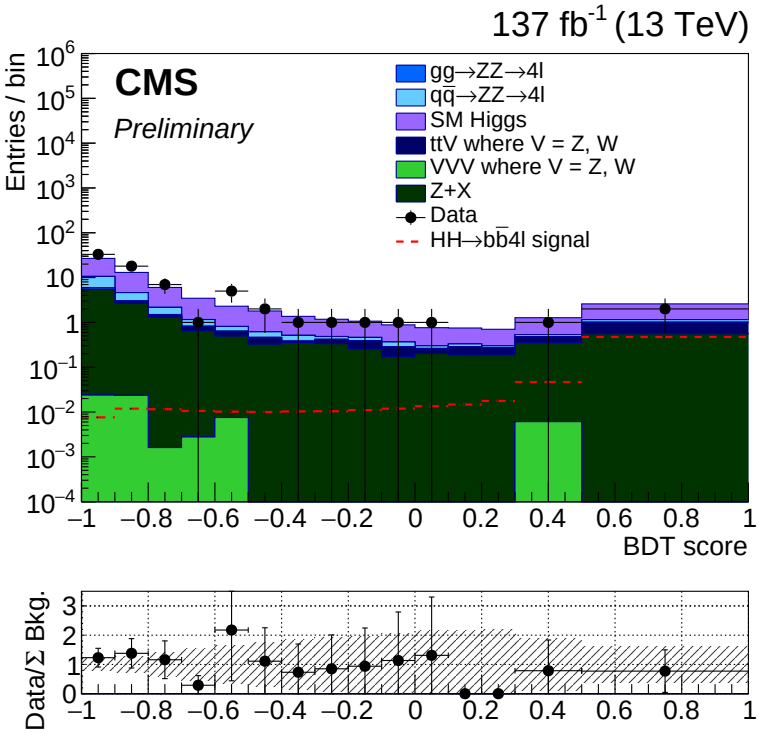

Figure 5.2: Inclusive BDT response distributions obtained combining the contributions of the three data taking years (2016, 2017, 2018) and for the three final states ($b\bar{b}4\mu$, $b\bar{b}4e$, and $b\bar{b}2e2\mu$) for each year. In the ratio plot, the grey dashed shade represents the relative statistical uncertainty on the total estimated background.

response distributions. This means that the majority of the signal is concentrated at large BDT scores, as expected for a well performing classifier.

The expected and observed yields selected in the signal region, the BDT response distributions obtained for each process and each data taking year, as well as the systematic uncertainties discussed in Section 4.4, are given as inputs to the *statistical analysis* performed to extract the final results.

5.2 Statistical analysis

A statistical analysis is performed in order to evaluate the presence of HH signal in the observed data, or to set an upper limit on its production cross section if no excess over the background predictions is observed. The statistical analysis also aims at setting a constraint on the anomalous Higgs boson self coupling.

The statistical method used for this purpose was developed by the ATLAS and CMS collaborations in the context of the combination of results of Higgs boson searches [33].

5.2.1 Likelihood function and nuisance parameters

To perform the statistical analysis a *likelihood function* is defined as the Probability Density Function (PDF)[1] that characterises the set of experimental observables considered in the analysis, given the parameters of the model.
The model adopted relies on a *signal strength modifier* parameter μ, that modifies the SM HH cross section by the scale μ and leaves the HH $\to 4\ell\mathrm{b}\bar{\mathrm{b}}$ decay branching fraction unchanged. It can be thus defined as the double-Higgs boson rate in the $4\ell\mathrm{b}\bar{\mathrm{b}}$ channel over the SM expectation.
Each independent source of systematic uncertainty described in Section 4.4 is assigned a *nuisance parameter* θ_i, and the full set is denoted as θ. These parameters are not of direct interest to the analysis, but they need to be considered in order to correctly extract the results. The uncertainty on their determination, in fact, will reflect on the parameters of interest of the model. To take into account the probability to measure a value $\tilde{\theta}_i$ for the i-th parameter, given its true value θ_i, the PDF $p_i(\tilde{\theta}_i|\theta_i)$ associated to each nuisance parameter is considered. The PDF for all the nuisance parameters is denoted as $p(\tilde{\theta}|\theta)$.
The expected background yields, b, and the expected signal yield, s, are functions of the nuisance parameters θ.
The likelihood function can thus be defined as:

$$\mathcal{L}(\text{data}|\mu,\theta) = \prod_c \mathcal{L}_c(\text{data}|\mu \cdot s(\theta) + b(\theta)) \cdot \prod_i p_i(\tilde{\theta}_i|\theta_i) \tag{5.1}$$

where "data" represents either the measured data or values from pseudo-datasets, i.e. sets of pseudo-random numbers sampled from the expected distributions given by the likelihood function, under certain hypotheses. The first product in Eq. 5.1 runs over all the channels considered in the analysis, i.e. the nine configurations obtained from the three final states ($\mathrm{b}\bar{\mathrm{b}}4\mu$, $\mathrm{b}\bar{\mathrm{b}}4e$, $\mathrm{b}\bar{\mathrm{b}}2e2\mu$) and the three data taking years (2016, 2017, 2018).
The $\mathcal{L}_c$ function is the PDF of the events that for binned distributions, like those used in the presented analysis, is given by the product of the Poisson probabilities

[1] Considering a random variable x, the Probability Density Function $f(x)$ is defined by

$$\mathcal{P}(x \in [x, x + \mathrm{d}x]) = f(x)\mathrm{d}x$$

where $\mathcal{P}$ is the probability of finding the value x in the interval $[x, x + \mathrm{d}x]$.

for every bin j considered to observe n_j events:

$$\mathcal{L}_c(\text{data}|\mu \cdot s(\theta) + b(\theta)) = \prod_j \frac{(\mu \cdot s_j(\theta) + b_j(\theta))^{n_j}}{n_j!} e^{-(\mu \cdot s_j(\theta) + b_j(\theta))} \tag{5.2}$$

The PDF associated to each nuisance parameter $p_i(\tilde{\theta}_i|\theta_i)$ assumes a different functional form according to the systematic uncertainty type described in Section 4.4. Normalization uncertainties are associated to log-normal PDFs. Shape uncertainty PDFs, instead, vary according to the different source of uncertainty and are modelled as alternate distributions of the BDT response predicted for each dedicated shape variation.

5.2.2 Hypothesis testing

Once the likelihood function is defined, it is possible to test different hypotheses on the basis of the observed data. In statistical literature, when two different hypotheses are considered, the first one is called *null hypothesis* H_0 and the second one is the *alternative hypothesis* H_1.
Hypothesis testing is based on building a *test statistic*, a function of the observed data that is derived from the likelihood function and encodes the information about expected signal and background, and uncertainties. The test statistic is a random variable that must be defined in such a way to have different distributions under the two considered hypotheses H_0 and H_1, in order to discriminate between them. The test statistic is usually built as a ratio of two likelihood functions, one evaluated for the observed data sample under the hypothesis H_0, and the other under H_1. The expected distributions followed by the test statistic under the two hypotheses are produced by generating pseudo-datasets from the PDFs included in the likelihood function. The test statistic is evaluated on the basis of the observed data and its value is compared with the expected distributions to quantify the compatibility of data with the alternative hypothesis.

Quantifying an excess

To quantify the statistical significance of an excess over the background-only expectation, the following test statistic is used:

$$q_0 = -2 \ln \frac{\mathcal{L}(\text{data}|0, \hat{\theta}_0)}{\mathcal{L}(\text{data}|\hat{\mu}, \hat{\theta})}, \quad \text{with } \hat{\mu} \geq 0 \tag{5.3}$$

The numerator is evaluated under the background-only hypothesis ($\mu = 0$), and $\hat{\theta}_0$ is the set of values of nuisance parameters that maximises it under this null hypothesis. The denominator is evaluated under the alternative signal+background hypothesis, and the values $\hat{\mu}$ and $\hat{\theta}$ are those that maximise the likelihood in the

denominator. With this definition q_0 is positive for a signal-like excess ($\mu > 0$), while in absence of an excess ($\mu = 0$) q_0 becomes 0.
The significance of an excess can be quantified in terms of the local *p-value*, defined as the probability to obtain a value of the test statistic q_0 as large as the one observed in experimental data under the background-only hypothesis:

$$p_0 = \mathcal{P}(q_0 \geqslant q_0^{obs}|b) \tag{5.4}$$

In other words, p_0 characterises the probability for a local background fluctuation to resemble the hypothesised signal at least as much as observed data do.
The p-value is usually converted in the *significance* Z of the excess through the Gaussian one-sided tail integral:

$$p_0 = \int_Z^\infty \frac{1}{\sqrt{2\pi}} e^{-x^2/2} \mathrm{d}x \tag{5.5}$$

The conventional $Z = 5\sigma$ threshold for claiming a discovery corresponds to a p-value of 2.8×10^{-7}.

Setting an upper limit

If no significant excess is observed, an upper limit is set on the considered signal hypothesis. To analyse this situation another test statistic is used, this time using the signal+background hypothesis in the numerator:

$$q_\mu = -2 \ln \frac{\mathcal{L}(\text{data}|\mu, \hat{\theta}_\mu)}{\mathcal{L}(\text{data}|\hat{\mu}, \hat{\theta})}, \quad \text{with } 0 \leq \hat{\mu} \leq \mu \tag{5.6}$$

where $\hat{\theta}_\mu$ maximises the numerator under the hypothesis of a signal with strength μ. $\hat{\mu}$ and $\hat{\theta}$ maximise the likelihood in the denominator, as before, and correspond to the global maximum of the likelihood. The lower constraint $0 \leq \hat{\mu}$ is required by physics, to have a positive signal rate; the upper constraint $\hat{\mu} \leq \mu$ is imposed to guarantee a one-sided confidence interval, this way upward fluctuations of the data are not considered as evidence against the hypothesis of a signal of strength μ.
This definition of the test statistic q_μ grants the possibility of deriving analytically the expected distributions of q_μ under the signal+background and background-only hypotheses, in the asymptotic limit of a large number of background events [95], instead of generating pseudo-datasets.
Exclusion limits in this analysis are computed with a modified frequentist approach, referred to as CL_s [96], taking the profile likelihood q_μ as test statistic, in the asymptotic approximation. Given an observed value of the test statistic q_μ^{obs}, obtained evaluating Eq. 5.6 with the observed data, the probability for q_μ to

be equal or larger than q_μ^{obs}, under the signal+background and background-only hypotheses, are defined, respectively, as:

$$\text{CL}_{\text{s+b}}(\mu) = P(q_\mu \geq q_\mu^{\text{obs}} | \mu \cdot s + b) \tag{5.7}$$

$$\text{CL}_{\text{b}}(\mu) = P(q_\mu \geq q_\mu^{\text{obs}} | b) \tag{5.8}$$

The quantity CL_{s} is defined as their ratio:

$$\text{CL}_{\text{s}}(\mu) = \frac{\text{CL}_{\text{s+b}}(\mu)}{\text{CL}_{\text{b}}(\mu)} \tag{5.9}$$

A signal of strength μ is excluded at a confidence level of α if $\text{CL}_{\text{s}}(\mu) < 1 - \alpha$. Usually, and also in this analysis, exclusion limits are computed for $\alpha = 95\%$.

5.3 Analysis Results

Results are extracted performing a multi-dimensional binned maximum likelihood fit over the BDT response distributions obtained for data in the three different final states ($\text{b}\bar{\text{b}}4\mu$, $\text{b}\bar{\text{b}}4e$, $\text{b}\bar{\text{b}}2e2\mu$) and for the three data taking years (2016, 2017, 2018), following the procedure presented in Section 5.2. BDT response distributions are obtained, as described in Section 4.3, applying the BDT to signal and background MC samples and to the data-driven Z+X background estimate. Systematic uncertainties, described in Section 4.4, are treated as nuisance parameters, as described in Section 5.2.1. The results reported in this section were published in the CMS paper [97].

5.3.1 SM results

A good agreement is observed between expected and observed yields selected in the signal region, as shown in Table 5.1, 5.2, 5.3.
In the absence of an excess in the observed data, upper limits are set on the HH production cross section times the HH $\rightarrow \text{b}\bar{\text{b}}4\ell$ branching fraction, using the procedure presented in Section 5.2.2, assuming SM branching fractions for Higgs boson decays. The results are given in terms of limits on the signal strength modifier μ, defined in Section 5.2.1.
Table 5.4 and Figure 5.3 report the 95% confidence level (CL) upper limits obtained separately for the three data taking years and inclusively for the full Run II dataset. The inclusive observed upper limit on μ amounts to 30 at 95% CL, while the expected inclusive upper limit is 37 at 95% CL. The observed upper limit excludes at 95% CL the existence an hypothetical HH signal with cross section of 30 times (or more) the SM cross section in the HH $\rightarrow \text{b}\bar{\text{b}}4\ell$ decay channel. Observed and expected limits are compatible within the uncertainties.

Table 5.4: Observed and expected upper limits at 95% CL on the signal strength modifier μ for the three data taking years and for the inclusive combination obtained with the full Run II dataset. One-σ and two-σ uncertainties are reported for the expected values.

	2016	2017	2018	Inclusive
Expected μ + 2σ	43	37	27	17
Expected μ + 1σ	64	55	39	24
Expected μ	102	88	61	37
Expected μ - 1σ	171	146	100	58
Expected μ - 2σ	276	234	157	89
Observed μ	122	59	53	30

From the results obtained, it is possible to observe that the inclusive result improves considerably the upper limit with respect to those set separately for the three different data taking years.

5.3.2 Constraint on BSM contributions

Upper limits are set also for different hypotheses of anomalous Higgs boson self coupling. Results are extracted using the procedure presented in Section 5.2.2 as a function of the Higgs boson self coupling modifier k_λ, while assuming the other BSM couplings to be equal to their SM values, i.e. $k_t = 1$, $c_g = 0$, $c_{2g} = 0$, $c_2 = 0$ (Section 1.2.2).
Observed and expected limits on the HH cross section times HH $\to$ b$\bar{\text{b}}4\ell$ branching fraction as a function of k_λ are shown in Figure 5.4 for the inclusive full Run II dataset. They are compared to the theoretical prediction for the HH cross section represented by the red curve. The exclusion limit follows the features of the HH production cross section, which is shaped by the destructive interference between the HH production via the Higgs boson self coupling and the emission of an HH pair from a top quark loop (Section 1.2.2). The minimum at $k_\lambda = 2.45$ corresponds to the maximum negative interference between the two diagrams, which results in a minimum of the cross section. As k_λ increases, the HH production via the Higgs boson self coupling becomes dominant and the limit tends asymptotically to the same value for both $k_\lambda \ll -10$ and $k_\lambda \gg 10$. The observed constraints on k_λ are $-9 < k_\lambda < 14$ at 95% CL, with the expected ones being $-10.5 < k_\lambda < 15.5$. Observed and expected constraints are compatible within the uncertainties.

5.3.3 Discussion

This analysis is the first HH search in CMS to produce results with the full Run II dataset. Although the sensitivity of this channel alone, with the current available amount of data, is somewhat limited, this analysis is expected to contribute to the combination that will be performed over all HH final states investigated in CMS.

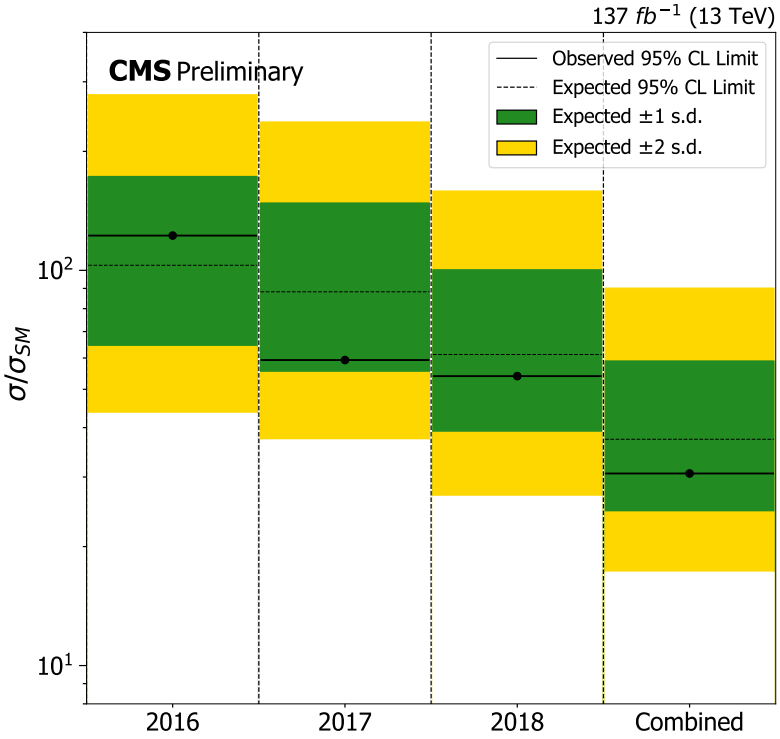

Figure 5.3: Observed and expected upper limits at 95% CL on the signal strength modifier μ for the three data taking years and for the inclusive combination. Green and yellow bands represent 1σ and 2σ uncertainties, respectively.

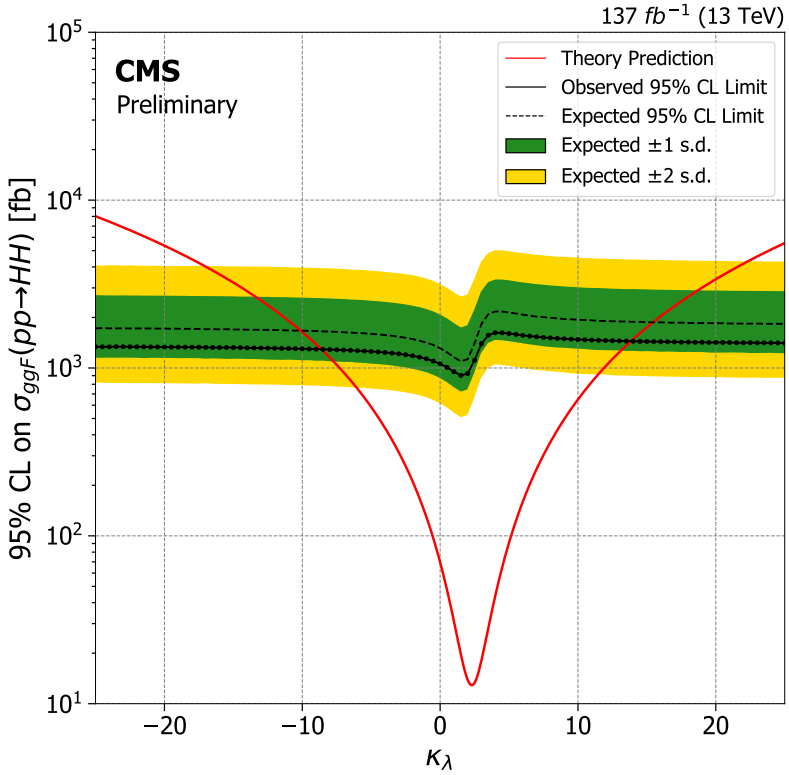

Figure 5.4: Expected and observed 95% CL upper limit on the HH cross section times the HH $\to$ b$\bar{\text{b}}4\ell$ branching fraction as a function of k_λ, for the full Run II dataset. The green and yellow bands represent, respectively, the one and two standard deviation uncertainties bands around the expected limit. The red line represents the theoretical prediction.

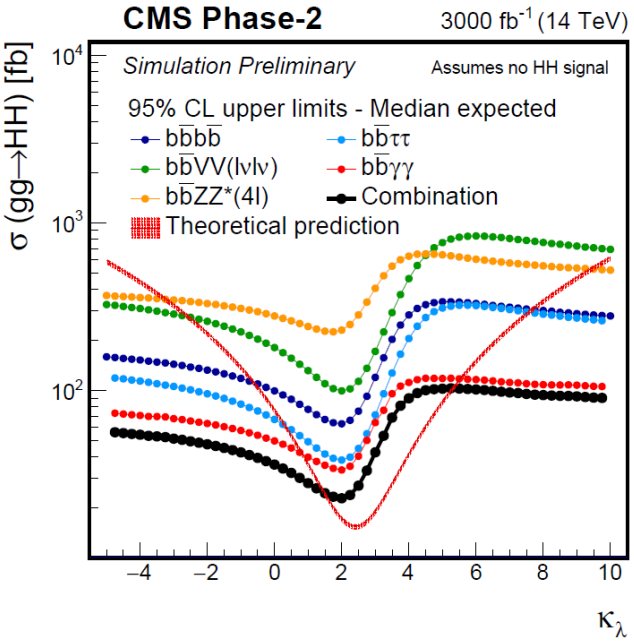

Figure 5.5: 95% CL upper limit on the HH production cross section as a function of k_λ for the five decay channels investigated in the HL-LHC projection study and their combination. The red line represents the theoretical production cross section [98].

The CMS collaboration performed a study on the prospects for searches of Higgs boson pair production and the measurement of Higgs boson self coupling at the High-Luminosity (HL) LHC [98]. Projected results for 3000 fb^{-1} were obtained considering five decay channels of the HH system to bbbb, bb$\tau\tau$, bbWW (with the W boson decaying leptonically), bb$\gamma\gamma$, and bbZZ (with Z bosons decaying into pairs of electrons or muons). Combination of these final states is shown to lead to an upper limit on the HH production cross section reaching 0.77 times the SM expectation, and a significance for the signal of 2.6 σ, slightly below the threshold usually quoted for an observation.
Prospects for the measurement of the Higgs boson self coupling were also studied and upper limits on the HH production cross section derived as a function of k_λ are shown in Figure 5.5.

These results underline that the observation of HH at LHC is a very challenging goal, and inclusion of all possible input, even from comparatively rare decay channels like the one presented in this thesis, is essential to extract the maximum possible information on the Higgs boson self-coupling from the available LHC data.

Conclusions

The non-resonant double-Higgs boson (HH) production can be used to directly study the Higgs boson self coupling. Observing HH production would be another crucial validation for the electroweak symmetry breaking (EWSB) mechanism, after the Higgs boson discovery. The search for HH production is experimentally very challenging because of the small production cross section predicted by the standard model (SM). Beyond standard model (BSM) contributions, however, could modify the cross section as well as the kinematic properties of the HH production process.

The analysis presented in this thesis is focused on the search for HH production in the final state where one of the two Higgs bosons decays into four leptons (4ℓ, where ℓ is either an electron or a muon), while the other one decays into a pair of b quarks ($\mathrm{b\bar{b}}$), which hadronise in jets. The results presented were obtained exploiting the full dataset collected by the CMS experiment in the LHC Run II.
In order to search for HH production in the $\mathrm{b\bar{b}}4\ell$ final state, a specific event selection was optimized to collect events containing four leptons and at least two jets, selecting then the two jets with the highest value of the b tag discriminator, which are the most likely to derive from b quarks hadronisation. A multivariate analysis technique was developed in order to separate signal from background contributions, exploiting the kinematic features of events. A statistical analysis was performed on selected events in order to extract the results. For the SM scenario, an upper limit on the HH production cross section times the $\mathrm{HH} \to \mathrm{b\bar{b}}4\ell$ branching fraction was set to 30 times the SM prediction at 95% CL, against the expected value of 37 times the SM prediction. Under the assumption of a possible BSM contribution, the analysis was able to constrain the Higgs boson self coupling modifier k_λ to the range $-9 < k_\lambda < 14$ at 95% CL, against the expected range $-10.5 < k_\lambda < 15.5$. These results were published in a CMS paper [97].
This analysis is the first HH search in CMS to produce results with the full Run II dataset. It is expected to contribute to the combination that will be performed over all HH final states investigated in CMS. The combination will improve considerably the constraint on HH observables with respect to the individual analyses. In this context, the inclusion of the $\mathrm{HH} \to 4\ell\mathrm{b\bar{b}}$ decay channel, which has never been investigated before, will provide essential information for the combination.

My personal contribution covered almost every aspect of the analysis presented. After investigating the possible sources of background affecting the considered final state, I defined the event selection. I started from the $H \to 4\ell$ candidate selection, choosing similar requirements to those used in the $H \to ZZ^* \to 4\ell$ analysis [55, 56, 57], which I have been contributing to during the first part of my PhD. I then optimised the jet selection and performed studies to choose the best method for building the $H \to b\bar{b}$ candidate from jet pairs.
I contributed to the development of the data-driven method for estimating the Z+X background, which originates from processes with leptons from mesons in flight decays or electrons from photon conversion or mis-reconstructed jets. A data-driven estimation for this background is necessary since uncertainties in the modelling of mis-identified leptons would affect an estimate from MC samples.
Initially, I performed studies in order to estimate the expected significance that could be obtained with a simple cut and count approach for extracting the results. Since the sensitivity to HH production of the considered final state is limited by the small branching fraction, it was necessary to use a more sophisticated analysis technique in order to extract the maximum possible amount of information from the available data sample. A multivariate technique was then adopted to enhance the signal vs background separation and thus improve the significance of the analysis. For the multivariate analysis, I contributed to the choice of the final set of input variables, and verified the data-MC agreement for the variables considered, providing the necessary calibrations to object selection where needed. I then took care of modelling the possible effect of systematic uncertainties. In particular I focused on jet uncertainties, developing the procedure to propagate all the different uncertainty sources for jet energy scale, jet energy resolution, and b tagging scale factors to final expected yields and observables.
Finally, I performed the statistical analysis for extracting the final results.

Within the CMS collaboration, I also took part to several experimental activities. In 2018, I participated in the data taking as detector on call shifter for the Drift Tubes (DT) muon system sub-detector, acquiring a large experience on the CMS experiments operations.
In 2019, I participated to the CMS detector upgrade activities performing Shift Leader duties, coordinating cosmic rays data collection for the commissioning of detectors upgrades, and contributing to the DT electronic upgrades. Since the DT detector is responsible for the tracking and triggering of muons in the central region of CMS, and since the higher L1 trigger rate foreseen for the high luminosity (HL) LHC upgrade will exceed the present capabilities of the DT on-detector electronics, DTs are profiting of the current Long Shutdown period to upgrade the on-detector electronics. In 2019 the first prototype of the new on-detector electronics was installed on the chambers of one sector of the central wheel of the CMS detector, in parallel to the old readout electronics in order to compare the

respective performances. I contributed at first characterising the new electronic boards and validating the installed firmware, and then participating as expert on call to the data taking performed after the boards were installed in CMS. The data collected with the new and old electronics were analysed with the performance comparison framework I contributed to develop. The features I implemented were useful for checking the improvement of the new system with respect to the old one, but also for spotting and correcting possible malfunctions or errors in the readout chain.
I also participated to the L1 muon trigger upgrade studies. To deal with the higher L1 trigger rate of HL-LHC, the CMS L1 muon trigger system is being upgraded. New trigger algorithms will include muon track reconstruction already at L1 trigger level. Since this new algorithm will be used in the whole CMS muon system, a common notation between the different muon detectors is necessary. In this context, I developed a framework for performance studies for the muon trigger upgrade, with a standard notation usable by all the muon subsystems, allowing an easier and faster comparison between detector regions.

The upgrade activities ongoing on the CMS detector will allow the CMS experiment to collect a larger data sample for analysis, and this, in pair with the improvement of analysis strategies and techniques, will allow new constraints on HH production to be set. In any case, combination of all possible inputs, even from rare decay channels like the one analysed in this thesis, is fundamental to obtain the maximum possible information on HH production.

In parallel with my work within the CMS collaboration, I took part to the LEMMA INFN project [99] aimed at investigating a new approach for building the muon source for a future muon collider. This approach is based on low emittance $\mu^+\mu^-$ pair production from $e^+e^- \to \mu^+\mu^-$ just above the production threshold ($\sqrt{s} = 212$ MeV), by using a beam of $\simeq 45$ GeV positrons on a thin target.
In summer 2018, I participated to two tests beams that took place at CERN aimed at investigating the $e^+e^- \to \mu^+\mu^-$ process using a positron beam on a beryllium target. I then contributed to the analysis performed on the collected data, whose results were published in the paper [100].
If realized, a future muon collider will have the detailed study of HH production as one of its main goals.

Bibliography

[1] F. Englert and R. Brout, "Broken Symmetry and the Mass of Gauge Vector Mesons," *Phys. Rev. Lett.* **13** (1964) 321–323.

[2] P. W. Higgs, "Broken Symmetries and the Masses of Gauge Bosons," *Phys. Rev. Lett.* **13** (1964) 508–509.

[3] G. S. Guralnik, C. R. Hagen, and T. W. B. Kibble, "Global Conservation Laws and Massless Particles," *Phys. Rev. Lett.* **13** (1964) 585–587.

[4] **ATLAS** Collaboration, G. Aad *et al.*, "Observation of a new particle in the search for the Standard Model Higgs boson with the ATLAS detector at the LHC," *Phys. Lett.* **B716** (2012) 1–29, arXiv:1207.7214 [hep-ex].

[5] **CMS** Collaboration, S. Chatrchyan *et al.*, "Observation of a new boson at a mass near 125 GeV with the CMS experiment at the LHC," *Phys. Lett.* **B716** (2012) 30–61, arXiv:1207.7235 [hep-ex].

[6] **ATLAS, CMS** Collaboration, G. Aad *et al.*, "Measurements of the Higgs boson production and decay rates and constraints on its couplings from a combined ATLAS and CMS analysis of the LHC pp collision data at $\sqrt{s} = 7$ and 8 TeV," *JHEP* **08** (2016) 045, arXiv:1606.02266 [hep-ex].

[7] **ATLAS** Collaboration, G. Aad *et al.*, "Combined measurements of Higgs boson production and decay using up to 80 fb^{-1} of proton-proton collision data at $\sqrt{s} = 13$ TeV collected with the ATLAS experiment," *Phys. Rev. D* **101** no. 1, (2020) 012002, arXiv:1909.02845 [hep-ex].

[8] **CMS** Collaboration, A. M. Sirunyan *et al.*, "Combined measurements of Higgs boson couplings in proton–proton collisions at $\sqrt{s} = 13\,\text{TeV}$," *Eur. Phys. J. C* **79** no. 5, (2019) 421, arXiv:1809.10733 [hep-ex].

[9] J. Baglio, A. Djouadi, R. Gröber, M. Mühlleitner, J. Quevillon, and M. Spira, "The measurement of the Higgs self-coupling at the LHC: theoretical status," *JHEP* **04** (2013) 151, arXiv:1212.5581 [hep-ph].

[10] **CMS** Collaboration, A. M. Sirunyan *et al.*, "Combination of searches for Higgs boson pair production in proton-proton collisions at $\sqrt{s} = 13$ TeV," *Phys. Rev. Lett.* **122** no. 12, (2019) 121803, arXiv:1811.09689 [hep-ex].

[11] J. Ellis, "Higgs Physics," in *2013 European School of High-Energy Physics*, pp. 117–168. 2015. arXiv:1312.5672 [hep-ph].

[12] J. Goldstone, "Field theories with "superconductor" solutions," *Il Nuovo Cimento (1955-1965)* **19** no. 1, (Jan, 1961) 154–164. https://doi.org/10.1007/BF02812722.

[13] R. Mohapatra and P. Pal, *Massive neutrinos in physics and astrophysics. Second edition*, vol. 60. 1998.

[14] C. Kim and A. Pevsner, *Neutrinos in physics and astrophysics*, vol. 8. 1993.

[15] **CMS** Collaboration, S. Chatrchyan *et al.*, "Observation of a new boson with mass near 125 GeV in pp collisions at $\sqrt{s} = 7$ and 8 TeV," *JHEP* **06** (2013) 081, arXiv:1303.4571 [hep-ex].

[16] **CMS** Collaboration, S. Chatrchyan *et al.*, "Study of the Mass and Spin-Parity of the Higgs Boson Candidate Via Its Decays to Z Boson Pairs," *Phys. Rev. Lett.* **110** no. 8, (2013) 081803, arXiv:1212.6639 [hep-ex].

[17] **ATLAS, CMS** Collaboration, G. Aad *et al.*, "Combined measurement of the Higgs Boson Mass in *pp* Collisions at $\sqrt{s} = 7$ and 8 TeV with the ATLAS and CMS Experiments," *Phys. Rev. Lett.* **114** (2015) 191803, arXiv:1503.07589 [hep-ex].

[18] **CMS** Collaboration, A. M. Sirunyan *et al.*, "Measurements of the Higgs boson width and anomalous HVV couplings from on-shell and off-shell production in the four-lepton final state," *Phys. Rev. D* **99** no. 11, (2019) 112003, arXiv:1901.00174 [hep-ex].

[19] **LHC Higgs Cross Section Working Group** Collaboration, D. de Florian *et al.*, "Handbook of LHC Higgs Cross Sections: 4. Deciphering the Nature of the Higgs Sector," arXiv:1610.07922 [hep-ph].

[20] **ATLAS** Collaboration, M. Aaboud *et al.*, "Observation of $H \to b\bar{b}$ decays and VH production with the ATLAS detector," *Phys. Lett. B* **786** (2018) 59–86, arXiv:1808.08238 [hep-ex].

[21] **CMS** Collaboration, A. M. Sirunyan *et al.*, "Observation of Higgs boson decay to bottom quarks," *Phys. Rev. Lett.* **121** no. 12, (2018) 121801, arXiv:1808.08242 [hep-ex].

[22] **CMS** Collaboration, A. M. Sirunyan *et al.*, "Observation of the Higgs boson decay to a pair of τ leptons with the CMS detector," *Phys. Lett. B* **779** (2018) 283–316, arXiv:1708.00373 [hep-ex].

[23] **ATLAS** Collaboration, M. Aaboud *et al.*, "Cross-section measurements of the Higgs boson decaying into a pair of τ-leptons in proton-proton collisions at $\sqrt{s} = 13$ TeV with the ATLAS detector," *Phys. Rev. D* **99** (2019) 072001, arXiv:1811.08856 [hep-ex].

[24] J. Alison *et al.*, "Higgs Boson Pair Production at Colliders: Status and Perspectives," in *Double Higgs Production at Colliders*, B. Di Micco, M. Gouzevitch, J. Mazzitelli, and C. Vernieri, eds. 9, 2019. arXiv:1910.00012 [hep-ph].

[25] R. M. Schabinger and J. D. Wells, "A Minimal spontaneously broken hidden sector and its impact on Higgs boson physics at the large hadron collider," *Phys. Rev. D* **72** (2005) 093007, arXiv:hep-ph/0509209.

[26] G. Branco, P. Ferreira, L. Lavoura, M. Rebelo, M. Sher, and J. P. Silva, "Theory and phenomenology of two-Higgs-doublet models," *Phys. Rept.* **516** (2012) 1–102, arXiv:1106.0034 [hep-ph].

[27] K. Agashe, H. Davoudiasl, G. Perez, and A. Soni, "Warped Gravitons at the LHC and Beyond," *Phys. Rev. D* **76** (2007) 036006, arXiv:hep-ph/0701186.

[28] L. Randall and R. Sundrum, "A Large mass hierarchy from a small extra dimension," *Phys. Rev. Lett.* **83** (1999) 3370–3373, arXiv:hep-ph/9905221.

[29] A. Carvalho, M. Dall'Osso, T. Dorigo, F. Goertz, C. A. Gottardo, and M. Tosi, "Higgs Pair Production: Choosing Benchmarks With Cluster Analysis," *JHEP* **04** (2016) 126, arXiv:1507.02245 [hep-ph].

[30] S. Dawson and C. W. Murphy, "Standard Model EFT and Extended Scalar Sectors," *Phys. Rev. D* **96** no. 1, (2017) 015041, arXiv:1704.07851 [hep-ph].

[31] F. del Aguila, M. Perez-Victoria, and J. Santiago, "Observable contributions of new exotic quarks to quark mixing," *JHEP* **09** (2000) 011, arXiv:hep-ph/0007316.

[32] R. Grober and M. Muhlleitner, "Composite Higgs Boson Pair Production at the LHC," *JHEP* **06** (2011) 020, arXiv:1012.1562 [hep-ph].

[33] **ATLAS, CMS** Collaboration, LHC Higgs Combination Group, "Procedure for the lhc higgs boson search combination in summer 2011," Tech. Rep. ATL-PHYS-PUB-2011-011/CMS-NOTE-2011-005, CERN, 2011. http://cdsweb.cern.ch/record/1379837.

[34] R. Frederix, S. Frixione, V. Hirschi, F. Maltoni, O. Mattelaer, P. Torrielli, E. Vryonidou, and M. Zaro, "Higgs pair production at the LHC with NLO and parton-shower effects," *Phys. Lett. B* **732** (2014) 142–149, arXiv:1401.7340 [hep-ph].

[35] **CMS** Collaboration, A. M. Sirunyan *et al.*, "Search for Higgs boson pair production in the $bb\tau\tau$ final state in proton-proton collisions at $\sqrt(s) = 8$ TeV," *Phys. Rev. D* **96** no. 7, (2017) 072004, arXiv:1707.00350 [hep-ex].

[36] Y. Baconnier, G. Brianti, P. Lebrun, A. G. Mathewson, and R. Perin, "LHC: the Large Hadron Collider accelerator project," Tech. Rep. CERN-AC-93-03-LHC, Geneva, 1993. http://cds.cern.ch/record/257706.

[37] E. Mobs, "The CERN accelerator complex. Complexe des accélérateurs du CERN,". https://cds.cern.ch/record/2197559.

[38] **CMS** Collaboration, S. Chatrchyan *et al.*, "The CMS Experiment at the CERN LHC," *JINST* **3** (2008) S08004.

[39] **CMS** Collaboration, "CMS Technical Design Report for the Pixel Detector Upgrade," Tech. Rep. CERN-LHCC-2012-016. CMS-TDR-11, 9, 2012. https://cds.cern.ch/record/1481838.

[40] **CMS** Collaboration, S. Chatrchyan *et al.*, "Performance of CMS Muon Reconstruction in pp Collision Events at $\sqrt{s} = 7$ TeV," *JINST* **7** (2012) P10002, arXiv:1206.4071 [physics.ins-det].

[41] **CMS** Collaboration, A. Sirunyan *et al.*, "Particle-flow reconstruction and global event description with the CMS detector," *JINST* **12** (2017) P10003, arXiv:1706.04965 [physics.ins-det].

[42] W. Adam, R. Frühwirth, A. Strandlie, and T. Todorov, "Reconstruction of Electrons with the Gaussian-Sum Filter in the CMS Tracker at the LHC," Tech. Rep. CMS-NOTE-2005-001, CERN, Geneva, Jan, 2005. https://cds.cern.ch/record/815410.

[43] P. Billoir, "Progressive track recognition with a Kalman like fitting procedure," *Comput. Phys. Commun.* **57** (1989) 390–394.

[44] M. Cacciari, G. P. Salam, and G. Soyez, "The Anti-k(t) jet clustering algorithm," *JHEP* **04** (2008) 063, arXiv:0802.1189 [hep-ph].

[45] **ATLAS** Collaboration, G. Aad *et al.*, "Search For Higgs Boson Pair Production in the $\gamma\gamma b\bar{b}$ Final State using pp Collision Data at $\sqrt{s} = 8$ TeV from the ATLAS Detector," *Phys. Rev. Lett.* **114** no. 8, (2015) 081802, arXiv:1406.5053 [hep-ex].

[46] **ATLAS** Collaboration, G. Aad *et al.*, "Search for Higgs boson pair production in the $b\bar{b}b\bar{b}$ final state from pp collisions at $\sqrt{s} = 8$ TeVwith the ATLAS detector," *Eur. Phys. J. C* **75** no. 9, (2015) 412, arXiv:1506.00285 [hep-ex].

[47] **ATLAS** Collaboration, G. Aad *et al.*, "Searches for Higgs boson pair production in the $hh \to bb\tau\tau, \gamma\gamma WW^*, \gamma\gamma bb, bbbb$ channels with the ATLAS detector," *Phys. Rev. D* **92** (2015) 092004, arXiv:1509.04670 [hep-ex].

[48] **ATLAS** Collaboration, M. Aaboud *et al.*, "Search for pair production of Higgs bosons in the $b\bar{b}b\bar{b}$ final state using proton–proton collisions at $\sqrt{s} = 13$ TeV with the ATLAS detector," *Phys. Rev. D* **94** no. 5, (2016) 052002, arXiv:1606.04782 [hep-ex].

[49] **ATLAS** Collaboration, M. Aaboud *et al.*, "Search for Higgs boson pair production in the $WW^{(*)}WW^{(*)}$ decay channel using ATLAS data recorded at $\sqrt{s} = 13$ TeV," *JHEP* **05** (2019) 124, arXiv:1811.11028 [hep-ex].

[50] **ATLAS** Collaboration, M. Aaboud *et al.*, "Search for Higgs boson pair production in the $\gamma\gamma WW^*$ channel using pp collision data recorded at $\sqrt{s} = 13$ TeV with the ATLAS detector," *Eur. Phys. J. C* **78** no. 12, (2018) 1007, arXiv:1807.08567 [hep-ex].

[51] **CMS** Collaboration, V. Khachatryan *et al.*, "Search for two Higgs bosons in final states containing two photons and two bottom quarks in proton-proton collisions at 8 TeV," *Phys. Rev. D* **94** no. 5, (2016) 052012, arXiv:1603.06896 [hep-ex].

[52] **CMS** Collaboration, V. Khachatryan *et al.*, "Search for resonant pair production of Higgs bosons decaying to two bottom quark–antiquark pairs in proton–proton collisions at 8 TeV," *Phys. Lett. B* **749** (2015) 560–582, arXiv:1503.04114 [hep-ex].

[53] **CMS** Collaboration, A. M. Sirunyan *et al.*, "Search for Higgs boson pair production in events with two bottom quarks and two tau leptons in proton–proton collisions at $\sqrt{s}$ =13TeV," *Phys. Lett. B* **778** (2018) 101–127, arXiv:1707.02909 [hep-ex].

[54] **CMS** Collaboration, A. M. Sirunyan *et al.*, "Search for resonant and nonresonant Higgs boson pair production in the $\mathrm{b\bar{b}}\ell\nu\ell\nu$ final state in proton-proton collisions at $\sqrt{s} = 13$ TeV," *JHEP* **01** (2018) 054, arXiv:1708.04188 [hep-ex].

[55] **CMS** Collaboration, A. M. Sirunyan *et al.*, "Measurements of properties of the Higgs boson decaying into the four-lepton final state in pp collisions at $\sqrt{s} = 13$ TeV," *JHEP* **11** (2017) 047, arXiv:1706.09936 [hep-ex].

[56] **CMS** Collaboration, A. M. Sirunyan *et al.*, "Measurements of properties of the Higgs boson in the four-lepton final state at $\sqrt{s} = 13$ TeV," Tech. Rep. CMS-PAS-HIG-18-001, CERN, Geneva, 2018. https://cds.cern.ch/record/2621419.

[57] **CMS** Collaboration, A. M. Sirunyan *et al.*, "Measurements of properties of the Higgs boson in the four-lepton final state in proton-proton collisions at $\sqrt{s} = 13$ TeV," Tech. Rep. CMS-PAS-HIG-19-001, CERN, Geneva, 2019. https://cds.cern.ch/record/2668684.

[58] **CMS** Collaboration, S. Chatrchyan *et al.*, "Measurement of the Inclusive W and Z Production Cross Sections in pp Collisions at $\sqrt{s} = 7$ TeV," *JHEP* **10** (2011) 132, arXiv:1107.4789 [hep-ex].

[59] S. Alioli, P. Nason, C. Oleari, and E. Re, "NLO vector-boson production matched with shower in POWHEG," *JHEP* **07** (2008) 060, arXiv:0805.4802 [hep-ph].

[60] P. Nason, "A new method for combining NLO QCD with shower Monte Carlo algorithms," *JHEP* **11** (2004) 040, arXiv:hep-ph/0409146.

[61] S. Frixione, P. Nason, and C. Oleari, "Matching NLO QCD computations with parton shower simulations: the POWHEG method," *JHEP* **11** (2007) 070, arXiv:0709.2092 [hep-ph].

[62] G. Heinrich, S. P. Jones, M. Kerner, G. Luisoni, and E. Vryonidou, "NLO predictions for Higgs boson pair production with full top quark mass dependence matched to parton showers," *JHEP* **08** (2017) 088, arXiv:1703.09252 [hep-ph].

[63] G. Buchalla, M. Capozi, A. Celis, G. Heinrich, and L. Scyboz, "Higgs boson pair production in non-linear Effective Field Theory with full m_t-dependence at NLO QCD," *JHEP* **09** (2018) 057, arXiv:1806.05162 [hep-ph].

[64] P. Nason and C. Oleari, "NLO Higgs boson production via vector-boson fusion matched with shower in POWHEG," *JHEP* **02** (2010) 037, arXiv:0911.5299 [hep-ph].

[65] H. B. Hartanto, B. Jager, L. Reina, and D. Wackeroth, "Higgs boson production in association with top quarks in the POWHEG BOX," *Phys. Rev. D* **91** (2015) 094003, arXiv:1501.04498 [hep-ph].

[66] J. M. Campbell, R. K. Ellis, R. Frederix, P. Nason, C. Oleari, and C. Williams, "NLO Higgs boson production plus one and two jets using the POWHEG BOX, MadGraph4 and MCFM," *JHEP* **07** (2012) 092, arXiv:1202.5475 [hep-ph].

[67] G. Luisoni, P. Nason, C. Oleari, and F. Tramontano, "$HW^{\pm}$/HZ + 0 and 1 jet at NLO with the POWHEG BOX interfaced to GoSam and their merging within MiNLO," *JHEP* **10** (2013) 083, arXiv:1306.2542 [hep-ph].

[68] Y. Gao, A. V. Gritsan, Z. Guo, K. Melnikov, M. Schulze, and N. V. Tran, "Spin determination of single-produced resonances at hadron colliders," *Phys. Rev.* **D81** (2010) 075022, arXiv:1001.3396 [hep-ph].

[69] M. Grazzini, S. Kallweit, and D. Rathlev, "ZZ production at the LHC: fiducial cross sections and distributions in NNLO QCD," *Phys. Lett.* **B750** (2015) 407–410, arXiv:1507.06257 [hep-ph].

[70] J. M. Campbell and R. K. Ellis, "MCFM for the Tevatron and the LHC," *Nucl. Phys. Proc. Suppl.* **205** (2010) 10, arXiv:1007.3492 [hep-ph].

[71] J. M. Campbell, R. K. Ellis, and C. Williams, "Bounding the Higgs width at the LHC using full analytic results for $gg- > e^{-}e^{+}\mu^{-}\mu^{+}$," *JHEP* **04** (2014) 060, arXiv:1311.3589 [hep-ph].

[72] M. Bonvini, F. Caola, S. Forte, K. Melnikov, and G. Ridolfi, "Signal-background interference effects in $gg \to H \to WW$ beyond leading order," *Phys. Rev. D* **88** (2013) 034032, arXiv:1304.3053 [hep-ph].

[73] S. Catani and M. Grazzini, "An NNLO subtraction formalism in hadron collisions and its application to Higgs boson production at the LHC," *Phys. Rev. Lett.* **98** (2007) 222002, arXiv:hep-ph/0703012 [hep-ph].

[74] M. Grazzini, "NNLO predictions for the Higgs boson signal in the $H \to WW \to l\nu l\nu$ and $H \to ZZ \to 4l$ decay channels," *JHEP* **02** (2008) 043, arXiv:0801.3232 [hep-ph].

[75] M. Grazzini and H. Sargsyan, "Heavy-quark mass effects in Higgs boson production at the LHC," *JHEP* **09** (2013) 129, arXiv:1306.4581 [hep-ph].

[76] K. Melnikov and M. Dowling, "Production of two Z-bosons in gluon fusion in the heavy top quark approximation," *Phys. Lett. B* **744** (2015) 43–47, arXiv:1503.01274 [hep-ph].

[77] C. S. Li, H. T. Li, D. Y. Shao, and J. Wang, "Soft gluon resummation in the signal-background interference process of gg($\to$ h) $\to$ ZZ," *JHEP* **08** (2015) 065, arXiv:1504.02388 [hep-ph].

[78] G. Passarino, "Higgs CAT," *Eur. Phys. J. C* **74** (2014) 2866, arXiv:1312.2397 [hep-ph].

[79] T. Sjöstrand, S. Mrenna, and P. Skands, "PYTHIA 6.4 physics and manual," *JHEP* **05** (2006) 026, arXiv:hep-ph/0603175 [hep-ph].

[80] T. Sjöstrand, S. Ask, J. R. Christiansen, R. Corke, N. Desai, P. Ilten, S. Mrenna, S. Prestel, C. O. Rasmussen, and P. Z. Skands, "An introduction to PYTHIA 8.2," *Comput. Phys. Commun.* **191** (2015) 159, arXiv:1410.3012 [hep-ph].

[81] **CMS** Collaboration, V. Khachatryan *et al.*, "Event generator tunes obtained from underlying event and multiparton scattering measurements," *Eur. Phys. J. C* **76** (2016) 155, arXiv:1512.00815 [hep-ex].

[82] **CMS** Collaboration, A. M. Sirunyan *et al.*, "Extraction and validation of a new set of CMS PYTHIA8 tunes from underlying-event measurements," *Eur. Phys. J. C* **80** (2020) 4, arXiv:1903.12179 [hep-ex].

[83] **NNPDF** Collaboration, R. D. Ball *et al.*, "Parton distributions for the LHC run II," *JHEP* **04** (2015) 040, arXiv:1410.8849 [hep-ph].

[84] **GEANT4** Collaboration, S. Agostinelli *et al.*, "GEANT4—a simulation toolkit," *Nucl. Instrum. Meth. A* **506** (2003) 250.

[85] J. Allison *et al.*, "GEANT4 developments and applications," *IEEE Trans. Nucl. Sci.* **53** (2006) 270.

[86] **CMS** Collaboration, A. M. Sirunyan *et al.*, "W-like measurement of the Z boson mass using dimuon events collected in pp collisions at $\sqrt{s} = 7$ TeV," Tech. Rep. CMS-PAS-SMP-14-007, CERN, Geneva, 2016. https://cds.cern.ch/record/2139655.

[87] **CMS** Collaboration, A. M. Sirunyan *et al.*, "Jet algorithms performance in 13 TeV data," Tech. Rep. CMS-PAS-JME-16-003, 2017. https://cds.cern.ch/record/2256875.

[88] **CMS** Collaboration, A. Sirunyan *et al.*, "Search for resonant and nonresonant Higgs boson pair production in the $\mathrm{b\bar{b}}\ell\nu\ell\nu$ final state in proton-proton collisions at $\sqrt{s} = 13$ TeV," *J. High Energ. Phys.* **01** (2018) 054.

[89] **CMS** Collaboration, A. M. Sirunyan *et al.*, "Determination of jet energy calibration and transverse momentum resolution in CMS," *JINST* **6** (2011) P11002, arXiv:1107.4277.

[90] **CMS** Collaboration, V. Khachatryan *et al.*, "Jet energy scale and resolution in the CMS experiment in pp collisions at 8 TeV," *JINST* **12** (2017) P02014, arXiv:1607.03663.

[91] **CMS** Collaboration, A. M. Sirunyan *et al.*, "Jet energy scale and resolution performances with 13 TeV data," CMS Detector Performance Summary CMS-DP-2016-020, 2016. https://cds.cern.ch/record/2160347.

[92] A. Hoecker *et al.*, "TMVA - Toolkit for Multivariate Data Analysis," arXiv:physics/0703039 [physics.data-an].

[93] M. Cepeda *et al.*, "Report from Working Group 2: Higgs Physics at the HL-LHC and HE-LHC," Tech. Rep. CERN-LPCC-2018-04, 12, 2019. arXiv:1902.00134 [hep-ph].

[94] M. Grazzini, G. Heinrich, S. Jones, S. Kallweit, M. Kerner, J. M. Lindert, and J. Mazzitelli, "Higgs boson pair production at NNLO with top quark mass effects," *JHEP* **05** (2018) 059, arXiv:1803.02463 [hep-ph].

[95] G. Cowan, K. Cranmer, E. Gross, and O. Vitells, "Asymptotic formulae for likelihood-based tests of new physics," *Eur. Phys. J.* **C71** (2011) 1554, arXiv:1007.1727 [physics.data-an].

[96] A. L. Read, "Presentation of search results: the CLs technique," *Journal of Physics G: Nuclear and Particle Physics* (2002) . https://doi.org/10.1088/0954-3899/28/10/313.

[97] **CMS** Collaboration, A. M. Sirunyan *et al.*, "Search for nonresonant Higgs boson pair production in the 4 leptons plus 2 b jets final state in proton-proton collisions at $\sqrt{s} = 13$ TeV," Tech. Rep. CMS-PAS-HIG-20-004, CERN, 2020. http://cds.cern.ch/record/2725691.

[98] **CMS** Collaboration, "Prospects for HH measurements at the HL-LHC," Tech. Rep. CMS-PAS-FTR-18-019, CERN, 2018. https://cds.cern.ch/record/2652549.

[99] M. Antonelli, M. Boscolo, R. Di Nardo, and P. Raimondi, "Novel proposal for a low emittance muon beam using positron beam on target," *Nucl. Instrum. Meth. A* **807** (2016) 101–107, arXiv:1509.04454 [physics.acc-ph].

[100] N. Amapane *et al.*, "Study of muon pair production from positron annihilation at threshold energy," *JINST* **15** no. 01, (2020) P01036, arXiv:1909.13716 [hep-ex].